Bottom Production at

$\sqrt{s} = 41.6$ GeV

Bottom Production at

$\sqrt{s} = 41.6$ GeV

The $b\bar{b}$ Production Cross Section in pN Collisions at $\sqrt{s} = 41.6$ GeV

De werkzame doorsnede voor $b\bar{b}$ productie in proton-kern botsingen bij $\sqrt{s} = 41.6$ GeV
(met een samenvatting in het Nederlands)

PROEFSCHRIFT

ter verkrijging van de graad van Doctor
aan de Universiteit Utrecht op gezag
van de Rector Magnificus, Prof. Dr. W.H. Gispen,
ingevolge het besluit van het College voor Promoties
in het openbaar te verdedigen op
woensdag 07 September 2005 des middags te 16.15 uur

door

Hernán Pablo Wahlberg

Geboren op 8 Febraury 1974, te Buenos Aires - Argentinië

promotor: **Prof. Dr. P.M. Kooijman**
Faculteit Natuur- & Sterrenkunde
Universiteit Utrecht
copromotor: **Dr. Th.S. Bauer**
Nationaal Instituut voor Kernfysica en
Hoge-Energie Fysica (NIKHEF)

Contents

Introduction

Quantum ChromoDynamics (QCD) is the theory of the strong interaction. It is modelled in analogy to Quantum Electro Dynamics (QED), and is formulated in terms of elementary fields of quarks and gluons. The cross section for quark pair production in hadronic collisions can be expressed as a perturbation series in the QCD running coupling constant α_s. For small quark masses this series does not converge sufficiently fast, but for heavy quarks, like the charm, bottom and top, it does so that the predictions of perturbative QCD can be confronted with the experimental results. This implies that measurements of sufficient precision are needed in order to verify the predictions of the theory, to improve the theory, or to identify aspects which are not covered by it.

The production of $b\bar{b}$ is particular relevant in several respects. For instance in the context of heavy-ion physics at LHC or RICH energies, bottom production may become a relevant source of J/ψ mesons. Since one of the signatures of Quark Gluon Plasma (QGP) formation is the J/ψ production suppression, a precise understanding of the $b\bar{b}$ production is needed to evaluate the contamination from $b \to J/\psi$ events. In the context of CP violation studies at LHC, but also in other studies where $b\bar{b}$ events become a source of background like top quark production, a better understanding of $b\bar{b}$ production will improve the trigger design and strategies.

By itself, $b\bar{b}$ production provides a road to improve our knowledge on the calculation of perturbative processes in QCD. At present there are complete calculations up to next-to-leading-order (NLO) in the expansion of α_s. However, these calculations fail to give an accurate value on the $b\bar{b}$ production cross section at energies near threshold, since higher order terms represent large contributions to the cross section. This makes $b\bar{b}$ production at threshold energies a suitable test case for new developments and for theoretical tools which aim at including higher order terms in the perturbative expansion, thus increasing our knowledge beyond NLO.

In the past $b\bar{b}$ production on fixed target has been measured three times. However, these results are not all compatible, and in addition, they suffer from limited statistics. In the year 2000 HERA – B performed a first $b\bar{b}$ cross section measurement. This was done with a detector which was only partially commissioned, and the results were based on a statistically very small sample. In late 2002 and early 2003, HERA – B took its last data, this time with much more statistics, such that the accuracy was considerably increased over the previous measurement. In this thesis we report on the analysis of the

new measurement of the $b\bar{b}$ cross section based on this 2002-2003 data sample.

Outline

We first describe the theoretical framework of perturbative QCD for the production of heavy quarks. We concentrate on describing the renormalisation procedure needed and the techniques to include high order terms (beyond NLO) in the perturbative expansion. In Chapter 2 we describe the HERA – B detector and the setup for the data taking period of 2002-2003. In Chapter 3 we describe the data taking conditions and data samples used in this thesis together with the simulations needed for the determination of detector and trigger efficiencies. Chapter 4 presents a more detailed description of the First Level Trigger system together with a study of its performance during the 2002-2003 data taking period. In Chapter 5 we describe the determination of the $b\bar{b}$ cross section through the inclusive $\mathrm{B} \rightarrow J/\psi + \mathrm{X}$ decay in the J/ψ muon channel. The last chapter describes the search for exclusive fully reconstructed decays in the $\mathrm{B}^+ \rightarrow J/\psi\ \mathrm{K}^+$ and $\mathrm{B}^0 \rightarrow J/\psi\ \mathrm{K}^+\ \pi^-$ decay channels.

Chapter 1

Heavy flavour production

In this chapter we describe the theoretical predictions for the $b\bar{b}$ cross section highlighting the main ideas behind the present calculations. First we introduce the dynamic quantities needed to describe the production process. Then we present the renormalisation and regularisation formalisms needed to give perturbative QCD predictive power, and highlight the problems for the calculation near threshold where large logarithms prevent fast convergence of the perturbative expansion. The specific approaches to overcome this problem are described in the context of the $b\bar{b}$ cross section at HERA – B energies. Finally, we also give an overview of charmonium production models, since J/ψ production is crucial to our measurement of the $b\bar{b}$ cross section, and we comment on nuclear effects in quarkonium production.

1.1 Parton model

At HERA – B protons of 920 GeV collide with fixed target materials. At these energies, hard interactions occur between the constituent partons (quarks and gluons) of the nucleons (proton and neutrons). Figure 1.1 shows the process schematically for two colliding nucleons of four momenta P_1 and P_2. The interacting partons carry fractions x_1 and x_2 of the respective total nucleon four momenta. Typically, the following variables are used to describe the process:

$$S = (P_1 + P_2)^2; \tag{1.1}$$

$$p_1 = x_1 P_1 \ ; \ p_2 = x_2 P_2; \tag{1.2}$$

$$s = (p_1 + p_2)^2; \tag{1.3}$$

$$x_F = \frac{p_z}{p_{z,max}} \sim x_1 - x_2. \tag{1.4}$$

x_F, introduced in 1.4, is called the "Feynman-x variable".

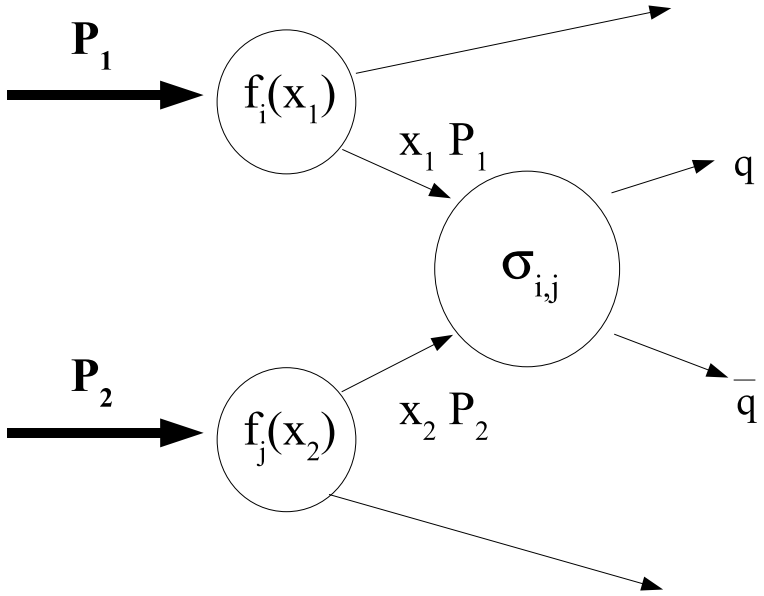

Figure 1.1: Schematic view of two colliding nucleons of momenta P_1 and P_2. The partons inside the nucleons are described by parton distribution functions f_i. In this process the hard interaction (σ_{ij}) which produces the $q\bar{q}$ pair, occurs between two partons carrying fractional four momenta x_1 and x_2.

In the parton model one assumes that the partons (quarks and gluons) are distributed according to the "parton distribution functions" (PDF). These PDFs ($f(x)$) describe the probability to find a certain parton with a momentum fraction x of the nucleon. Naturally, they have to satisfy sum rules, like the momentum sum rule which states that the sum of all parton momenta must equal the total nucleon momentum:

$$\int_0^1 dx \sum_i x f_i(x) = 1, \tag{1.5}$$

where the sum is taken over all quark flavours and gluons. In the case of the proton with quark composition uud the charge sum rules are:

$$\int_0^1 dx (f_u(x) - f_{\bar{u}(x)}) = 2 \tag{1.6}$$

$$\int_0^1 dx (f_d(x) - f_{\bar{d}(x)}) = 1 \tag{1.7}$$

$$\int_0^1 dx (f_s(x) - f_{\bar{s}(x)}) = 0 \quad , \tag{1.8}$$

and similar for the neutron. Based on the distribution functions which describe the initial state dynamics, we can express the total quark production cross section in an hadronic collision as

$$\sigma_{hh \to qq} = \sum_{i,j} \int_0^1 dx_1 dx_2 f_i(x_1) f_j(x_2) \sigma_{i,j} \quad , \tag{1.9}$$

where the σ_{ij} represent the partonic cross sections. Eq. 1.9 is based on the QCD factorization theorem [1, 2], which states that hard parton scattering can be to good approximation factorised from the initial state process. The hard scattering cross section can be computed within the framework of perturbative Quantum ChromoDynamics (pQCD) as long as the energies involved are large *i.e.* larger than the QCD scale, Λ_{QCD}, which will be discussed below.

1.2 Perturbative QCD

At short distances – or equivalently at high energies – it is possible to compute the cross section since the coupling constant α_s is small and the leading term of an expansion in α_s will give a good approximation of the exact result. Schematically, the expansion for a qq or gg interaction can be expressed as:

$$\sigma = \alpha_s^2(\sigma_0 + \alpha_s\sigma_1 + \alpha_s^2\sigma_2 + ...) \quad . \tag{1.10}$$

One refers to calculations up to σ_0 as leading-order (LO) or Born level calculations. Calculations up to σ_1 are referred to as next-to-leading-order (NLO), up to σ_2 as next-to-next-to-leading-order (NNLO), and so on.

The cross section is then calculated using the Feynman rules which are applied following the Feynman diagrams. Figure 1.2 shows all LO diagrams with a $q\bar{q}$ pair in the final state.

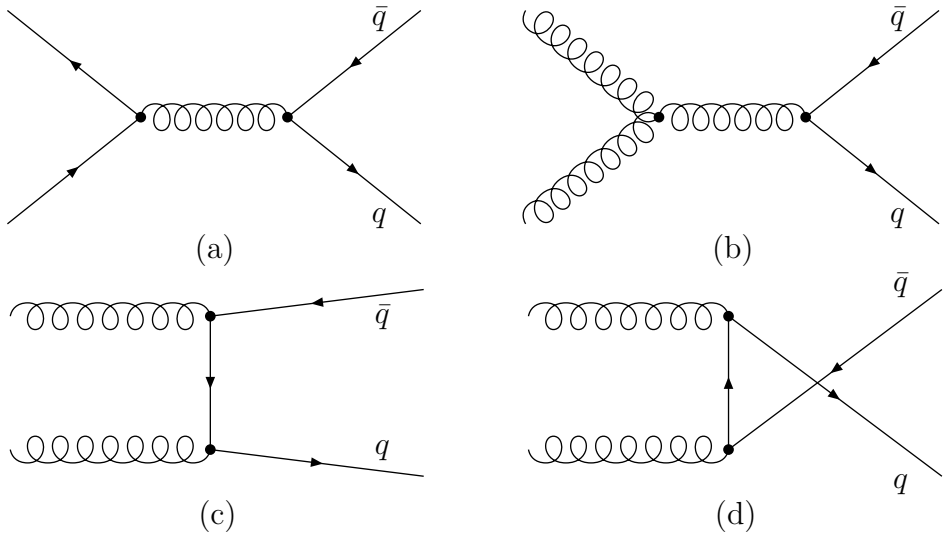

Figure 1.2: Leading order Feynman diagrams for $q\bar{q}$ production. Both quark-antiquark annihilation (a) and gluon fusion (b,c,d) contribute to the production cross section.

When higher order terms in the perturbative expansion are included, singularities

arise which must be treated to recover the predictive power of the theory. They can be summarised as follows:

- *Infrared and collinear divergences*: The emission of gluons (Fig.1.3a) by a quark introduces terms of the form
$$[\ E_q E_g(1-\cos\theta_{qg})\ ]^{-1} \tag{1.11}$$
into the cross section amplitude. Such terms diverge as the energy of the gluon vanishes ($E_g \to 0$) or if the quark and the gluon are collinear ($\cos\theta_{qg} \to 1$).

- *Ultraviolet divergences*: The virtual loops which appear in the propagators have no constraint on the momentum that "runs around". This leads to momentum integrals of the form
$$\int^{\infty} \frac{dp}{p}, \tag{1.12}$$
which diverge logarithmically for $p \to \infty$ (Fig.1.3b).

Figure 1.3 shows typical higher order Feynman diagrams that contribute to the mentioned divergences.

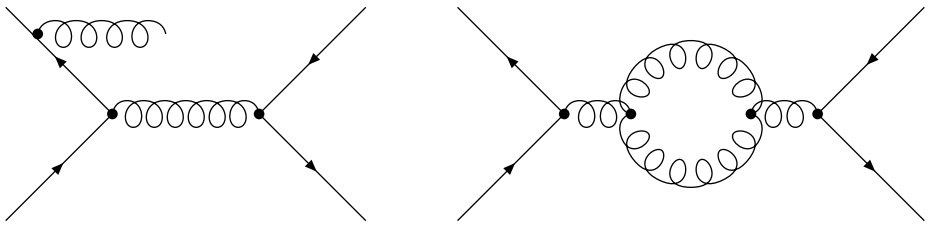

Figure 1.3: Higher order examples of QCD Feynman diagrams. a) Initial state gluon emission. b) Virtual loop diagram.

In the present work we do not discuss the contributions of qg interactions, since $q\bar{q}$ in qg interactions happen at higher orders in α_s and thus are suppressed in comparison to quark annihilation and gluon fusion [3, 4, 5, 6].

1.3 Renormalisation

We discuss now how the singularities can be removed consistently.

The ultraviolate divergences are handled during the calculations by a technique called "renormalisation". This technique is characterised by two steps. The first one is called regularisation which is a method to isolate the divergences. The second step is renormalisation, where the couplings, masses and fields are redefined in such a way that the

infinities cancel at each order. In this section we sketch the renormalisation technique defined by a "cut off" regularisation, as described in Ref. [7] [1]. In the regularisation, one applies an upper limit to the momentum integral of the virtual loops. Then one replaces the "bare" coupling constants by an effective or "renormalised" coupling. When performing the momentum integral of the virtual loop (Eq. 1.12) with an upper limit M, terms of the form

$$\sim C \ \ln(\frac{M^2}{Q^2}) \tag{1.13}$$

appear in σ_1 of Eq. 1.10. Here, C is a constant, Q is the invariant momentum of the interaction, and M is the upper cutoff limit of the integral 1.12. At the end of the calculation one must take the limit of $M \ \rightarrow \ \infty$.

In the following step one replaces the coupling constant by an effective one. The idea behind this technique is that the coupling constant which we naively assume in a certain vertex interaction (Figure 1.3 a), is in fact the sum of all possible processes like the ones shown in Figure 1.3 b and c.

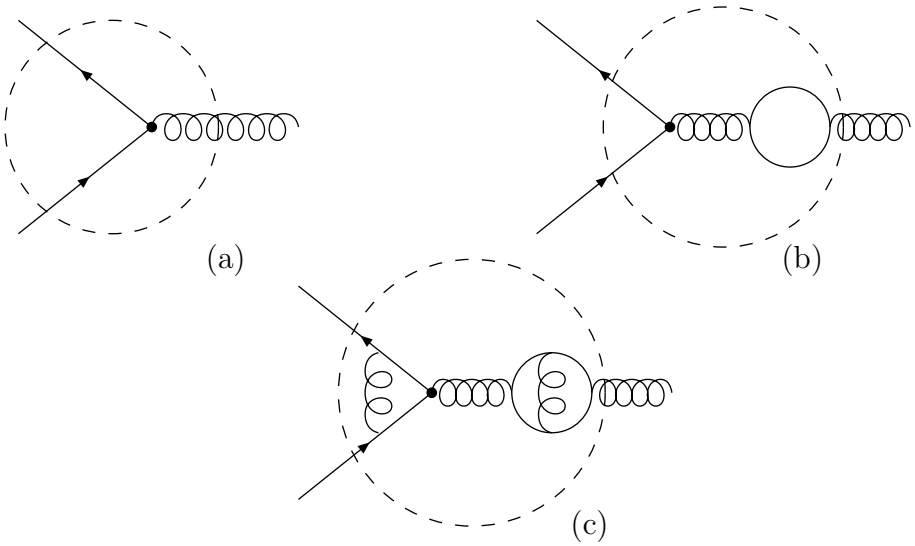

Figure 1.4: a) Naive picture of the coupling constant. b) and c) higher order diagrams contributing to the "renormalised" coupling.

The redefinition of the coupling constants introduces new terms of the form of Eq. 1.13. The new terms depend, too, on an energy scale μ (also called renormalisation scale μ_R), which in this case is not constrained or determined. As it is shown in Ref. [7], the new terms contribute with opposite signs to the ones coming from the loops. After combining them, we obtain

$$C \ \ln(\frac{M^2}{Q^2}) - C \ \ln(\frac{M^2}{\mu^2}) = C \ \ln(\frac{\mu^2}{Q^2}). \tag{1.14}$$

[1] At present, this is not the most commonly applied technique. Rather,the dimensional regularisation is used instead, where the momentum integrals are performed in a generic dimension "d" and then the limit "d = 4" is taken [8].

Summarising, the infinities in the loops compensate the infinities in the coupling. Similar procedures can also be applied to the mass and to the wavefunctions of the particles so as to absorb all singularities appearing at all orders for any cross section (see for example Ref. [9]).

The renormalisation of the theory leads to a scale dependent coupling constant (scale μ). This dependence can be derived at first order as [7]:

$$\alpha_s(\mu^2) = \frac{12\pi}{(33 - 2n_f)\ \ln \mu^2/\Lambda^2}\ , \tag{1.15}$$

where n_f is the number of flavours running around in a loop correction to the elementary vertex. From this equation we can see that at large energy scales, the effective coupling becomes small ("asymptotic freedom").

This also implies that at energies much larger than Λ the effective coupling is small and the perturbative expansion should converge reasonably fast. The value of Λ is not predicted by theory but must be determined experimentally. We can estimate α_s for our case at HERA – B assuming the production at threshold energy (~ 10 GeV) and $\Lambda^{udcs}_{\overline{\rm MS}} = 498$ MeV as determined in Ref. [10]. This results in $\alpha_s \sim 0.2$, a sufficiently small value to expect a proper description at the perturbative level.

We now turn to the *infrared singularities* caused by collinear and soft gluon emissions. The soft gluon divergences are found to cancel out when including real and virtual gluon emissions [11]. On the other hand, divergences due to the collinear gluon emission need again a special treatment. The main idea to handle these singularities is to factorise them out of the cross section and include them in the parton distribution functions. We show here schematically this procedure, as presented by P. Nason [12], where the cross section is expanded as:

$$\sigma_q = \sigma_0(p) + \sigma_1(p) = \left(\ \mathbb{I} + \frac{\alpha_s}{2\pi}\ \ln\left(\frac{Q^2}{\lambda^2}\right)\ P\ \right)\ \sigma_0(p) + \sigma_1^{finite}(p) \tag{1.16}$$

where p is the incoming quark four momentum and λ is the lower cut-off in the momentum integral that must be taken as $\lim \lambda \rightarrow 0$ (representing collinear emission), P is a non-divergent momentum splitting function, and $\sigma_0(p)$ and $\sigma_1(p)$ represent the leading and the next-to-leading components, respectively. On the right hand side of Eq. 1.16, the NLO component is factorised in a singular term proportional to the Born level component and a finite component. From now on we keep the singular terms of order α_s relative to the Born term. The main step of the procedure lies in the factorisation of Eq. 1.16 as:

$$\sigma_q = \left(\mathbb{I} + \frac{\alpha_s}{2\pi}\ \ln\left(\frac{\mu^2}{\lambda^2}\right)\ P\ \right)\ \sigma^{(0)}(p)\ \otimes\ \left(\ \mathbb{I} + \frac{\alpha_s}{2\pi}\ \ln\left(\frac{Q^2}{\mu^2}\right)P\ \right)\ \sigma^{(0)}(p), \tag{1.17}$$

the symbol $\otimes$ denotes the convolution of the two elements ($f \otimes g \equiv \int f(\tau)g(t-\tau)d\tau$). The factorisation can be verified by expanding the product of the terms in the parenthesis

retaining terms up to α_s and combining [2]:

$$\ln \frac{\mu^2}{\lambda^2} + \ln \frac{Q^2}{\mu^2} = \ln \frac{Q^2}{\lambda^2} \ . \tag{1.18}$$

The hadronic cross section, as already shown, is the convolution of the PDFs with the partonic cross sections $\sigma(p) = f \otimes \sigma_q(p)$. Based on Eq. 1.17 we can rewrite the convolution as:

$$\sigma(p) = f(\mu) \otimes \hat{\sigma}_q(p, \mu) \ , \tag{1.19}$$

where now

$$f(\mu) = f \otimes \left(\mathbb{I} + \frac{\alpha_s}{2\pi} \ \ln(\frac{\mu^2}{\lambda^2}) \ P \right) \tag{1.20}$$

and

$$\hat{\sigma}_q(p, \mu) = \left(\mathbb{I} + \frac{\alpha_s}{2\pi} \ \ln(\frac{Q^2}{\mu^2}) \ P \right) \ \sigma^{(0)}(p). \tag{1.21}$$

Now the factorisation of the divergent logarithms (Eq. 1.17) and the inclusion of the divergent part into the PDFs (Eq. 1.20) makes of the partonic cross section (1.21) a finite quantity. This procedure holds for any cross section, using the same splitting functions (P). This is the key benefit of the factorization and gives a predictive power to QCD in hadronic collisions. This factorisation leaves a residual new parameter or "scale" (μ) called the factorisation scale (μ_F), which appears both in the hard cross section and in the distribution functions. The distribution functions are not known analytically; however, their scale dependency can be determined and are described by the Dokshitzer-Gribov-Lipatov-Altarelli-Parisi (DGLAP) equations [14]. Therefore, once they are measured for a particular scale – they are determined by global fits to experimental data –, they can be derived for any other scale and applied to any other process because of their universality.

1.4 Scheme dependence and parton distribution functions

There is some ambiguity in the way the parton densities are defined (based on the first part of Eq. 1.17). In our example it can be seen as a different way of performing the factorisation which may introduce extra constants in the formulas. For every calculation the method must be clearly specified together with the procedure to compute the cross section. At present the most common one is the "modified-minimal-subtraction" scheme $\overline{\text{MS}}$ [15]. For the empirical parton distribution functions, there is no common approach to perform global fits to the data of different experiments. Several groups provide parton distribution functions which are updated when new data or theoretical calculations

[2] We show here schematically the treatment of the collinear divergences up to leading order in perturbation theory only. There is a variety of more complex arguments for higher order terms, all included in the factorisation theorem [13] which states that Eq. 1.17 holds at all orders.

become available. In the results presented in the next sections, parton distributions are used as developed by three different groups. They are commonly indicated as CTEQ (Coordinated Theoretical-Experimental project on QCD) [16], MRST (Martin, Roberts, Stirling, Thorne) [17], and GRV (Glück, Reya and Vogt) [18]. A comparison of the different approaches and their prediction for HERA data can be found in Ref. [19].

1.5 Heavy quark production at threshold

At present, several full calculations up to NLO in perturbation theory are available [3, 4, 5, 6, 20]. For the perturbative expansion to converge rapidly, it is necessary that α_s is small. Still, in specific kinematic regions, large logarithms in the coefficients of the perturbative expansion spoil its convergence. This means that a full calculation at NLO might not yet be good enough since large corrections could still be caused at higher orders. They could appear in different observables, such as :

- the total cross section:
  - At very high energy, one expects terms like $[\alpha_s \ln s/m_q^2]^n$ to arise at all orders in perturbation theory. This problem is relevant for bottom production at Tevatron and LHC energies.
  - At threshold for the production of heavy quarks, terms like $[\alpha_s \ln^2(1-4m_q^2/s)]^2$ arise. Such terms are relevant for top production at the Tevatron or for bottom production at HERA – B .
- differential distributions:
  - For example at high transverse momentum, terms like $[\alpha_s \ln^2(p_T/m_q)]^n$ arise at all orders.

In the present work, we are interested mainly in the problems that arise in the calculation of the total cross section. At HERA – B , b pairs are produced near threshold, thus logarithmic terms arising at higher orders than NLO cannot be neglected since they have an important contribution to the total cross section. We will briefly point to ways how these logarithmic terms can be included.

We now rewrite the total cross section 1.9 including the renormalisation parameter in the factorisation formula (following the notation of [21], where the location of the large logarithms becomes explicit):

$$\sigma(\rho_h, m^2) = \sum_{i,j} \int_0^1 dx_1 dx_2 \; F_i(x_1, \mu^2) F_j(x_2, \mu^2) \; \hat{\sigma_{ij}} \left(\rho; m^2, \alpha_s(\mu^2), \mu^2\right) \; . \tag{1.22}$$

Here, m is the mass of the heavy quark, i and j denote parton indices ($i, j = q, \bar{q}, g$), and the dimensionless variables ρ and ρ_h are

$$\rho_h = \frac{4m^2}{s} \ , \rho = \frac{\rho_h}{x_1 x_2} \ , \tag{1.23}$$

where s is the square of the center of mass energy. The parton densities $F_i(x_1, \mu^2)$ and the partonic cross sections $\hat{\sigma_{ij}}$ depend on the factorisation scale, which is set to be equal to the renormalisation scale. Note that they also depend on the factorisation scheme. Here we use the "modified-minimal-subtraction" $\overline{\text{MS}}$ scheme. The partonic cross section can be written in terms of dimensionless functions f_{ij} (which should not be confused with the PDFs $f_i(x)$ of Eq. 1.9):

$$\hat{\sigma_{ij}}\left(\rho; m^2, \alpha_s(\mu^2), \mu^2\right) \equiv \frac{\alpha_s^2(\mu^2)}{m^2} f_{ij}\left(\rho; \alpha_s(\mu^2), \mu^2/m^2\right) \ , \tag{1.24}$$

with

$$\begin{aligned} &f_{ij}\left(\rho; \alpha_s(\mu^2), \mu^2/m^2\right) = \\ &f_{ij}^{(0)}(\rho) + 4\pi\alpha_s(\mu^2)\left[f_{ij}^{(1)}(\rho) + \bar{f_{ij}^{(1)}}(\rho)\ln\frac{\mu^2}{m^2}\right] + \sum_{n=2}^{\infty}\alpha_s^n(\mu^2) f_{ij}^{(n)}(\rho; \mu^2/m^2), \end{aligned} \tag{1.25}$$

where the LO terms $f_{ij}^{(0)}(\rho)$ as well as the NLO contributions $f_{ij}^{(1)}(\rho)$ are explicitly known. Multiple-gluon radiation at higher perturbative orders leads to stronger logarithmic corrections and the coefficient function $f_{ij}^{(n)}(\rho; \mu^2/m^2)$ in Eq. 1.25 behaves as:

$$f_{ij}^{(n)}(\rho; \mu^2/m^2) \sim f_{ij}^{(0)}(\rho) ln^{2n}\beta^2, \tag{1.26}$$

with $\beta \equiv \sqrt{1-\rho}$. Such terms diverge as β vanishes ($\rho \to 1$) in the near threshold limit. This causes problems for the convergence of the perturbative expansion in this limit.

1.6 Soft gluon resummation

To be able to recover the predictive power of the calculation in the region near threshold, different techniques are developed to organise the large logarithms in a way that they can be "resummed" at all orders. To understand the meaning of resummation we first rewrite once more the cross section, now in the following schematic simplified form:

$$\sigma = 1 + \alpha_s(L^2 + L + 1) + \alpha_s^2(L^4 + L^3 + L^2 + L + 1) + ... \tag{1.27}$$

where L is a potentially large logarithm. In this notation, for terms of order α_s^n, the leading-logarithm order (LL) refers to the L^{2n} component. The next-to-leading-order

(NLL) includes terms at L^{2n-1}, and so on. The L terms can be often resummed, *i.e.* reorganised, into functions whose expansions will reproduce Eq. 1.27. A typical organisation could be as follows:

$$\sigma = \sigma_0 \ \times \ \exp\left[L\ g_1(\alpha_s\ L) + g_2(\alpha_s\ L) + O(\alpha_s\ (\alpha_s\ L)^k)\right] \tag{1.28}$$

where $g_{1,2}$ can be expanded in terms of $\alpha_s\ L$. At present there are two estimates of higher order logarithmic terms. The first one is due to Kidonakis, Laenen, Moch and Vogt and includes terms up to NNLO-NNLL [22] and more recently up to NNLO-NNNLL [23]. In this approach, the cross section is factorised in a way such that the different large contributions are individualised separately. Each of these terms is then resummed and expanded perturbatively. Finally, the expansions are convoluted together keeping terms up to NNLO-NNLL. It is checked that this new expansion matches the exact LO calculations and also those for NLO. By forcing this last match, some terms which are not known analytically in the NNLO expansion, can be deduced. This method is less sensitive to the renormalisation scales, as shown in Figure 1.5, which indicates an improved predictive power of the calculation. In this calculation two different descriptions of the kinematic of the final state are tested; a one particle inclusive (1PI) kinematics and a pair-invariant mass (PIM) kinematics.

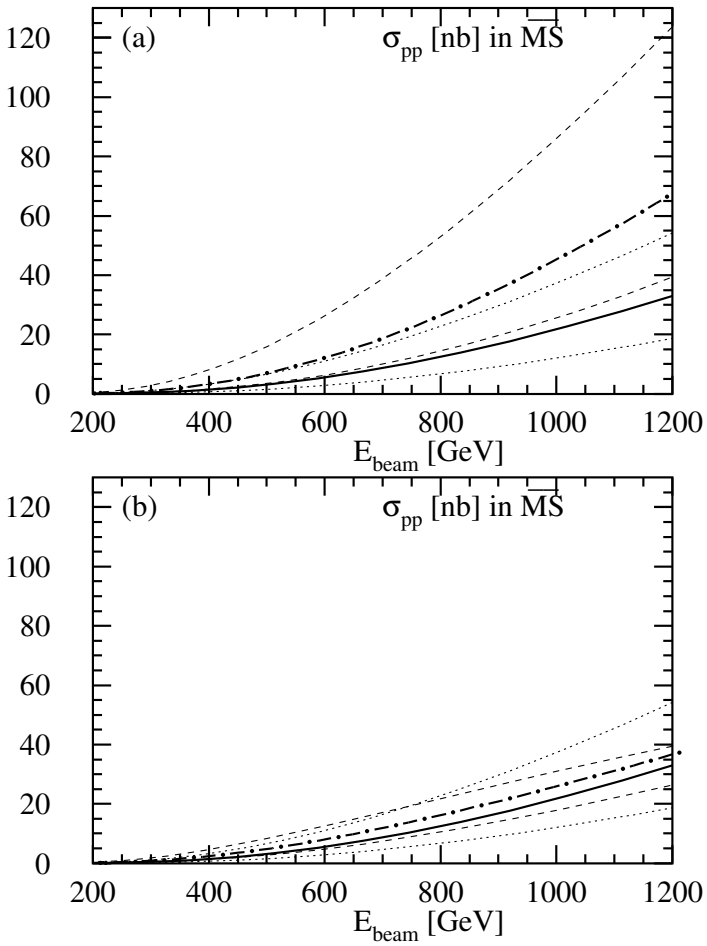

Figure 1.5: Total $b\bar{b}$ cross section (in the $\overline{\text{MS}}$ scheme) at fixed target pp experiments vs. beam energy, with m_b=4.75 GeV, taken from [22] a: One particle inclusive (1PI) kinematics. b: Pair invariant mass (PIM) kinematics. The exact NLO cross section is shown for $\mu = m_b$ (solid lines), $m_b/2$ (upper dotted lines) and $2m_b$ (lower dotted lines). The NNLO-NNLL cross section is shown for $\mu = m_b$ (dashed-dotted lines), $m_b/2$ (upper dashed lines) and $2m_b$ (lower dashed lines).

In the other approach to include large logarithms, due to Bonciani, Catani, Mangano and Nason [21], one adds to the exact NLO calculation the NLL contribution at all orders in the α_s expansion, *i.e.* there is no expansion after the resummation. Figure 1.6 shows the improvement of these enhanced calculations, in which the dependence on the unphysical renormalisation scale is reduced by including the large logarithmic contributions.

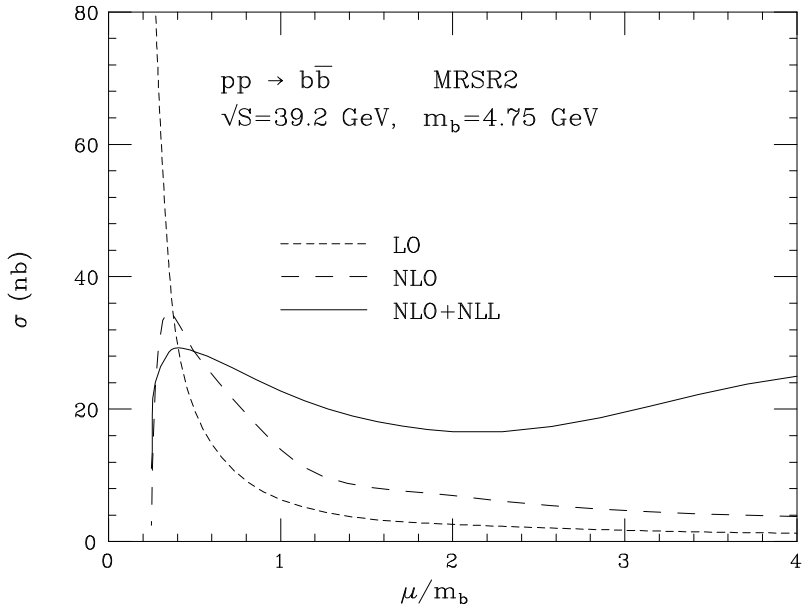

Figure 1.6: Scale dependence of the $b\bar{b}$ cross section determined with the MRSR2 parton distribution function. Different order perturbative calculations are shown, taken from [21]. The reduced dependence when including higher order terms is seen, reflecting the increasing accuracy of the prediction. The c.m.s energy was determined considering the old HERA proton beam energy of 820 GeV. For comparison with HERA – B measurement the values are updated to the present energy (920 GeV).

1.7 Cross section prediction

The result from Kidonakis *et al.*, at NNLL-NNLO, $\sqrt{s} = 41.6$ GeV and using CTEQ5 partons functions is

$$\sigma(b\bar{b}) = 30\pm12 \text{ nb/nucleon} . \tag{1.29}$$

Based on the same technique but including terms up to NNNLL-NNLO and taking parton distributions from MRST and GRV98 one obtains, respectively:

$$\sigma(b\bar{b}) = 28\pm15 \text{ nb/nucleon} , \tag{1.30}$$

$$\sigma(b\bar{b}) = 25\pm13 \text{ nb/nucleon} . \tag{1.31}$$

The uncertainties in the calculation come from the dependence on the renormalisation scale μ (which was evaluated at three different values, $m_b/2$, m_b and $2m_b$, the mass m_b of

the b-quark is assumed to be 4.75 GeV) and the choice of the final state kinematics. In this calculation two different descriptions of the kinematic of the final state are tested; a one particle inclusive (1PI) kinematics and a pair-invariant mass (PIM) kinematics.

The approach of Bonciani *et al.* , at HERA – B energy, including orders up to NLO + NLL and using the most recent MRST distributions, results in:

$$\sigma(b\bar{b}) = 25^{+20}_{-13} \text{ nb/nucleon} . \tag{1.32}$$

Here, the uncertainties come from the dependence of the calculation on the parameter μ, where three typical values were tested ($m_b/2$,m_b and $2m_b$), and the unknown mass of the b quark, for which three different values (4.5, 4.75 and 5.0 GeV) were assumed.

At present there are three measurements at fixed target experiments at similar energies. They use two different techniques for the measurements: the identification of $b \to J/\psi X$ inclusive decays [24, 25] and the counting of simultaneous double semileptonic b decays into muons [26].

Experiment	Year	Target	Proton energy	$\sigma(b\bar{b})$ nb/nucleon	Method	Ref.
E789	1995	Au	800 GeV	$5.7 \pm 1.5 \pm 1.3$	$b \to J/\psi$	[24]
E771	1999	Si	800 GeV	$43^{+27}_{-17} \pm 7$	$b\bar{b} \to \mu\mu$	[26]
HERA – B	2002	C/Ti	920 GeV	$32^{+14\ +6}_{-12\ -7}$	$b \to J/\psi$	[25]

Table 1.1: The present experimental knowledge of the $b\bar{b}$ cross section in pN interactions.

The measurements of E789 and E771 were performed at the same energy and they differ by a factor of 7, but uncertainties are still large.

1.8 Hadronisation

The quarks must be confined into colourless hadrons, which means that after their production they must go through a fragmentation and hadronisation process with unit probability. The hadronisation process involves interactions at high α_s so that it cannot be treated perturbatively, and no calculations are thus available. Rather one uses experimental fragmentation functions D which have been largely obtained in the clean environment of e^+e^- collisions. The differential hadron cross section can be written as:

$$\frac{d\sigma}{dz}(e^+e^- \to hX) = \sum_q \sigma(e^+e^- \to q\bar{q}) \; [D_q^h(z) + D_{\bar{q}}^h(z)] . \tag{1.33}$$

It describes the differential cross section of producing a hadron h carrying a fraction z of the generated quark ($z \equiv \frac{E_h}{E_q}$). The fragmentation functions $D_q^h(z)$ describe the

probability of a hadron h to be formed with a fraction z of the energy of the quark q and must satisfy the probability and momentum constraint

$$\sum_h \int_0^1 z D_q^h(z) dz = 1 \ . \tag{1.34}$$

Possible parametrisations of the fragmentation function for heavy quarks are:

$$\text{Peterson[27]} : D_b^h(z) \propto \frac{1}{z} \cdot \left(1 - \frac{1}{z} - \frac{\epsilon}{1-z}\right)^{-2}; \tag{1.35}$$

$$\text{Kartvelishvili[28]} : D_b^h(z) \propto z^\alpha \cdot (1-z). \tag{1.36}$$

Of these, the Peterson functional is the most commonly used parametrisation. Figure 1.7 shows the fragmentation fraction parametrisations together with experimental data from ALEPH collaboration [29]. The hardness of the fragmentation function for the bottom distribution is clearly visible (as it has its maximum close to one).

1.9 J/ψ production

The production of a $c\overline{c}$ pair follows a similar process as the one described for $b\bar{b}$ since it can be treated perturbatively ($m_c > \Lambda_{QCD}$). Most of the pairs will hadronise into a $D\bar{D}$, and only a small fraction ($\sim 5\%$) will form a charmonium state. The charmonium formation process is not completely understood at present, and there are three models proposed to describe this process (see a summary in Ref. [30]). The Colour Singlet Model (CSM) [31, 32] assumes that the $c\overline{c}$ is created in a colour singlet state with the same quantum numbers as the final charmonium state. This implies for the J/ψ state with charge conjugation C = -1, that the first order diagram must radiate a gluon, thus restricting the production to $O(\alpha_s^3)$. At present this model fails to reproduce the measurements, which may be interpreted as a hint that octet states may be the main contribution to charmonium production.

The other two models, the Colour Evaporation Model (CEM) [33, 34] and the Colour Octet model based on Non-Relativistic QCD (NRQCD) calculations [35, 36, 37, 38, 39, 40, 41] assume an initial $c\overline{c}$ pair in both octet or singlet colour states. Only after a non-perturbative process the $c\overline{c}$ pair form a charmonium state. The CEM assumes multiple gluon radiation before the formation of the bound state, by which all information on the state in which the initial $c\overline{c}$ pair was generated is lost. This model cannot make a prediction of the absolute cross section since the functions describing the multiple gluon radiation are not known. However, it can predict the relative production ratios of different charmonium states, which seem to be in agreement with observations. The NRQCD

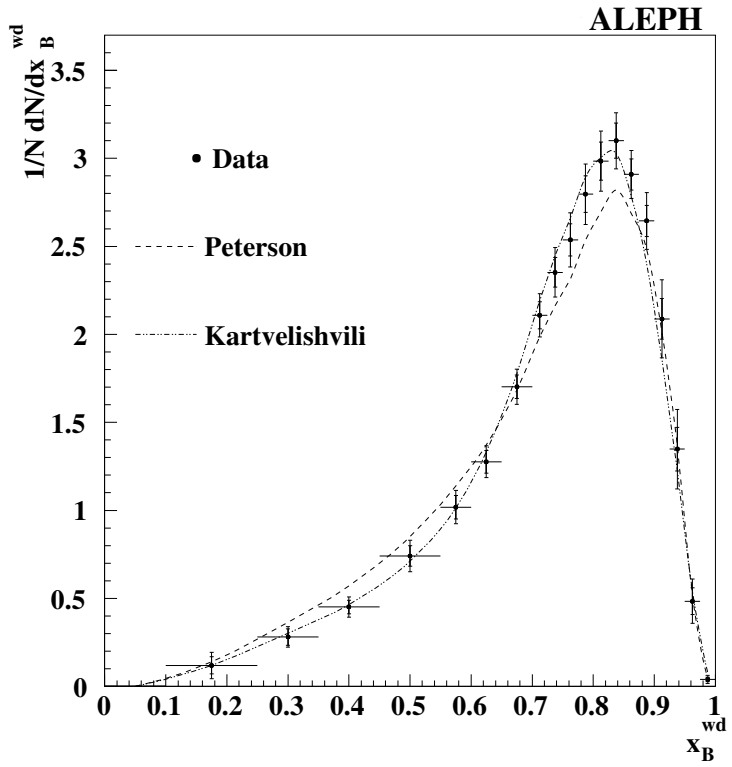

Figure 1.7: ALEPH results on b quark fragmentation with the best fitting Peterson and Kartvelishvili shapes, taken from [29]. The variable x_B^{wd} ($\approx z$) indicates fraction of energy of weakly decaying B mesons, corrected by detector acceptance and resolution.

derives transition probabilities to form a final charmonium state for different initial colour states. This model includes several free parameters that limit its predictive power. It successfully describes the J/ψ p_T distributions but fails to describe the results of CDF on the J/ψ polarization at high p_T [42].

However, the J/ψ cross section is well supported by several measurements at different center of mass energies. Figure 1.8 shows the different meaurements fitted with a function of the form $F = ae^{-b\sqrt{\tau}}$ with $\tau = M_{J/\psi}^2/s$ [43].

1.10 Nuclear dependence

In proton nucleus collision the dependence of the production cross sections on the mass number A of the target nucleus is commonly parameterised as:

$$\sigma^A = \sigma_0 \times A^\alpha \ , \tag{1.37}$$

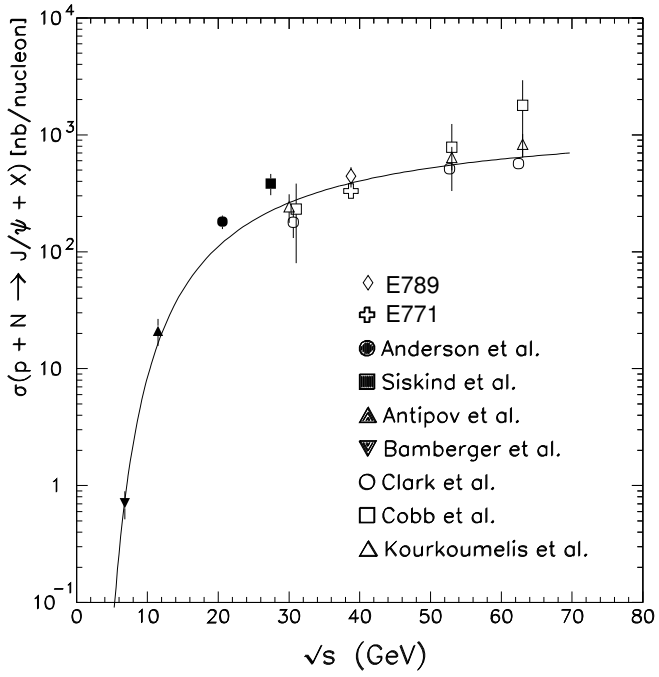

Figure 1.8: J/ψ cross vs. $\sqrt{s}$, measured by different experiments. The solid line corresponds to the phenomenological fit described in the text, taken from [43]

where σ_0 stands for the proton nucleon cross section. For the case that the nucleus is nothing but a collection of independent nucleons, one expects $\alpha = 1$. The interaction between the projectile nucleon and the target nucleons actually takes place in a nuclear environment which may affect the incoming nucleon as well as the hadronisation process after the interaction. If this plays a role, α is expected to differ from unity depending on the process under study. In the case of open $b\bar{b}$ and $c\bar{c}$ production no influence of the nuclear environment is expected [44]. In open $c\bar{c}$ production (D meson production) α has been measured [45] and is consistent with unity; in $b\bar{b}$ production, no measurement has been reported. In our analysis we will assume $\alpha = 1$ for $b\bar{b}$ production.

The situation is different for J/ψ production since the $c\bar{c}$ pair must form a bound state after the production step. A key issue is if the $c\bar{c}$ pair is produced in a color neutral state or not. If the pair is not generated in a color neutral state, radiation of soft gluons and interactions with nuclear matter may generate the required transition to a neutral state. On the other hand, the presence of many quarks (valence and sea quarks) can lead to an enhancement of open charm at the expense of $c\bar{c}$ states. The mechanism is not completely understood, but measurements of the E866 collaboration [46] which are carried out at a beam energy of 800 GeV, not too different from the one used at HERA – B , set the value of α at 0.96 ± 0.01 in the range of $0.0 < x_F < 0.2$.

Chapter 2

The HERA – B experiment

In this chapter we present an overview of the HERA – B detector together with a short historic review and the updated physics goals. After the detector description the trigger and data acquisition systems are presented as they were used in the 2002-2003 set up.

2.1 Motivation and history

The HERA – B proposal [47] was presented in May 1994 and the Technical Design Report (TDR) followed in January 1995 [48]. The first goal of the project was to measure CP violation through the $B^0 \to J/\psi\, K^0_S$ decay channel, which is shown schematically in Figure 2.1. This decay process is chosen for its clean signature combined with the fact that the extraction of CP violating parameters is especially clean. However, the cross section of this process is suppressed by a factor of 10^{-11} compared to the inelastic cross section. In order to deal with this huge suppression, the lay-out of the detector was tailored to detect with good efficiency the final state particles of just this process, and to suppress through a fast and complex trigger logic the unwanted event rate. The final state reconstruction requires a good lepton identification of both muons and electrons, originating from the decay of the J/ψ and a good K^0_s identification over a high pion background.

Due to the low count rate of the $B^0 \to J/\psi\, K^0_S$ channel, a collection of relevant statistics ($\sim$ 1000 per year) requires a high luminosity together with a highly selective trigger. To increase the interaction rate above the 10 MHz frequency of HERA, a target system is required which allows the study of several interactions per bunch crossing. The trigger requirements lead to a highly ambitious hardware system that selects J/ψ events at an early stage of the selection process.

The assembly of the experiment started in 1998 and finished in the year 2000; this was about two years later than scheduled. In the mean time the competitors for the measurement of CP violation (BaBar and Belle) were in an advanced stage to provide a

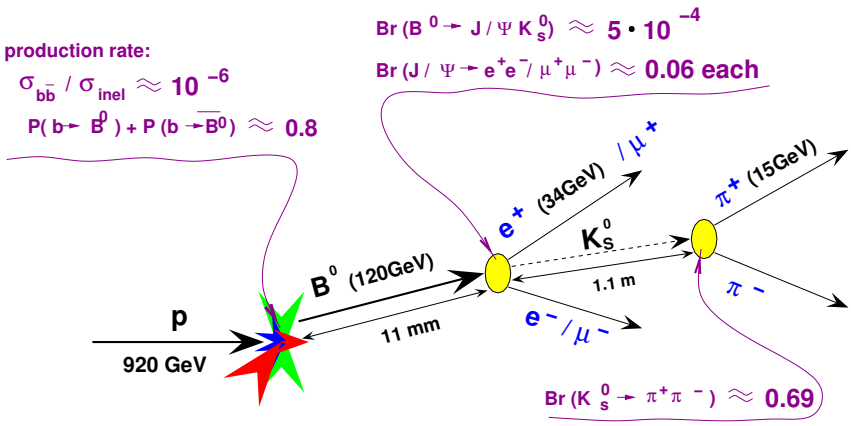

Figure 2.1: Schematic view of the golden decay. Indicated are some typical parameters for the kinematics at HERA – B and some relevant branching ratios.

measurement with a statistical precision [49, 50] well beyond HERA – B capabilities. In addition, it turned out that some assumptions in the construction of HERA – B , such as the possibility to run at an interaction rate of 40 MHz, had been overoptimistic, and that the commissioning of some subsystems, especially the crucial first level of the trigger, were especially time consuming. Last but not least, the shutdown of the HERA accelerator complex, which started in mid-2000, took longer than foreseen, and prevented a timely restart of the experiment. All these conditions together obliged the HERA – B collaboration to reevaluate its physics program and concentrate the efforts on other relevant topics in which the HERA – B detector could still make a valuable contribution. The updated physics goals are summarised in Ref. [51]. At the end of the much prolonged shut-down of HERA, HERA – B restarted data taking in October 2002, but with rather unstable beam conditions due to problems with the HERA machine. Ultimately, a new shut-down at the beginning of March 2003 lead to the decision that HERA – B would have to be stopped definitively.

We give here a short summary of the presently most advanced studies on the HERA – B data:

- Measurement of $\sigma_{b\bar{b}}$: This is a relevant quantity to test the predictive power of QCD. The analysis of this measurement is the subject of this thesis.
- Measurement of J/ψ , ψ' and χ_c production, decay angular distribution and A dependence: At present the production of charmonium is not completely understood and there are different models to describe the production, such as the Color Singlet Model (CSM) [31], the Color Evaporation Model (CEM) [33] [34], and the Non-Relativistic

QCD approach (NRQCD) [35] [40]. A precise understanding of the J/ψ production is also of particular interest since its suppression has been predicted in the regime of the Quark-Gluon-Plasma (QGP) [52]; however, before it is possible to use a possible suppression as evidence that the QGP regime is obtained, the production mechanism in "normal" nucleus-nucleus collisions must be understood. HERA – B provides information in the transition region from nucleon-nucleon to nucleus-nucleus interactions.

With the HERA – B data of the commissioning run in 2000, a result on the fraction of J/ψ from a χ_c radiative decay was published [53] which favours NRQCD models. With 2002-2003 data, HERA – B is able to improve this result with a significantly enhanced statistical precision. Since HERA – B can run simultaneously with two different materials, it can provide valuable data on nuclear suppression effects, with reduced systematic uncertainties.

- Measurement of Υ production [54]: As in the case of charmonium, bottonium production provides an opportunity to investigate quarkonium production models.

- Measurement of the upper limit $D^0 \to \mu^+\mu^-$ branching ratio: The Standard Model (SM) prediction of the branching ratio is of the order of 10^{-19}. The clean signal of this channel and the strong suppression predicted by the SM make this channel an interesting test-case for new physics such as supersymmetric theories (SUSY), which predict a significantly smaller suppression. HERA – B sets a new upper limit of 2.0×10^{-6} at 90% confidence level [55].

- Measurement of strangeness production (K_s, Λ, $\bar{\Lambda}$): A possible signature of a quark gluon plasma in nucleus-nucleus collisions is the enhancement of particles with strangeness. HERA – B already measured production ratios, based on the year 2000 data, finding no dependence on target materials [56], *i.e.* no nuclear dependence in the ratios.

- Measurement of direct photon production at high transverse momentum: In hadronic collisions the process $qg \to q\gamma$ is an important source of photons with high p_T. This process which is sensitive to the gluon density, allows the measurement of the gluon structure of the nucleon.

- Pentaquark production: Recently, several experiments reported the evidence of possible bound states of five quarks ("Pentaquarks") [57, 58, 59, 60, 61, 62, 63] . HERA – B searched for the $\Theta^+ \to K_s + p$ and $\Xi^{--} \to \Xi^-\pi^-$, in the high statistics data sample taken in the running period 2002-2003. In both decays, results are compatible with no signal [64].

2.2 DESY and HERA

The HERA – B detector was located at the Deutsches Elektron SYnchrotron (DESY) facility in Hamburg (Germany). The Hadron Electron Ring Anlage (HERA) is a storage ring of 6336 m circumference that provides protons of up to 920 GeV and electrons and

positrons of up to 27.5 GeV. The particles are preaccelerated by a linear accelerator (LINAC) and then injected into the Positron Elektron Tandem Ring Anlage (PETRA). The electrons are accelerated up to 12 GeV and the protons up to 40 GeV, before being injected into HERA. The protons are guided at HERA by superconducting magnets, while the light electrons are guided by normal conducting magnets. The two beams collide at two interaction points where two "general purpose" detectors, H1 and ZEUS are situated. The third experiment, HERMES, studies the proton spin structure. At present it uses a polarised electron/positron beam to collide with a polarised gaseous target. HERA – B , the fourth detector, was located in the west hall of the storage ring and makes use only of the proton beam. The proton ring contains space for 220 bunches ($\sim 10^{11}$ protons each) which are separated by 96 ns. Usually, up to 180 bunches are filled.

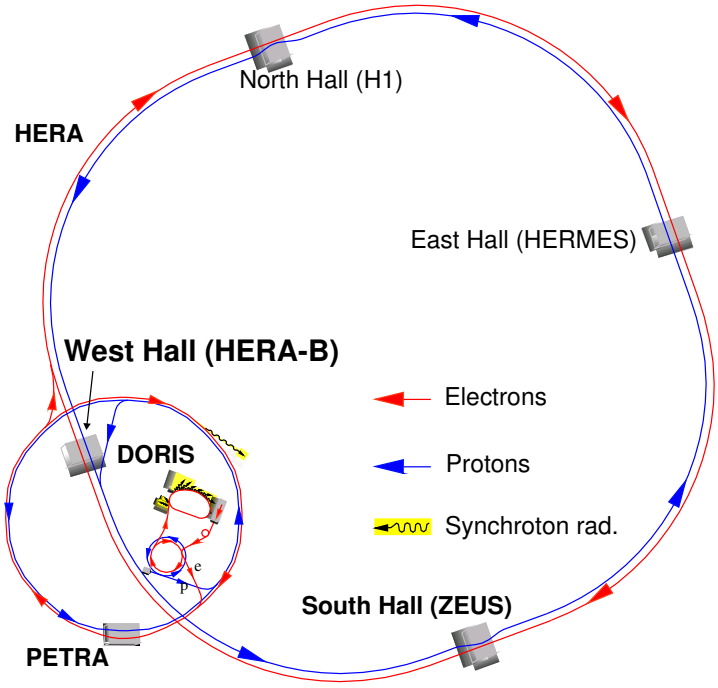

Figure 2.2: A schematic lay-out of the HERA storage rings. Protons are accelerated to 920 GeV and electrons-positrons to 27.5 GeV. At HERA – B , protons collide with a fixed nuclear target at a center of mass energy $\sqrt{s} = 41.6$ GeV.

2.3 The HERA – B detector

HERA – B is a forward spectrometer detector built to study collisions of protons at 920 GeV with different fixed target materials. It operates in the halo of the proton beam. This allows the production of collisions without interfering with the core of the beam used by the collider experiments (ZEUS and H1).

The detector presents an angular coverage of 220 mrad in the bending plane (x) and 160 mrad in the perpendicular non-bending (y) plane. Figure 2.3 shows a schematic view of the detector. From left to right we have the target system where the primary interactions take place. A silicon vertex detector (VDS) determines the position of primary and secondary vertices. The magnet, which provides a vertical magnetic field, is placed after the vertex detector to determine the momentum of the charged particles. The first tracking stations[1] composed of an inner (ITR) and an outer (OTR) part positioned after the magnet and before a Cherenkov detector (RICH) which is used for hadron identification. After the Cherenkov detector the second set of tracking stations are positioned. The two last detectors which are used for lepton identification are the electromagnetic calorimeter (ECAL) and the muon (MUON) detectors. In the following we detail each of these components.

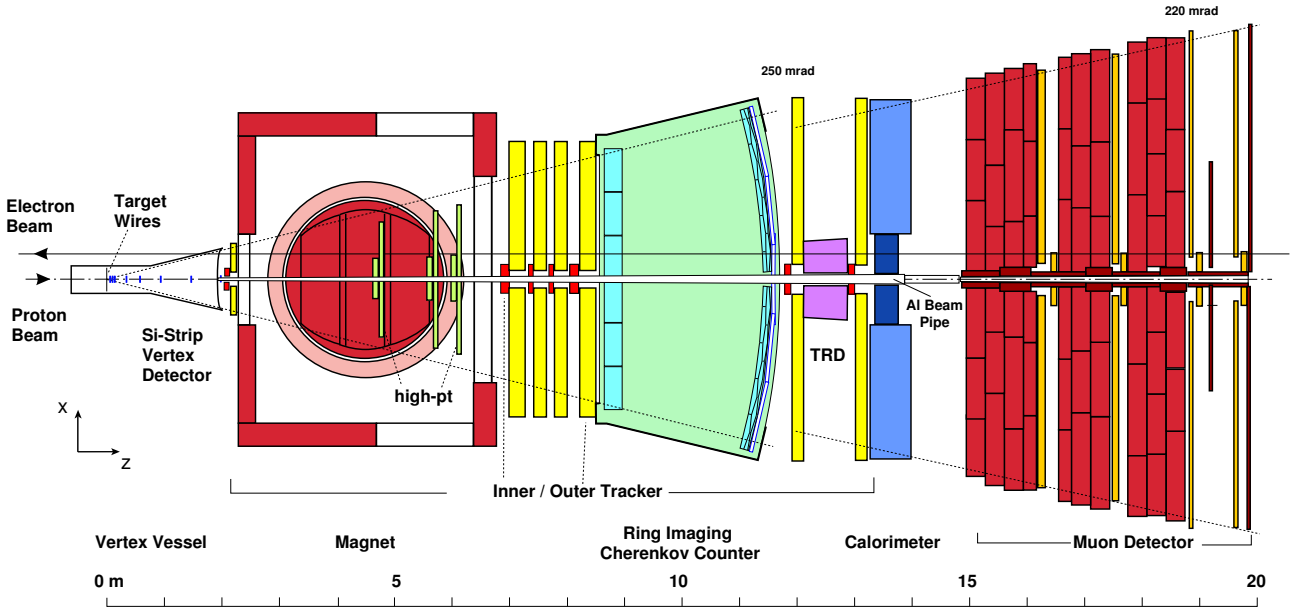

Figure 2.3: Schematic top view of the HERA – B detector

2.3.1 The target system

The target system consists of two stations of four wires each, surrounding the proton beam line (Fig. 2.4). It has the possibility to move all wires independently and simultaneously. In fact, the wires are not put into the proton beam itself, since this would disturb the beam and the collider experiments, not to speak of the damage to the HERA – B detector itself. Rather, the wires are moved only into the halo of the beam. This allows one to adjust the total interaction rate above or below the 10 MHz bunch crossing frequency. During the 2002-2003 data taking, no more than two wires were used simultaneously in

[1] In HERA – B internal nomenclature a station is called superlayer. A superlayer is composed of several layers at different angles. In this thesis we will indistinctively refer them as stations or superlayers.

order to avoid occupancy problems and to make the off-line analysis easier in the cases when it is crucial to know on which wire the primary interaction occurred.

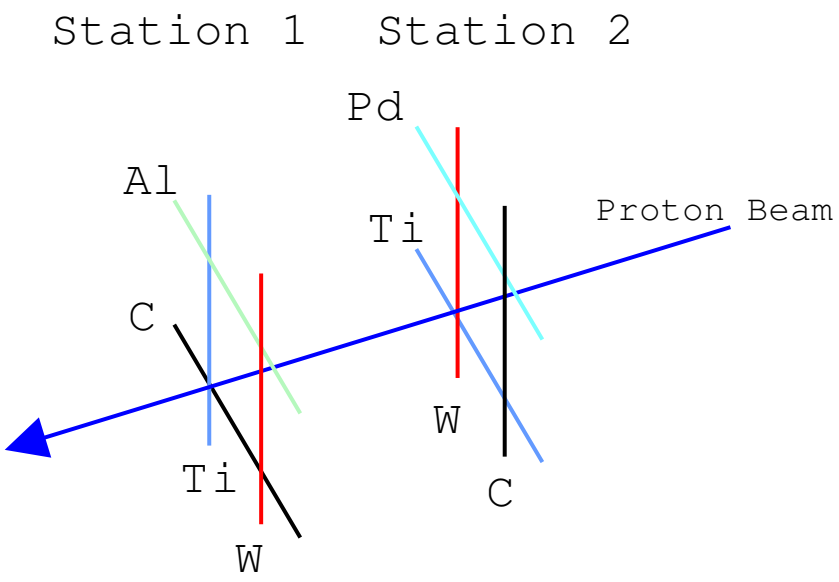

Figure 2.4: Schematic view of the target system. Wire materials are shown as of January 2003.

Five different materials were present as target wires, but only C, W, and Ti were used during data taking. These three materials were chosen since they cover a wide range of atomic numbers. The other wires were were not used in order to avoid further fragmentation of the limited statistics. The possibility of using simultaneously different target materials permits the study of the A dependence of cross sections with reduced systematics uncertainties, since both materials are active in (almost) exactly equal experimental conditions, and only the luminosity normalisation might be different. Table 2.1 shows the geometrical shapes and the distributions of the different materials in the two target stations. During the data taking period it was necessary on two occasions to replace broken wires. The wires broke due to misplacement of the proton beam, so that they received a direct hit for a short period of time, which was sufficient to overheat the wires and break them.

2.3.2 Vertex detector

The Vertex Detector System (VDS) is used to reconstruct vertices and impact parameters with sufficient precision to separate long lived particles (with decay lengths of a few mm) from primary interactions. For decays of B mesons a resolution better than 10% of the mean decay length ($\sim$ 9 mm) is desirable. The VDS consists of 8 layers of silicon microstrip detectors as shown in Figure 2.5, with a pitch of 50 μm. It is arranged perpendicular to the beam direction in a Roman pot system such that the detectors can be retracted during injection and steering of the proton beam. The VDS is located inside a vessel at a secondary vacuum of 10^{-6} mbar, separated by an aluminium foil from the primary beam

Name	Abbreviation	Material	A atomic weight	Shape	Dimension (mm)
Inner 2	I2	Carbon	12.01	Ribbon	0.1 × 0.5
Outer 2	O2	Tungsten	183.84	Ribbon	0.05 × 0.5
Bottom 2	B2	Titanium	47.87	Cylinder	0.025
Top 2	T2	Palladium	106.42	Cylinder	0.025
Inner 1	I2	Tungsten	183.84	Cylinder	0.025
Outer 1	O2	Titanium	47.87	Cylinder	0.025
Bottom 1	B1	Carbon	12.01	Ribbon	0.1 × 0.5
Top 1	T1	Aluminium	26.98	Ribbon	0.05 × 0.5

Table 2.1: Wire specifications including material, shape and position information for each wire as of January 2003.

vacuum of 10^{-9} mbar. To prevent radiation damage of the detectors a minimal distance to the beam is required. It was estimated that at a radial distance of 10 mm the VDS would remain operational for one year of HERA – B data taking. In the 2002-2003 run the VDS achieved its design performance providing a 500 μm vertex resolution in the beam direction and 60 μm in the perpendicular plane.

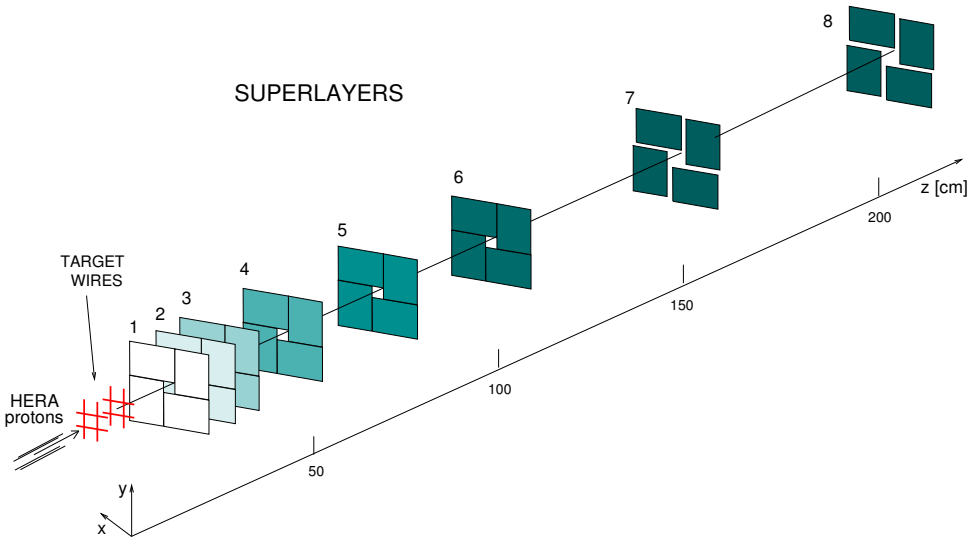

Figure 2.5: Schematic of the VDS, consisting of 8 layers of silicon micro strip detectors perpendicular to the beam direction, each of them arranged in a Roman pot system

2.3.3 The magnet

The HERA – B magnetic field is provided by a normal conducting magnet which provides an integrated field strength of 2.2 Tm in the vertical (y) direction. It is placed after the VDS and before the tracking chambers. An iron skirt at the entrance of the magnet protects the VDS from the magnetic fields. An important issue is the shielding of the electron beam pipe that transverses the detector. In order to preserve the beam polarisation, fields must be shielded. To achieve this two high metal permeability pipes were placed as passive shielding around the electron beam pipe.

2.3.4 The inner tracker

The Inner Tracker (ITR) covers the radial distance from the beam pipe up to 25 cm. To provide the necessary granularity and resolution it uses Microstrip Gas Chambers (MSGC) together with a gas electron multiplier (GEM) as shown in Figure 2.6. The strip pitch is 300 μ, which gives a spatial resolution of 80 μm. To provide 2 dimensional spatial information it has layers at three different angles; -5, 0 and 5 degrees [2]. Unfortunately, the performance during the 2002-2003 data taking period was lower than required. The ITR also showed unstable performance on a run by run basis, which makes Monte Carlo simulations quite difficult. Based on these facts it was decided not to include this detector in the present analysis.

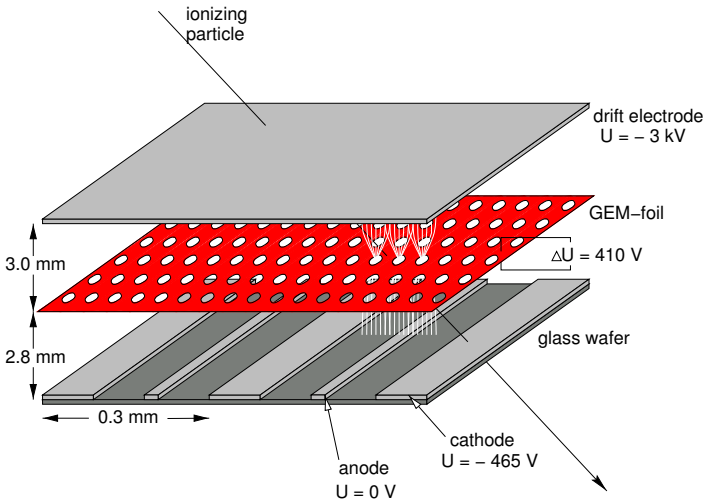

Figure 2.6: Schematic lay-out of the ITR, which consists of Microstrip Gas Chambers (MSGC) together with a gas electron multiplier (GEM).

[2]The angles quoted for directions of wires and strips are with respect to the vertical (y) axis.

2.3.5 The outer tracker

The Outer Tracker (OTR) is of the honeycomb drift tube design and is shown in Fig. 2.7. It is placed perpendicular to the beam axis and covers the region from 25 cm up to 3 m from the beam pipe.

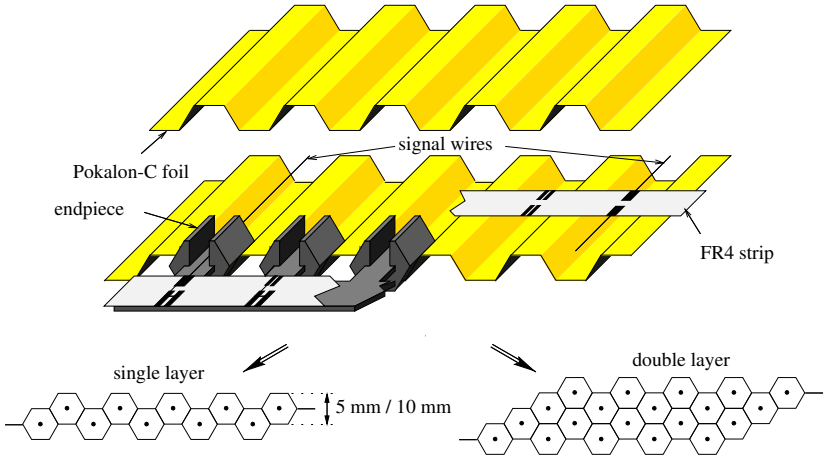

Figure 2.7: Schematic lay-out of the OTR. Honeycomb drift tube chambers of 5 and 10 mm cells size, that can be arranged in a single and double layer system.

The detector is segmented so as to keep the occupancy below 20 %. For reasons of high voltage stability, the cell size can not be smaller than 5 mm. This limits the minimum distance to the proton beam pipe to 20 cm. For distances to the beam pipe larger than 50 cm, a cell size of 10 mm is used, which reduces the number of channels but still keeps the occupancy rate at the desired levels [65]. When a charged particle traverses the chambers it produces free electrons through ionisation in the drift gas; the electrons drift in the highly non-linear electrical field and near the wire form an avalanche of secondary electrons that induces a signal on this anode wire in the center of the tube cell. The time between the crossing of the particle and the arrival of the signal at the anode gives a measure of the radial distance between the wire position and the crossing point of the particle. This allows an improvement of the resolution of the system over the cell size, and final values of about 200 μm have been achieved. The charge collection time must be less than the 96 ns bunch crossing period in order to avoid events from different bunchcrossings mixing together in the read-out procedure. This is achieved also for the large cell size of 10 mm by using a fast drift gas mixture of Ar:CF_4:CO_2. The OTR system is divided into two regions within the detector as shown in Figure 2.8. The first one contains four Pattern Recognition Chambers (PC1, PC2, PC3, PC4) which are located between the magnet and the RICH. They form the core of the track finding; in addition, the stations PC1 and PC4 also provide information to the First Level Trigger (FLT). The second section of the OTR is placed between the RICH and the ECAL systems, and it comprise of the so-called Trigger Chambers (TC1 and TC2). Their main purpose is to provide information to the FLT and allows extrapolation of the tracks to the ECAL and MUON

detectors. Each station contains layers at three different angles (-5, 0 and +5 degrees) with respect to the vertical y axis, which allows a three-dimensional reconstruction of the particle trajectory.

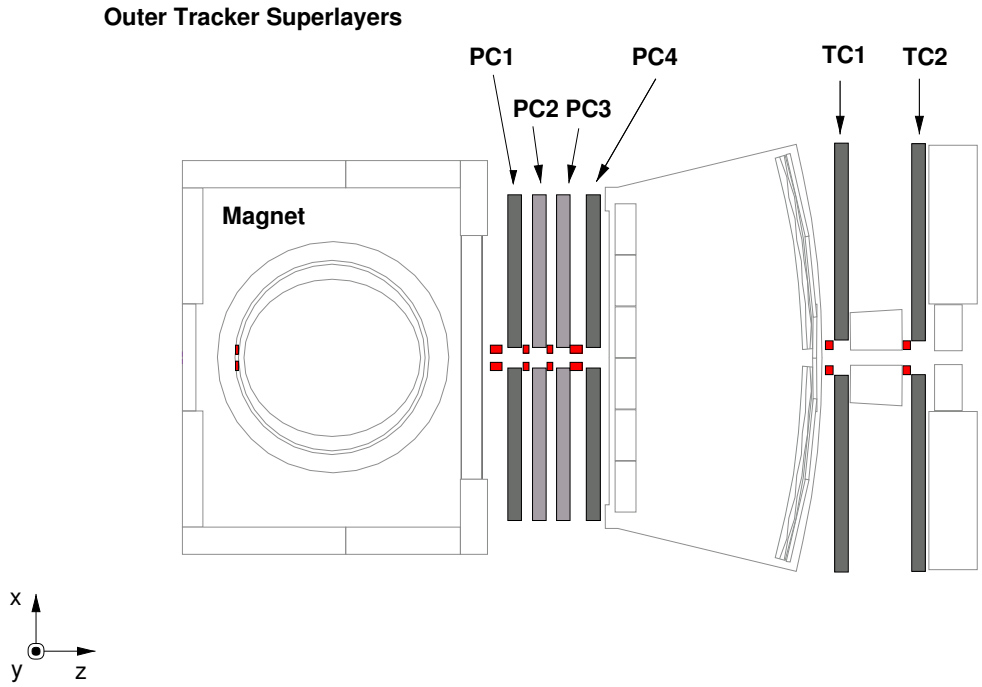

Figure 2.8: OTR tracking stations. The PC chambers are placed between the magnet and the RICH, and the TC chambers between the RICH and the ECAL.

To improve the trigger efficiency the stations used by the FLT have double layers as shown in Table 2.2.

Superlayer	z_{min} [cm]	z_{max} [cm]	Stereo layers
PC1	702.1	730.7	$\circ\ -\ \circ\ \oplus\ \odot\ \ominus$
PC2	742.3	766.4	$\circ\ +\ \circ\ -\ \circ\ +$
PC3	777.9	802.0	$\circ\ +\ \circ\ -\ \circ\ +$
PC4	822.6	851.2	$\circ\ -\ \circ\ \oplus\ \odot\ \ominus$
TC1	1192.2	1211.7	$\oplus\ \odot\ \ominus$
TC2	1305.8	1325.3	$\oplus\ \odot\ \ominus$

Table 2.2: OTR stations. The symbols $+, -$ and $\circ$ stand for +5, 0 and -5 degrees single layers, respectively. The symbols $\oplus, \odot$ and $\ominus$ stand for +5, 0 and -5 degrees double layers, respectively. These chambers are used by the FLT.

During the 2002-2003 data taking period the performance of the OTR was stable, with less than 10 % dead channels, a typical cell efficiency of $\sim$ 95% and a track efficiency of $\sim$ 95 % [66]. For the track reconstruction not all the tracking layers are required to have a hit.

2.3.6 RICH

The main propose of the Ring Imaging Cherenkov Counter (RICH) [67] is to identify charged kaons coming from a B decay. This implies that it has to separate pions from kaons in the momentum range from 3 GeV to 50 GeV [3]. As radiator perfluorobutane gas is used (C_4F_{10}). Charged particles traversing this gas will emit light in a cone with an angle θ_C with respect to the direction of the particle. This angle depends on the refractive index of the radiator gas ($n = 1.00137$) and the velocity β:

$$\cos\theta_C = \frac{1}{n\beta} \ . \tag{2.1}$$

If the momentum of the particle is known from the main tracker information, and θ_C is measured, it is possible to determine the mass of the incident particle. In the gas used here the radiation threshold momenta for pions and kaons are 2.7 GeV and 9.6 GeV, respectively. A spherical mirror projects the parallel photons into a focal point. In order to place the focal surface outside the particle flux, the mirrors are tilted by 9 degrees away from the beam-line. Planar mirrors project the photons to the focal area above and below the radiator vessel, where the sensitive photomultipliers are placed. Figure 2.9 shows a schematic view of the RICH detector and the path of the Cherenkov photons from an incoming particle.

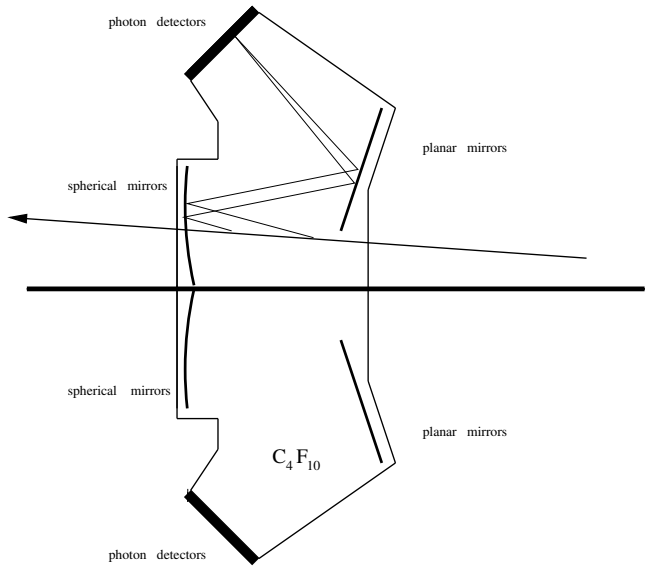

Figure 2.9: Schematic view of the RICH. Rays emitted by a particle and their path to the photon detector are indicated.

Figure 2.10 shows the Cherenkov angle versus the momentum of different particles. A clear separation of kaons from pions and protons is seen in the desired range. The

[3]For simplicity in the notation in this thesis it is assumed $c = 1$. Thus momentum and masses will be also expressed in GeV.

RICH detector was not designed to separate electrons, muons and pions, as can be seen in the figure. Electrons, muons and pions are identified by the response of the ECAL and MUON detectors.

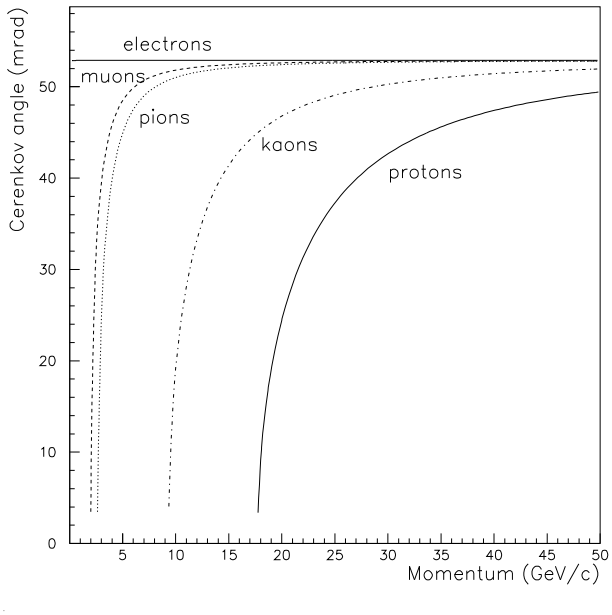

Figure 2.10: Reconstructed Cherenkov angle versus particle momentum. Lines for kaons, pions and protons are clearly separated.

The RICH system was working stably and according to design since the 2000 data taking period.

2.3.7 Electromagnetic calorimeter

The Electromagnetic CALorimeter (ECAL) consists of cells of "shashlik" sampling scintillator absorber with a "sandwich" structure as shown in Figure 2.11. Absorber material (Pb and W) ensures that the incident electrons and photons deposit all their energy in the ECAL. The primary electrons or photons traversing cells material produce secondary radiation by Bremsstrahlung and pair production. This creates a short, narrow shower of electrons-positrons, that produce scintillation light when they traverse the scintillator material. This light is read out by plastic WaveLength Shifter (WLS) fibres running perpendicular to the plates and connected at their end to photomultipliers. To discriminate between hadrons and electrons, the characteristic of the electromagnetic shower is used.

This lead to an energy deposit which for electrons is equal to the total energy or momentum of the particle. Hadrons do not deposit their full energy in the a calorimeter as they produce hadronic showers which penetrate more deeply and exit the rear of the calorimeter. Thus, candidates with a ratio of ECAL energy over momentum (E/P) close to unity are considered electrons or positrons. Photons are identified as ECAL clusters with no associated track. As in the case of the OTR, the radial dependence of the track density suggests a variable cell size so as to equalise the occupancy. Thus, the system is divided in three sections (inner, middle and outer) with cell sizes of 2.23 × 2.23 cm^2, 5.757 × 5.757 cm^2 and 11.15 × 11.15 cm^2, respectively. The ECAL system was working correctly during the 2002-2003 run, with energy resolutions $\sigma(\mathrm{E})/\mathrm{E} = \mathrm{A} / \sqrt{E(GeV)} + \mathrm{B}$ summarised in Table 2.3 [68].

	Inner	Middle	Outer
A	0.205 ± 0.002	0.118 ± 0.001	0.108 ± 0.002
B	<0.02	<0.02	<0.02

Table 2.3: Energy resolution parameters A and B for the energy resolution, $\sigma(E)/E = \mathrm{A} / \sqrt{E(GeV)} + \mathrm{B}$. Values in this table are still preliminary.

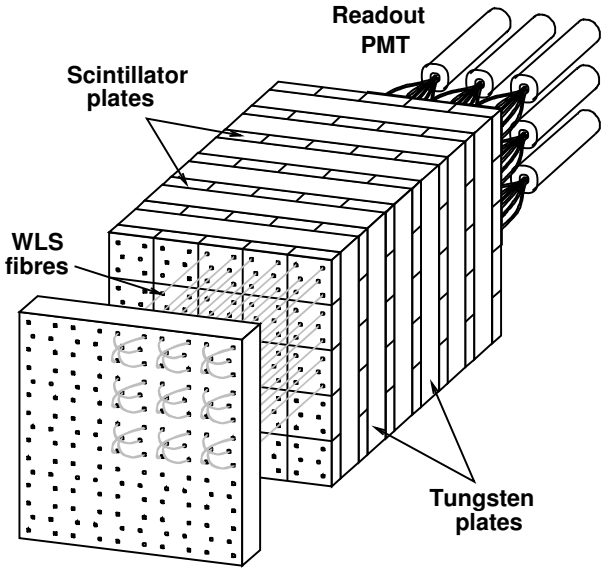

Figure 2.11: ECAL cell. Layers of absorber material are placed between scintillator plates. The signal is guided to the photomultipliers (PMTs) by WaveLength Shifter (WLS) fibres.

2.3.8 Muon system

The main purpose of the muon system (MUON) is to provide pretrigger information to the trigger and to identify muons, separating them from hadrons. It consists of concrete and steal absorbers between four superlayers of pad and wire chambers (MU1, MU2, MU3 and MU4) as shown in Figure 2.12. The absorbers stop hadrons, so that most particles

reaching the rear of the muon detectors are in first instance considered to be muons; however, decay in flight of pions and kaons leads to muons which do not originate for the primary vertex. Due to the thickness of the absorber material, the muons must have a momentum higher than 4.5 GeV to leave hits in all the chambers. The inner region of the system at the high occupancy area, close to the beam pipe, is made out of gas pixel chambers of 9×9 mm^2 cell size and 30 mm wire length, oriented along the z direction. The first two superlayers (MU1 and MU2) consist, in the outer part, of three layers of muon tube chambers at three different angels (-20, 0 and 20 degrees) and a cell size of 12 mm. They are used to provide track matching with the OTR. The layer MU1 also provides information to the FLT. The last two superlayers behind the absorbers (MU3 and MU4) consist of vertical double layer tube chambers with a segmented cathode (pads) which is also readout. The pads have an approximate cell size of 12×13 cm^2. These last superlayers are placed with no absorber in between so as to provide clean information about position and direction. The muon performance (as summarised in [69]) showed an average pad efficiency of 92 % and for tube chambers a 99 % double hit efficiency.

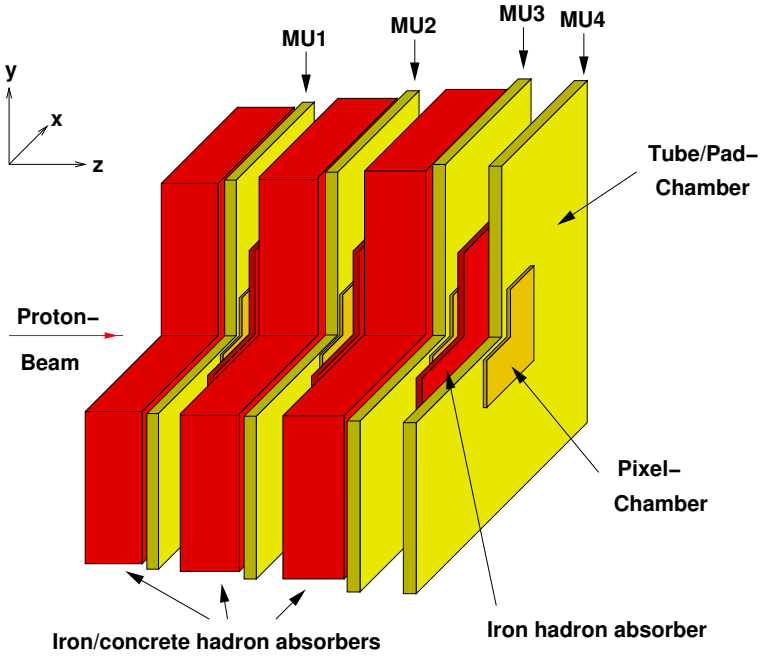

Figure 2.12: MUON schematic view. It consists of hadron absorbers between four superlayers. The inner region is composed of pixel chambers and the outer part of tube and pad chambers as described in the text.

2.3.9 Trigger system

The trigger system of HERA – B is built to filter only the few interesting events out of the huge rate of primary interactions. The primary interaction rate was planned to be about 40 MHz, whereas the rate of the original interesting $B^0 \to J/\psi\, K^0_S$ events is many orders below this. The trigger is a multilayer system, starting from pretrigger information

from the ECAL and MUON system, followed by a hardware tracking system to perform a fast lepton selection. The higher level software trigger refines the track parameters and performs a dilepton selection. The originally designed scheme differs from that which was used during the data taking period 2002/2003, and we describe it here only as it was used during this period. This mode has been dubbed "star mode" and accepts events with at least 2 pretrigger messages form the ECAL or MUON, at least one track reconstructed by the first level trigger, and a dilepton vertex reconstructed at the Second Level Trigger (SLT).

The pretrigger seeds for the trigger tracks are obtained from the ECAL and the MUON system. A pretrigger seed will be issued by the ECAL when a cluster of five cells in a cross shape, with energy above 1 GeV is found. For a muon seed a hit coincidence between the last two muon stations (pad chambers MU3 and MU4) is required.

The first level trigger is a hardware trigger composed of dedicated boards which make a fast decision on reconstructed tracks. The information of the pretriggers and of the tracking stations is transmitted through the Trigger Link Boards (TLBs) to the Track Finding Units (TFUs). These try to find tracks via a Kalman filter technique [70]. A detailed description of the FLT is done in Chapter 4.

The second level trigger is based on software and redoes the tracking based on the pretrigger seeds. It runs on a farm of PCs where each one process a particular event so that several events are processed in parallel. It also includes hit information from PC2 and PC3 and uses the drift time to refine the track parameters. To improve the momentum determination a VDS reconstruction of the track is also performed. The SLT will accept an event when at least 2 tracks are compatible with a common vertex.

Finally, a Fourth [4] Level Trigger (4LT) runs simultaneously. Its task during the 2002-2003 data taking period was to reconstruct, monitor and classify subsamples of the events. Figure 2.13 shows an schematic view of the trigger chain, together with the rate reduction at each step.

2.3.10 Data acquisition

The Data Acquisition System (DAQ) is shown schematically in Figure 2.14. HERA – B represents about 600,000 channels to be inspected and possibly read out by the system for each interaction. In a first step data from up to 128 bunch crossing are stored in the front end electronics while the FLT makes the trigger decision. The FLT receives direct hit information from the pretriggers and the tracking stations by a system of linkboards. The trigger decision is passed to the Fast Control System (FCS), which synchronises the different subsystems. On a positive trigger decision the FCS distributes the signal to the Front End Drivers (FEDs) to transmit the event information via the switch to the Second

[4] A third level trigger was foreseen but finally not implemented. The nomenclature was kept so that in our scheme we pass from the second level trigger to the fourth level trigger.

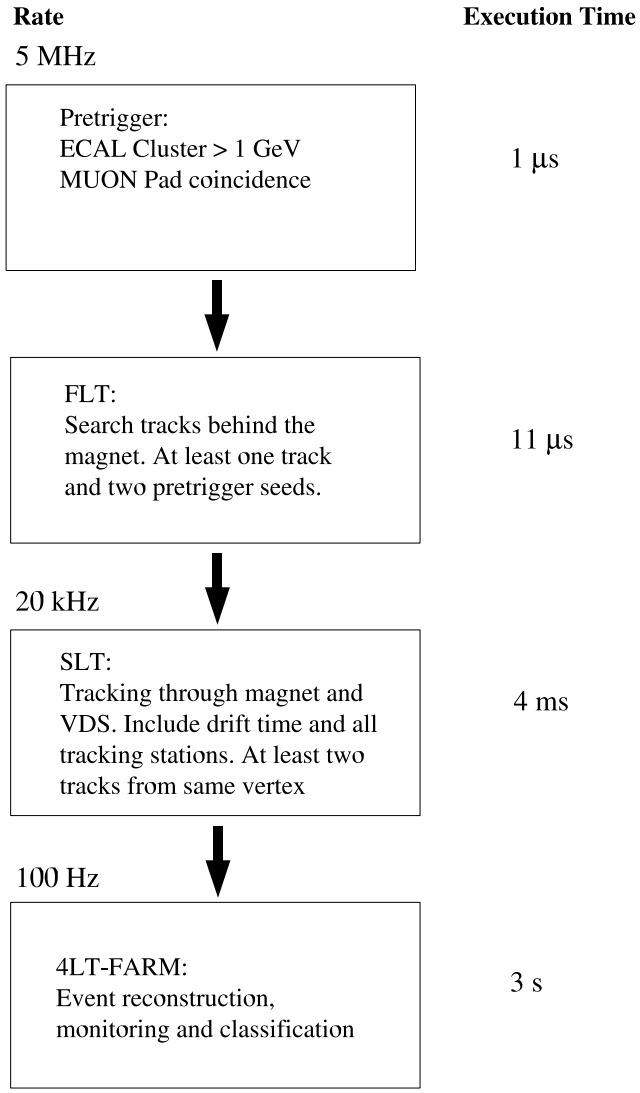

Figure 2.13: Trigger chain. Execution time and reduction rates are shown explicitly.

Level Buffer (SLB) [5]. The SLB will provide the input information to the SLT and also store it until the SLT makes a decision. If the event is accepted by the SLT, the complete data information is transmitted via the switch to a particular SLT node (processor) to a possible third level trigger evaluation. After this, the event is passed to the fourth level trigger which operates on a second farm of about 200 PCs, where the event is completely reconstructed and stored on tape.

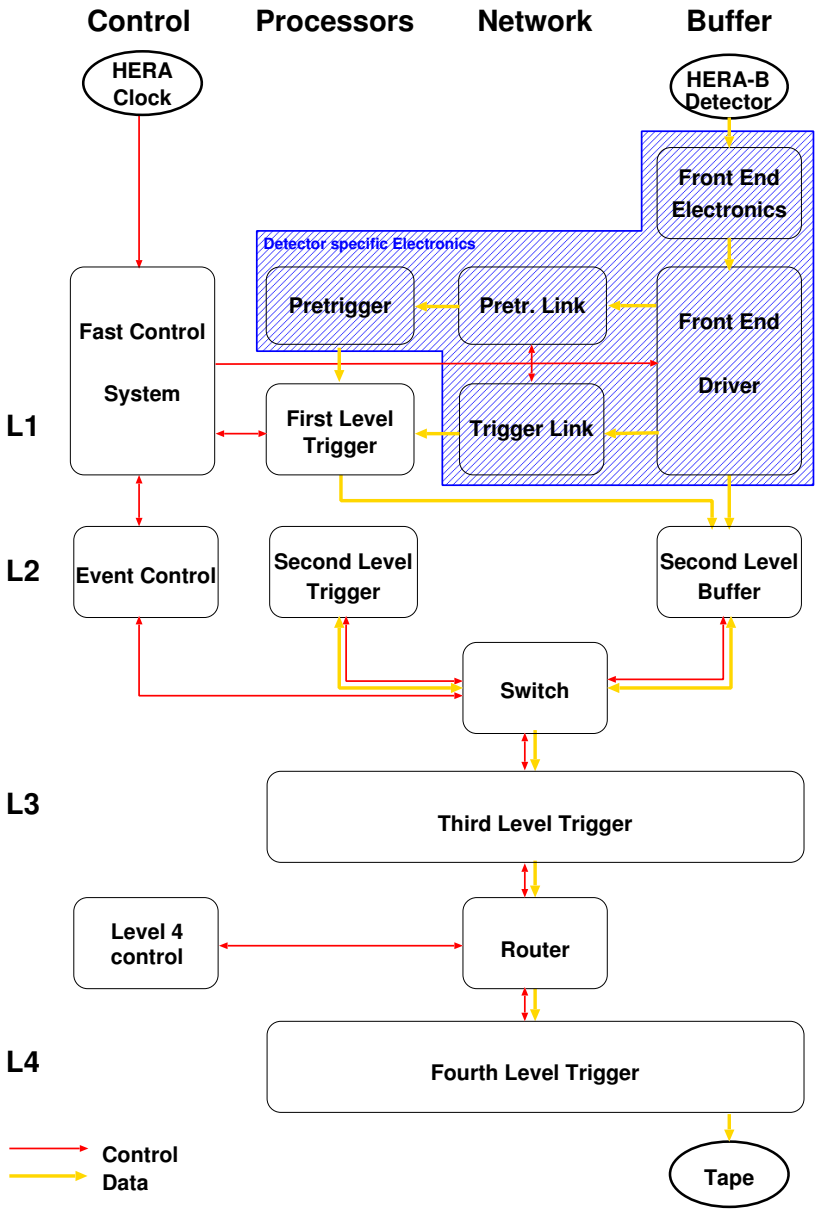

Figure 2.14: Architecture scheme of the Data Acquisition System (DAQ) as described in the text. Shadow area shows the detector specific electronics.

[5]The switch consist of a set of boards which route data between the SLT nodes and the SLBs.

Chapter 3

Data Samples

In this chapter we introduce the data samples (data and simulation) used in the present studies.

3.1 Data

The data used in this analysis were taken between October 2002 and February 2003. The sample can be divided in several periods between access days, during which work on commissioning took place. This work produced new alignments and efficiencies of the different detector components.

A total sample of 150 million triggered events were taken with the trigger in the "star mode" which requires at least two pretriggers, at least one FLT track and at least two SLT tracks from a common vertex. These trigger data lead to a sample of 300,000 off-line reconstructed J/ψ almost equally distributed in the muon and electron decay channels. A sample of 180 million minimum bias events was also collected with a trigger that requires a minimum occupancy in the detector, meaning at least 30 photons in the RICH or a total energy in the ECAL greater than 1 GeV. In stable and normal conditions, HERA – B was taking data at 5 MHz interaction rate, with an output of ~ 1200 J/ψ per hour on tape for dilepton triggered events. Eleven different wire configurations were used, including Carbon, Tungsten and Titanium materials as target wires. A maximum of two wires were used simultaneously. Figure 3.1 shows the accumulated number of triggered and minimum bias data versus time.

Table 3.1 shows the amount of dilepton data collected with the different wire configurations, together with the number of runs in each one. This shows clearly the fragmentation of the data sample. The biggest sub-sample was taken using carbon targets (≈ 64 %), followed by tungsten (≈ 27 %) and titanium samples (≈ 9 %).

The total amount of data taken was only 10 % of what was promised. After a major

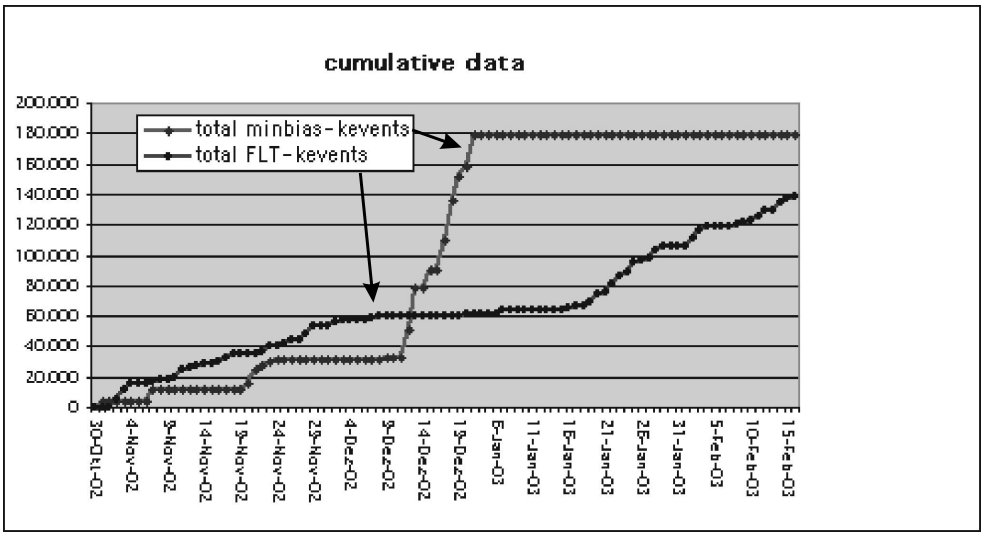

Figure 3.1: Cumulative data samples acquired (as of 15th of February 2003). Minimum bias and trigger data were taken separately, the biggest sample of minimum bias was taken in a dedicated period in December 2002.

Target Setting	Wire Material	# Runs	# dileptons
B1	C	61	12,516,211
B1B2	C/Ti	25	13,679,215
B1I1	C/W	44	23,009,704
B1I2	C/C	24	11,524,843
B1O2	C/W	70	41,879,965
B2	Ti	17	6,867,597
B2I2	Ti/C	7	61,663
I1	W	9	177,792
I1I2	W/C	51	17,461,433
I2	C	81	22,388,948
O2	W	11	6,841,770
total		385	156,409,141

Table 3.1: Statistics of the dilepton triggered data on the different wire configurations.

shut down to upgrade the luminosity at the collider experiments at HERA (ZEUS and H1) in the year 2001, a new period of data taking started in 2002. Major problems appeared at the start up, due to unacceptable levels of radiation at the collider experiments. This radiation was mainly due to misplacement of new collimators and to vacuum problems. Under these conditions the DESY management had to put priority to get HERA running at the design values, which entailed a premature stop of HERA – B . Fig 3.2 shows the data taking status of the HERA – B detector in time percentage.

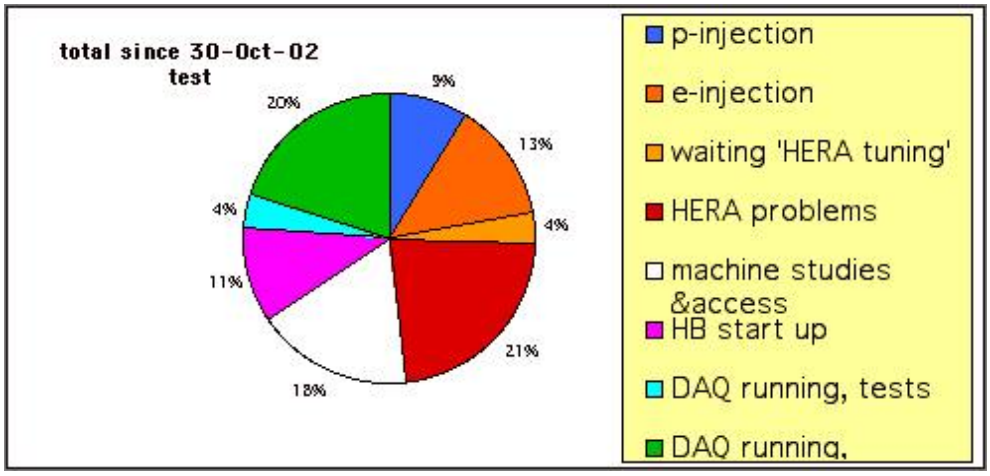

Figure 3.2: Status of the data taking in time percentage distribution at Desy.

Runs used in this analysis are physics runs with the trigger in the star mode and with reasonable statistics. Several runs are discarded due to:

- Test runs with unstable trigger conditions;
- Runs with non standard trigger settings;
- Trigger efficiency runs;
- Runs with broken wires;
- Runs during which important devices were missing or malfunctioning;
- Runs with unstable or unusual vertex distributions;
- Runs with too low or too high interaction rates.

These requirements selected 327 runs to be used in this analysis. During data taking it happened twice that due to sudden miss-positioning of the proton beam, the O2 Tungsten wire was hit directly by the proton beam. This over exposure broke the wire forcing a replacement.

3.2 Monte Carlo Simulation

The simulation of triggered heavy quark data in the HERA – B frame is done using two different MC packages [71]. One is the PYTHIA package [72] used to simulate the hard partonic interaction leading to the heavy quark production. Since PYTHIA is not able to reproduce nuclear effects and soft interactions, for these effects the FRITIOF package [73] is used. The mechanism to simulate the complete process starts with PYTHIA generating the process $pN \rightarrow q\bar{q}X$, which includes the hadronisation of the quark pair through the JETSET package [72]. The remaining energy carried by X is then given to FRITIOF in order to simulate the accompanying soft processes of the interaction. After this, all final state particles are passed to the GEANT 3 package [74] to simulate the response of the HERA – B detector to these particles. The number of interactions per triggered event corresponds to one hard process (triggering interaction) plus minimum bias interactions following a Poisson distribution with a mean value of half an interaction per event [1] [75]. For double wire runs, the hard interaction is forced to be in one of the wires and the minimum bias process is shared by the two active wires.

The acceptance of the detector depends on x_F and p_T. These distributions must therefore be reproduced correctly by the simulations. Since the MC simulation only includes calculations to a limited order in perturbation theory, and since the interactions within nuclear matter are not well understood theoretically, these distributions are not properly generated by the packages PYTHIA and FRITIOF. To overcome this problem, the prompt J/ψ events are weighted such that the distributions of the E789 collaboration are reproduced. However, this specific experiment has a positive x_F range acceptance only, and nothing is known about the behaviour at negative x_F. We have assumed a distribution symmetric in x_F. In the case of J/ψ from b decays, there is no experimental information available concerning the corresponding distributions, in this case the events are re-weighted according to the NLO-NNLL (Next to Leading Order - Next to Next to Leading Logarithm) theoretical calculations of Mangano *et al.*[3, 4], with a b quark mass of 4.75 GeV and a QCD renormalisation scale $\mu = \sqrt{m_b^2 + p_T^2}$. The HERA – B MC takes into account the hadronisation of the heavy quarks by coupling them with the spectator partons in the colliding nucleons. We make use of b fragmentation function, by a Peterson shape [27] and with a parameter $\epsilon = 0.006$ [76, 77, 78] in order to obtain the correct distributions of the final hadron states. Finally the intrinsic transverse momenta of the incoming partons are smeared to fit a Gaussian distribution with average squared transverse momentum $< k_T^2 > = 0.5$ GeV^2 [79]. Figure 3.3 [80] shows the comparison of the x_F and p_T distributions with and without the weighting factor. From these distributions we estimate the fractions of $b \rightarrow J/\psi$ and prompt J/ψ, within the HERA – B acceptance, to be $f_B = (90.6 \pm 0.5)$ % and $f_p = (77 \pm 1)$ %, respectively.

The MC samples are grouped in different periods (in a month base) with similar detector characteristics and configurations. This includes efficiencies of each detector com-

[1] At an interaction rate of 5 MHz there is half an interaction per bunch crossing at 10 MHz HERA bunch crossing rate.

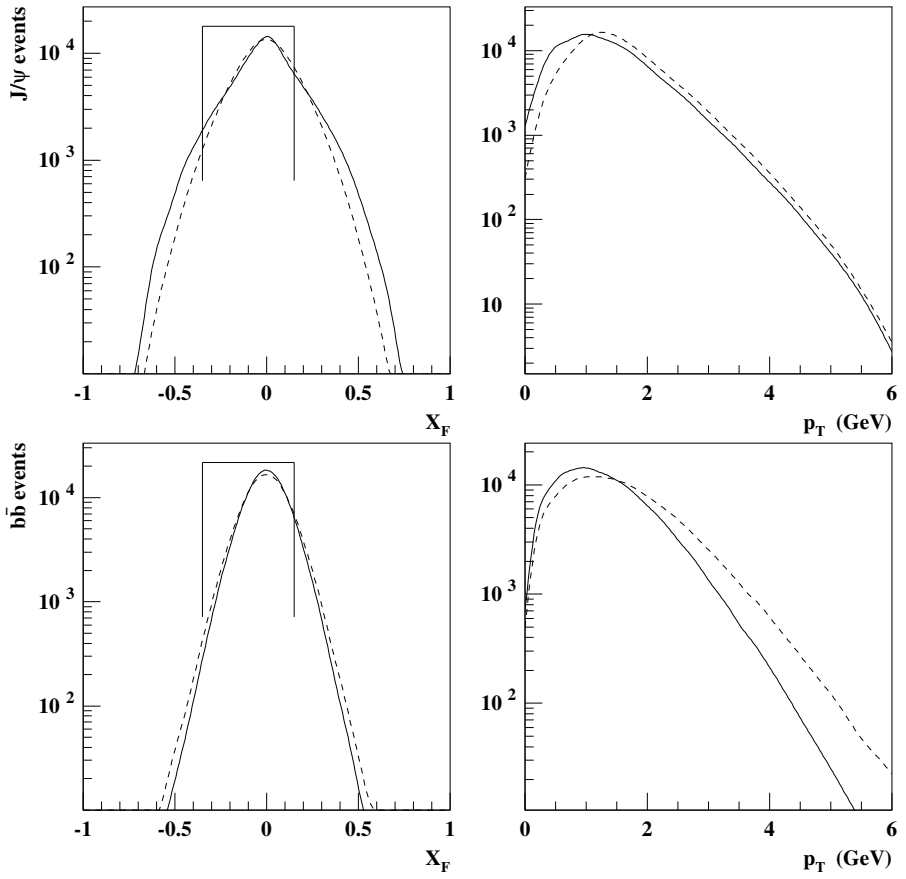

Figure 3.3: x_F (left) and p_T (right) distributions for prompt J/ψ (top) and for J/ψ from b decays (bottom). Solid lines show the MC model we use; the dashed lines show the PYTHIA default distributions. The HERA – B x_F acceptance is shown explicitly.

ponent, dead channels, detector alignment, trigger efficiencies, etc. In double wire configurations, two different samples were generated, each one containing the physics process generated on one of the two wires with the minimum bias events distributed equally on both wires. On average, for each wire in each wire configuration about two million events are generated for the prompt J/ψ proccess, and 500,000 for the $b \to J/\psi$ events.

3.3 Event reconstruction chain

The event reconstruction is done with the ARTE software packages [81]. It contains tools for hit preparation, stand alone track reconstruction on different detectors and particle identification. The process starts with the hit reconstruction form the raw data at each detector component. The next step is the track finding base on the hit information. In the

VDS, track segments are reconstructed by a Cellular Automaton for Tracking in Silicon (CATS) package [82]. A similar cellular automaton is used to reconstruct tracks in the pattern recognition chambers [83] while a second package (RANGER [84]) propagates tracks to the trigger chambers. For particle identification a stand alone tool runs on the ECAL, the CARE packages [85], which looks for cluster of cells with energy deposit. Muon identification is done by matching tracks in the tracking chambers with hits in the MUON chambers [86]. The RITER package [87] is use to assign Cherenkov rings to tracks traversing the RICH detector. Finally segments in the VDS and in the subdetectors behind the magnet are matched into long tracks by the MARPLE package [88]. For these long tracks with hits before and after the magnet, their momentum is estimated from their deflection in the magnetic field. As the last step, the track parameters are refined by a refit with all available information. After the track finding, the GROVER package [89] is invoked for vertex reconstruction.

3.3.1 Track finding and vertexing

Tracking and vertexing at HERA – B are based on the Kalman filter technique. The Kalman filter determines the evolution of a system, described with a state vector, with the addition of individual new measurements. It is an iterative method that consist essentially of three steps which can be summarised as [70]:

- Prediction: From the known parameters at the current step, the coordinates of the search window in the next step are estimated.
- Filter: The contribution of the new measurement to the total χ^2 is evaluated. A decision whether the new measurement is included or not depends on this contribution.
- Smoother: Recalculates the state vector with the information of all measurements and propagates the information backwards, making the full information available at each step.

As a tracking method [84], the Kalman filter starts at the "rear" end of detector with an initial estimate of the track parameters and uncertainties and proceeds sequentially through the detector stations. At each step the track parameters are updated with the new hit information. Based on this information it predicts the location of the hits in the next station. The process continues until no navigation options are available, *e. g.* at the end of the spectrometer or after successive failures to find hits in the predicted regions. This method yields a pattern recognition efficiency of ~ 96 % with a ~ 10 % ghost rate [84] in a dense environment with an average of ~ 140 tracks per event.

For vertexing, a new measurement corresponds to the addition of a reconstructed track [90]. At each step a new track is added to the vertex and the vertex parameter are updated accordingly. The algorithm starts taking as reference the target-wire position.

These method showed a reconstruction efficiency for a single vertex of 97 % with a ghost rate at the level 1-2 % [91].

Chapter 4

First Level Trigger

The primary aim of the FLT is to provide a fast trigger decision for J/ψ events based on the selection of lepton pairs from a common vertex in a certain range around the J/ψ mass. However, in order to increase the efficiency during the 2002-2003 run, it was changed to provide a trigger signal if at least two trigger seeds of either the ECAL or the MUON system were received, and in addition at least one lepton track was reconstructed. The rate reduction - in combination with the additional second level trigger requirements - was sufficient to reach the required reduction rate from 5 MHz to 20 kHz. Note also, that the trigger chain was not set at its full planned capability, since the high p_T trigger as well as the inner detectors were not included, due to late commissioning and instability of their performance.

In this chapter we first give an overview of the principle of operation and the hardware implementation of the First Level Trigger. After this, we present an analysis of its performance during the data taking period 2002-2003.

4.1 Overview

The FLT consists of 60 hardware processors for track reconstruction working with a 50 MHz clock. It has to make a decision within 128 bunch crossing (12 μs). It receives hits inputs from tracking chambers (every bunch crossing 100k bits) and messages from pretriggers. The hits of the last 128 bunch crossing (BX) are stored in Wire Memories (WMs), custom built ASIC [1] chips with a 128 bunch crossing pipeline. The processors communicate with each other via an 80-bit message carrying the track parameters. The FLT messages travel asynchronously through the network. Track finding is based on triple hit coincidences of the three wire views in each superlayer, within a certain region of interest (RoI). All boards are 9U VME boards equipped with Motorola 68020 CPUs allowing monitoring and debugging. The hardware is based on a one-to-one mapping of

[1] Application-Specific Integrated Circuit

the region within tracking chambers on a processor (Track Finding Unit - TFU) in the trigger hardware. The schematic of the system can be seen in Figure 4.1 which shows the connection between the detector and the TFUs and between the TFUs themselves. Each processor has access to hit information in a certain region defined by the overlap of wires of each of the three views in a particular chamber. As input a processor receives track information from a downstream processor, which has determined that the region of interest defined by a track is within the wire chamber region covered. Using the hit information from the wire memories, the track parameters are updated and the region of interest is defined in the next upstream trigger chamber, which again corresponds to a processor linked to this region via a wire mapping. The track information is then passed to the processor where it is updated. This continues until all wire planes have been traversed by the track. All tracks found in this way in parallel are then passed to the Track Parameter Units (TPUs). Each TPU determines the momentum of the particle assuming that it was generated at a reference target position. It makes a selection of the tracks based on their transverse momentum and total momentum. For electrons, it makes also a selection based on the ratio of ECAL energy over momentum. The tracks are also scanned for multiple copies of the same track. After removal of these clones the list of remaining tracks are passed to the Track Decision Unit (TDU) where the final track based trigger decision is made. In this unit also two track invariant masses can be calculated in order to aid the trigger decision.

To start the process the pretrigger information from the ECAL and MUON system are used. From these reference positions the FLT starts the backward tracking search towards the target. It uses the Kalman filter technique [70] to update the track information at each step. The chambers used in the FLT are the MU4, MU3, MU1, TC2, TC1, PC4 and PC1 chambers (see Figures 2.8 and 2.12). From the pretrigger seed the filter defines a Region of Interest (RoI) in the closest layer towards the target. In Figure 4.2 the process can be seen schematically, starting from the leptonic pretriggers going in the direction of the target. The shadowed areas indicate the RoI search at each step of the tracking filter.

Then track information is propagated coded in a message of 80 bits. The propagated message contains the RoI, the destination TFUs and the actual track parameters. This process allows a fast transmission of the information, since it reduces the amount of data transmitted at each step substantially, transmitting only a few track parameters and not the full hit information. This technique is based on the premise known as “move the process and not the data”.

4.1.1 Pretriggers

The pretriggers define either an electron or a muon candidate. Muon pretriggers are defined by the muon system. The only particles that can traverse the muon absorbers and yield a signal are muons, thus, a hit pattern in the last two stations is sufficient to identify a muon candidate with high probability. The pretrigger algorithm searches for hit coincidences in the pad chambers MU3 and MU4. Figure 4.3 shows the coincidence

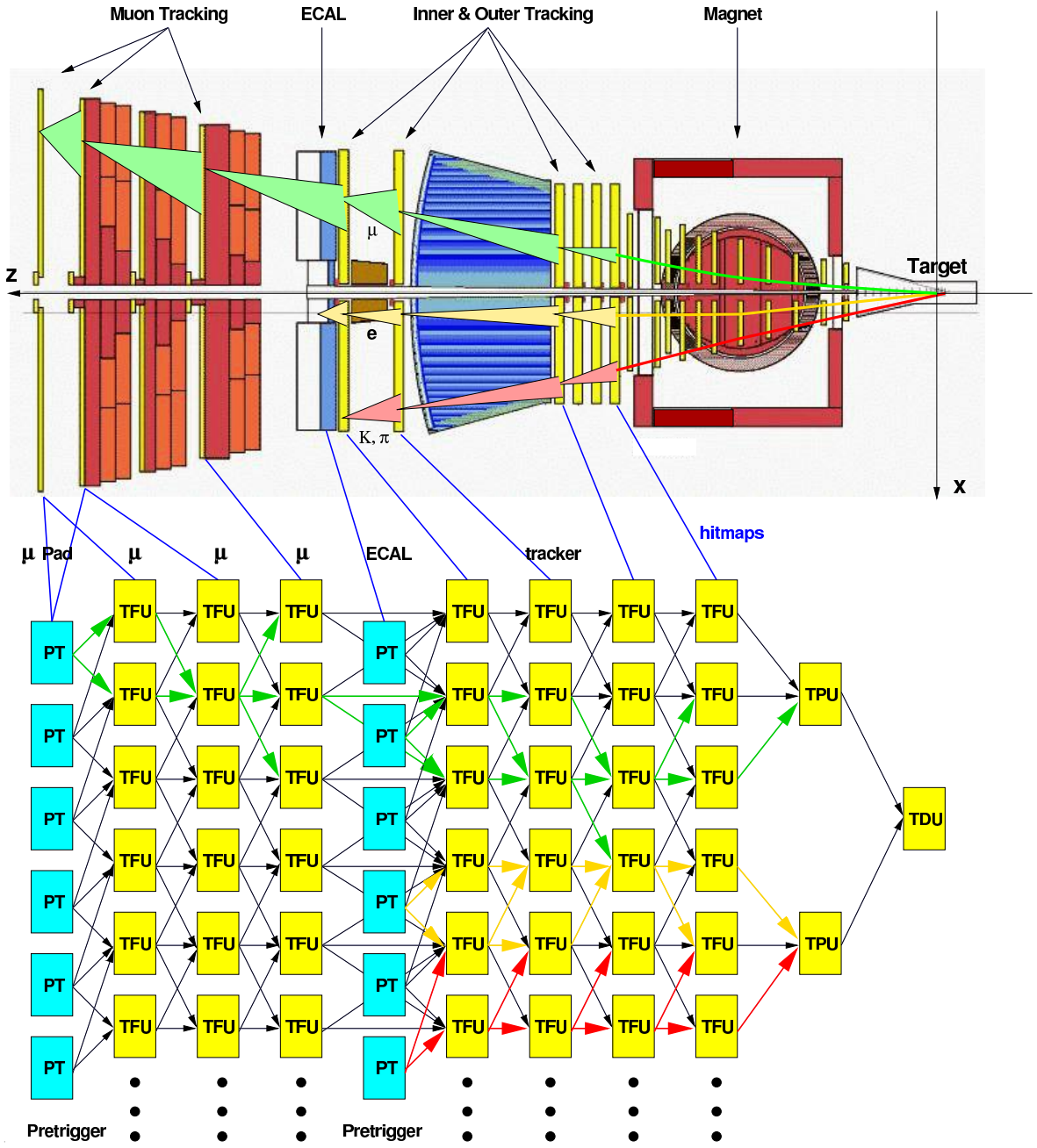

Figure 4.1: Layout of TFU boards performing the track finding at the FLT. Hit information is transferred from the pretriggers and the tracking system to the TFUs. The TFUs perform the track finding through a Kalman filter technique from left to right in the figure. The final tracks found by the TFUs system are then passed to a Track Parameter Unit (TPU) where a track selection is performed. Finally, a Track Decision Unit (TDU) does the last selection of the event and issues the trigger decision.

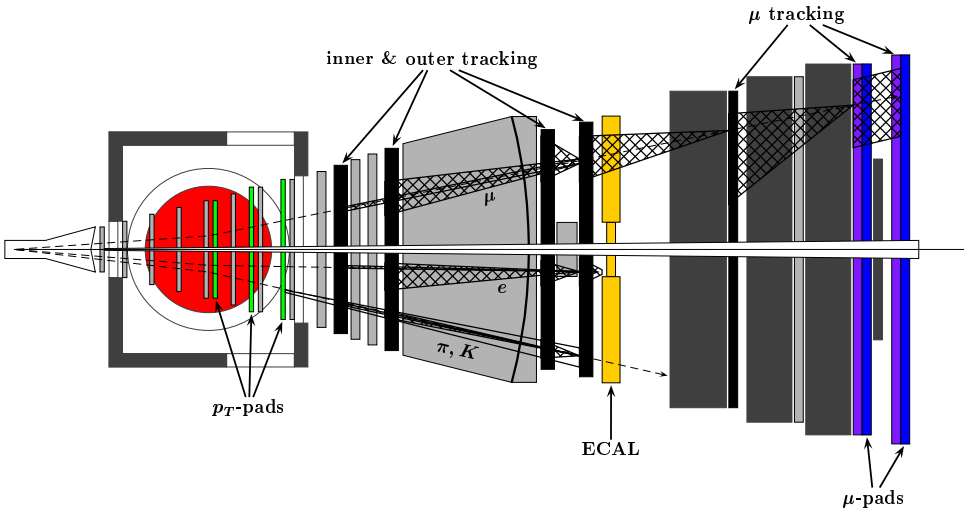

Figure 4.2: Schematic track finding procedure. From right to left, the different steps of the Kalman filter algorithm are shown. The shadows correspond to the region of interest from layer to layer. At each step, the track information is updated. The pretrigger regions are indicated (note that the p_T trigger was not used in the run 2002-2003).

pattern. Since the muons traversing the absorbers suffer from multiple scattering, they present a significant angular spread, which is taken into account by a six to one coincidence scheme. When a coincidence is found, a message is transmitted to the FLT network.

The electron pretrigger is based on the ECAL information. Dedicated pretrigger boards perform a search for a local energy maximum in the ECAL cells. To these cells, the energy of the adjacent cells is added, forming a cluster with a cross shape with a total of 5 cells as shown in Figure 4.3. A pretrigger message is issued if the following requirements are fulfilled:

$$E_{Centercell} > E_{TH}/2 \tag{4.1}$$

$$E_{Total} > E_{TH} \ , \tag{4.2}$$

where E_{TH} is an (adjustable) threshold. E_{TH} is related to the cut on the transverse energy (E_T) by:

$$E_{TH} = E_T \frac{\sqrt{x^2+y^2+z^2}}{\sqrt{x^2+y^2}} \ . \tag{4.3}$$

This relation is based on a simple E_T determination assuming no bending in the magnet. In 2002-2003, E_T was set to 1 GeV. The x and y positions of the cluster are determined

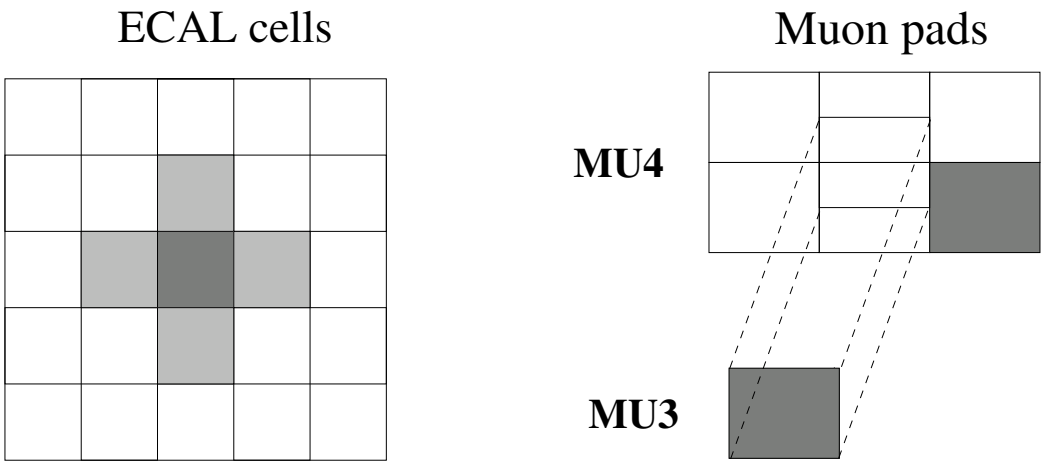

Figure 4.3: Pretrigger seeds from ECAL and MUON systems. Left: ECAL cluster with a cross shape formed around a locally maximum energetic cell. Right: Coincidence scheme for the muon pretrigger based on the pad chambers MU4 and MU3. The dashed lines show the projection of MU3 onto MU4, whereas the shadowed regions indicate one of the possible coincidence patterns.

from the center of gravity. When a cluster passing the above threshold cut is found, a message is passed to the tracking hardware.

4.1.2 Data transmission from the tracking system

Each wire of the OTR honeycomb cells is connected via a 20 cm coaxial cable to an ASD8 (8 channel Amplifier-Shaper-Discriminator) chip which treats 8 wires. The ASD8 chip amplifies, shapes and discriminates the signal and sends a differential signal to a Time to Digital Converter (TDC) via twisted pair cables of about 5 m length. The TDC determines the drift time and codes it into an 8 bit format. Each TDC reads up to 32 wires and stores up to 128 consecutive events. The depth of this buffer corresponds to about 12 μs and defines the accepted latency of the FLT. The hit patterns, without the drift time are sent to the Trigger Link Boards (TLBs) which map them and send them to the wire memories of the FLT system. The TDC also performs a logical OR between double layers cells in order to increase the efficiency. If the FLT only receives hit patterns from single layers the track efficiency will be determined by the efficiency of finding a hit in all 12 wire layers that cover the FLT in the OTR. Assuming a hit efficiency of 98% we have for the maximum probability that the FLT finds the track:

$$\epsilon_{FLT\ track} = \epsilon^{12}_{OTR\ hit} = 78.5\% \ , \tag{4.4}$$

whereas in the case of an "OR" of each double layer, this efficiency becomes:

$$\epsilon_{FLTtrack} = (\ 1 - (1 - \epsilon_{OTR\ hit})^2\ )^{12} = 99.5\%. \tag{4.5}$$

After a positive FLT decision, the TDC transfers the hit information to the Second Level Buffer (SLB, SHARC[2] boards) which is read by the SLT. The complete scheme of the data transmission can be seen in Figure 4.4. For the MUON chambers the read out system is similar to the OTR but without the TDC step, since no drift time is determined.

4.1.3 Trigger Link Boards

The data from the Front End Drivers (FED) is transmitted to the TFUs through specific trigger link boards [92]. The TLBs receive the information from the TDCs through flat cables. Since the FLT operates independently of the HERA – B bunch crossing (BX), the BX identification must also be distributed with each event which is done by the Fast Control System (FCS). The flat cables contain 34 leads (32 signal and 2 grounds). In the case of the OTR, each pin carries the signal of ORed cells. These 32 signals are fed to a Programmable Logic Device (PLD) which is programmed for mapping the geometry of the OTR to the one used by the FLT. In addition the BX number of the hits is added to the data stream sent to the TFU. Figure 4.4 shows the position of the TLB in the data transmission chain. The mapping is needed because the data from the detector can not be transmitted directly to the TFUs, but it must be organised to adjust to the simplified pattern used by the TFUs calculations. Because of the requirement of a fast calculation, the FLT needs to assume that cells represented by the wire memory (WM) locations are equidistant. This is not the case where a TFU covers regions of both 10 mm and 5 mm OTR cells; in these cases the signal must be split or merged [93] in a way such that the equal spacing can still be assumed. This procedure is shown schematically in Figure 4.5. Some TFUs cover the region where the OTR is separated into two halves. If the closing between the two halves of the station is not perfect, this may introduce a gap on the spacing of the cells of different halves. Since this disturbs the equidistancy between WMs an additional hit is inserted (hardcoded 1 in the hit pattern) to fill the gap if needed. In order to increase the efficiency, the PLDs also makes a logical OR of consecutive cells of the +5 degree layers of each station. This is done by distributing the cell signal into the corresponding bit of the WM and into the previous one.

After the mapping is done the PLD distributes a 24 bit signal to a Motorola AUTOBAHN chip, which performs the serialisation of the information. The AUTOBAHN chip creates and distributes two 32 bit packages during one bunch crossing. Each package contains 24 bits for hit information and 8 bits for the bunch crossing identification. The BX identification is also used to check transmission errors, since it is known that it must be identical for two consecutive packages and must increment in the next package. The packages are transmitted by ≈ 50 m long optical links to an optical receiver at the TFUs

[2]Super Harvard ARchitecture Computer

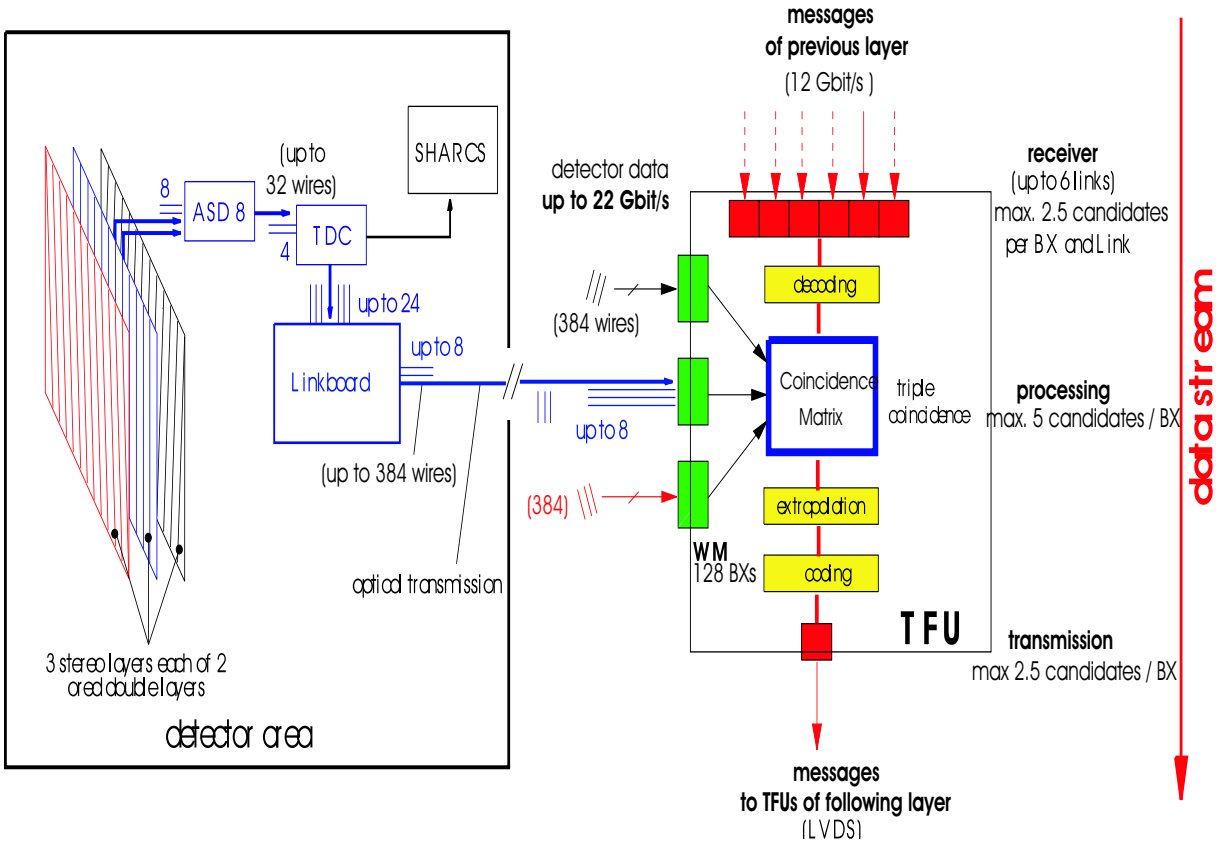

Figure 4.4: Schematic view of the data transmission. From left to right, an OTR wire signal is processed by an ASD8 channel, which amplifies, shapes and discriminates the signal. Then a TDC digitises the signal and sends it to the TLB. After mapping the hit information a serialised signal is sent via optical links to the TFUs. The TFUs receive also the message from the (logically) previous TFUs and, if a triple coincidence is found, will update and propagate the message to the next station.

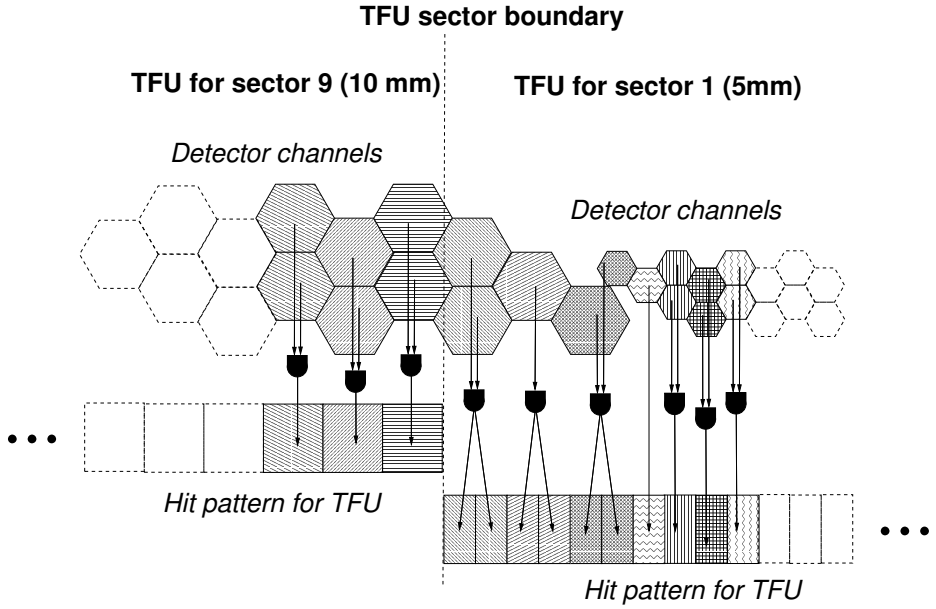

Figure 4.5: Schematic view of the mapping of the detector cells in the WMs. The dotted line indicates the separation between two TFUs. The one at the right is covering a region with both cell sizes. In this case the 10mm cells are splitted into two WM cells to accommodate with the assumption of the equal spacing between the WMs. The logic OR at the TDC is explicitly shown.

where another AUTOBAHN takes over the serial signal and distributes it finally to the WMs.

4.1.4 Track Finding Units

The TFUs are the core of the FLT system. They are dedicated boards which can be schematically seen in Figure 4.4. There are three WMs on each TFU, covering the hit map of each of the three stereo views of the corresponding superlayer. The WMs are dual-ported, which allows them be written to and read out simultaneously. They store 128 events. A Coincidence Matrix (CM) performs a search for hit coincidences in the three WMs in the corresponding RoI. If a coincidence is found, its position will be determined from the location in memory and this hit is added to the track and the parameters of the track are updated. The new parameters are then coded into a message and passed to the TFU transmitter. The transmitter will finally distribute the message to the next TFUs in the line. Details of the 80 bit message transmitted between the TFUs are indicated in Table 4.1

The most important parameters which are modified at each step of the process are the track slope ($d\xi$) and the size of the RoI ($dd\xi$). The first one codes the track angle after the magnet, whereas $dd\xi$ defines the size of the RoI. All the other parameters are transmitted

Variable	Description	Nr. bits
TDI	Destination identifier	8
nξ	Number of RoIs to search	1
ξ	x coordinate at TC2	10
dξ	Minimal track slope	8
ddξ	Size of RoIs (in slopes)	8
all	Flag when hits in all TFUs (for photons)	1
η	Slope in y (non bending plane)	9
ω	Cluster width at TC2	2
BX	Bunch crossing number	8
ID	Pretrigger identifier	2
P	Initial estimate of momentum	7
$flag$	Flag to pass the message to next TFU (for photons)	1
E^+	Bremsstrahlung energy (positron hypothesis)	7
E^-	Bremsstrahlung energy (electron hypothesis)	7
nu	Not used	1

Table 4.1: Description of the message transmitted between TFUs. The description of each variable and the number of bits used are shown.

unchanged and will be used at the final stage of the calculations only. In the case of muon candidates, the slope in y (η) is updated at MU1, since the slope provided by MU4 and MU3 is not precise due to the multiple scattering in the absorbers. Calculations are based on Look Up Tables (LUTs) in order to reduce the processing time (a detailed description of the TFU logic can be found in Ref. [94]).

It is also possible to set a cut at the TFU level for events which produce a large latency. For this, the difference between the "write address" and the "read address" of the wire memory can be used to reject old messages. If the difference is bigger than a certain latency cut, the message is rejected. This cut is different for different superlayers, increasing from MU4 to PC1, since the processing time increases accordingly.

Each TFU has 24 optical receivers. Each of them receives 48 bits of hit information. Eight optical receivers are connected to one WM, which means (24*8) 384 channels are covered by each WM. The distribution and coverage of the TFUs can be seen in Figure 4.6 for PC and TC chambers.

To determine the position of the hits, geometry files are produced that allow the determination of the coordinates represented by each WM. It is assumed that each WM covers a section of the detector delimited by a parallelogram as shown in Figure 4.7. The x position of a general "wire" n at a certain y position is determined as follows (based on the parameters described in Figure 4.7):

$$x_n = x_0 + (0.5 + n)\frac{sx}{Nx} + \tan\alpha(y - y_0) \ . \tag{4.6}$$

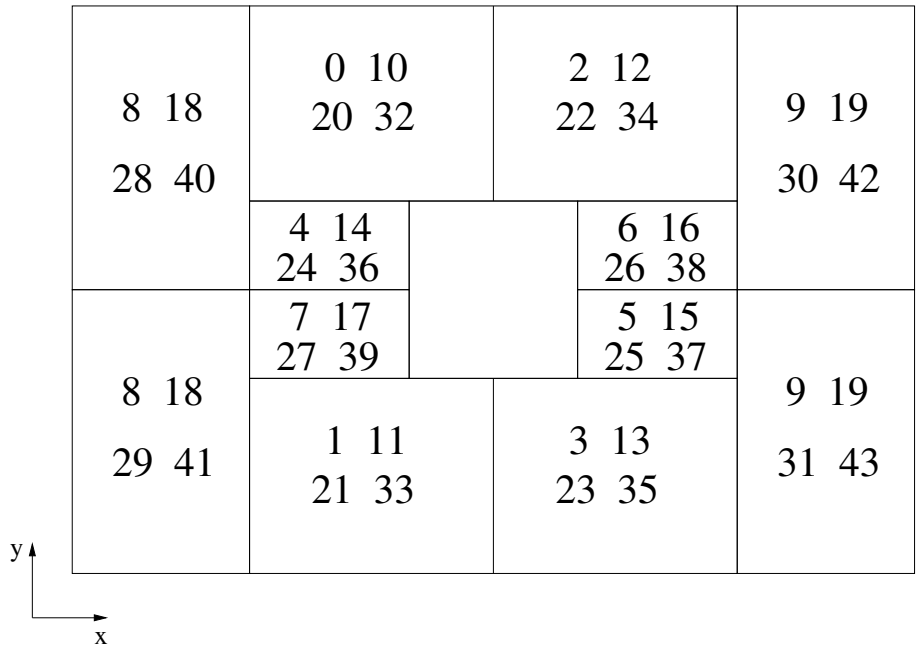

Figure 4.6: TFUs coverage for OTR chambers. TFUs numbers assigned to each superlayer as: 0-9 PC1 ; 10-19 PC4 ; 20-31 TC1 ; 32-43 TC2.

where Nx is the number of "wires" of the WM in question and the shift of 0.5 cell derives from the fact that the wire is in the middle of the cell and not at the edge.

4.1.5 Track Parameter Unit

The last TFU boards at PC1 are connected to the TPUs. These boards determine the track momentum by a propagation of the track to the center of the magnet and then to a reference target position. The charge is also determined at this stage by the bending direction of the track. In the case of electrons it is also possible to apply a cut on the ratio between energy and momentum in order to reject hadrons which also deposit energy in the ECAL. To prevent a high load of the TDU with a large number of clone tracks, the TPU is able to compare any new incoming track with the last 20 messages. The most significant bits of the momenta are compared, and if they are identical the clone is removed from the list. A description of all the parameters and their discriminating settings can be found in Ref. [95], which is reproduced in Table 4.2. A detailed description of the TPU can be found in Ref. [96].

4.1.6 Track Decision Unit

The Track Decision Unit is the final step of the FLT. It makes the decision whether the event is accepted or rejected. It can work in two different modes. One of them is the

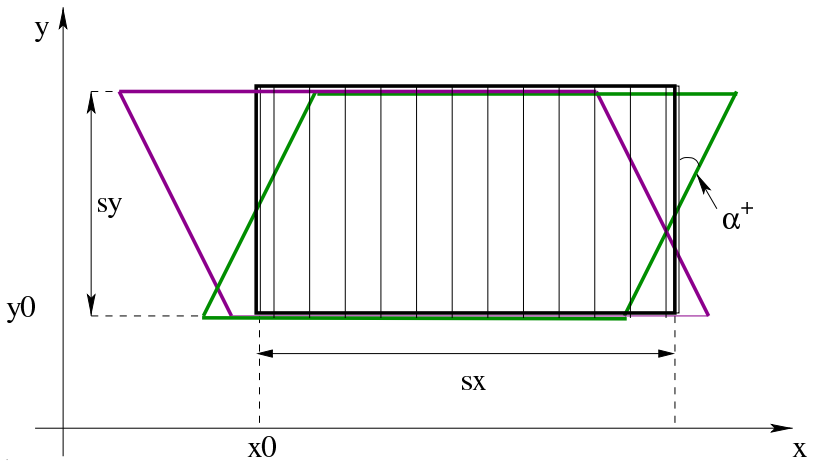

Figure 4.7: TFU geometry. The geometry assigned to the WMs is shown. The parallelogram is defined by the starting coordinates (x_0, y_0), the size sx and sy, and the angle of the layer (α).

Parameter	Description	Cut value 2002-2003
Track Cut	Maximum number of track to be processed	23
Compare Status	Remove tracks with similar kinematic (clones)	enable
P_t^{min}	Minimum P_t of track	0.5 GeV
P_t^{max}	Maximum P_t of track	1000 GeV
P^{min}	Minimum P of track	0 GeV
P^{max}	Maximum P of track	200 GeV
$(E/P)_{min}$	Minimum energy- momentum ratio for electrons	0.5
$(E/P)_{max}$	Maximum energy- momentum ratio for electrons	2
En. Brem.	Energy cut for bremsstrahlung corrections	disable (no correction)

Table 4.2: TPU parameters for the track selection. Together with the name of the cut and the setting for the 2002-2003 data run is shown.

"counter trigger", which makes a decision on the number of tracks of a certain type. The second mode is the "pair trigger mode" which calculates the invariant mass of the different pairs and delivers a decision based on an invariant mass cut. Further details of the TDU can be found in Ref. [97]. In the 2002-2003 run a "counter trigger" was used to select events with at least one reconstructed track and at least two pretrigger messages of the same leptonic type. If the trigger condition was fulfilled the BX-ID of the corresponding interaction is sent to the FCS. This signal is relayed by the FCS to all read out electronics to send their information to the SLB so that it is available for the SLT. The TDU also sends its track messages to the SLT. With this information the SLT can start the track search seeded by FLT tracks. This last feature was not used in 2002-2003. Rather, a second TDU was connected directly to the pretriggers, and the SLT was seeded by the pretrigger messages provided by this second TDU.

4.2 Performance

In this section we analyse some features of the FLT performance during data taking.

4.2.1 Testing the TFU geometry, mapping and cabling

As mentioned before, the FLT algorithm assumes equal spacing of the detector wires mapped into the WMs. This, however, is not really the case in the hardware, since the detector can have slightly different spacing due to, *e.g.* material between modules, imperfections of the supporting structure or incorrect closing between the two halves of the detector. In order not to lose efficiency in the tracking search, the WMs have to correspond to the position of the real wires within the size of a cell. This is checked by comparing the assumed WM position with the real position obtained from data bases of OTR and MUON. Figure 4.8 shows a typical spectrum of the difference of the WM value and the real x position versus the real position of the wire (for TFU 42: TC2, +5 degrees). The jumps of the difference are due to changes of the OTR module every 32 wires. The slope is due to a small difference of the cell size (δx) determined by the TFUs, which is calculated as $\delta x = sx/Nx$ (see Figure 4.7). This may differ from the exact cell size since the region covered by the TFU contains modules with non-equal spacing, thus the division will not yield the exact cell size. During the 2002-2003 run 98% of the WM wire positions were within a distance of half a cell from the real position, and the maximum difference never exceeded the distance corresponding to one full cell width. It is also possible to test the geometry independently from the OTR and MUON data bases, through a comparison between external reference tracks and hits in the WMs. Reference tracks are reconstructed requiring a matching segment in the ECAL and in the RICH. Since these tracks do not require any information of the OTR system, they are not affected

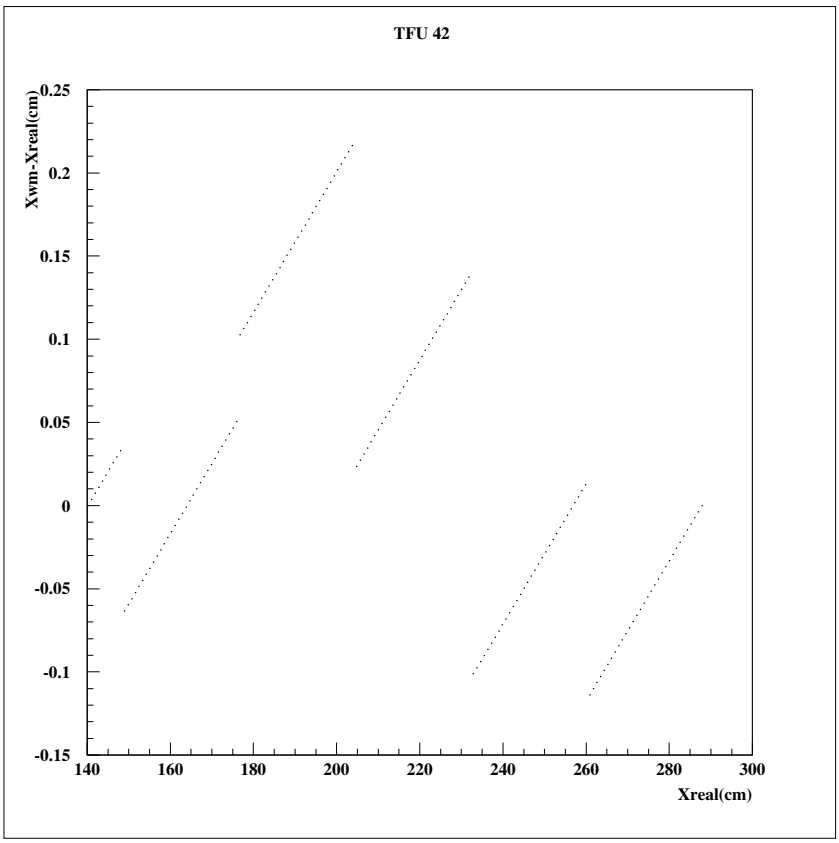

Figure 4.8: Difference between the x position assumed by the WM and the real position of the wire from the OTR data base. The slopes arise from imprecision in determining the cell size by the TFUs, and the jumps are due to positions of different modules.

by any bias. A uniform shift of the residual distributions from the central position at any layer is an indication of misalignment. Typical distributions are shown in Figure 4.9. Since the data transmission between the detector and the FLT does not contain the wire

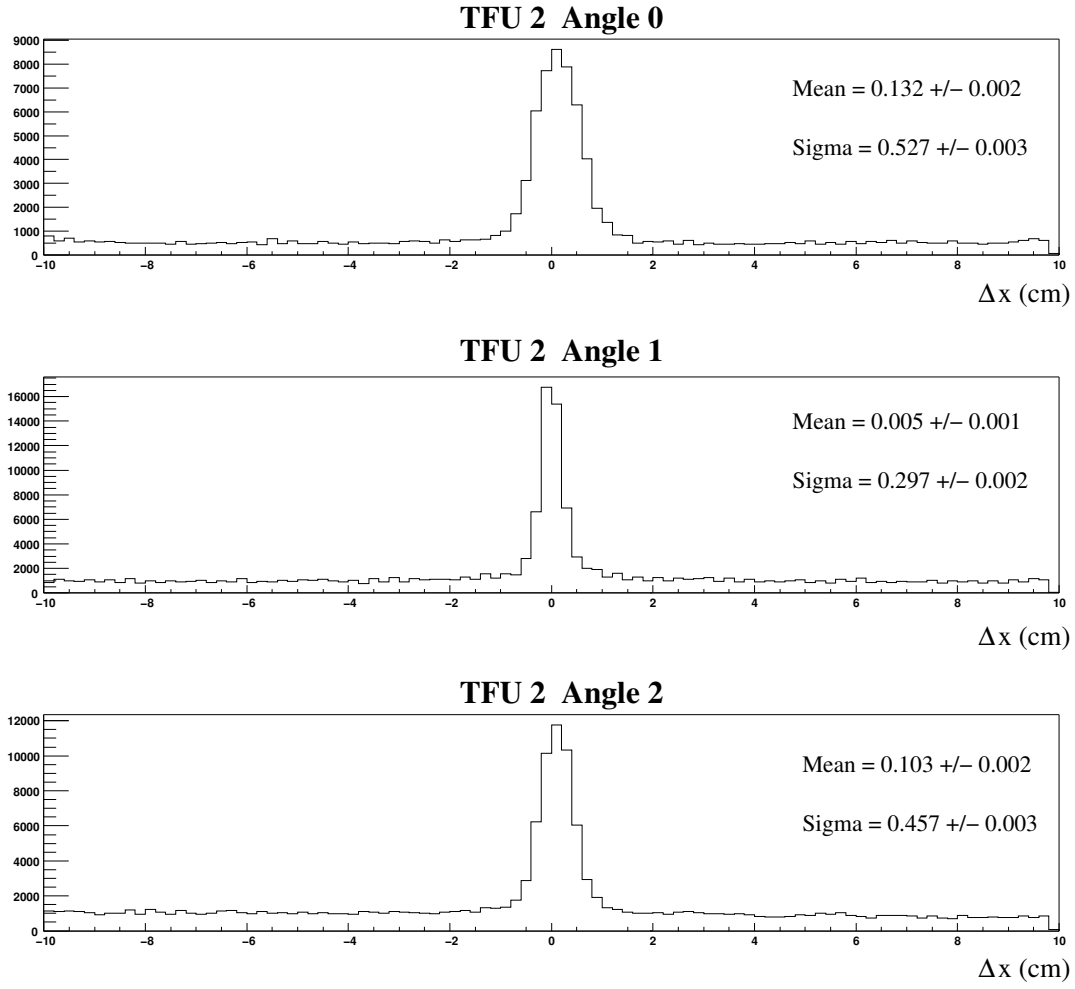

Figure 4.9: Residuals between WM hits and track positions for reference tracks in the region covered by TFU 2. The three plots correspond to the TFU coverage of the different stereo layers. Top: +5° . Middle: 0°. Bottom : -5°

identification, the assignment between the WM and the detector wires is based on the proper cable connection in the entire data path. Since the connections are done manually and there are $\sim$ 10000 ASD8-TDC connections, more than 2000 TDC-TLB cables and $\sim$ 1300 optical links, the probability of miscabling is not negligible. To have an idea of the influence of a miscabling, one has to consider that only one wrongly connected optical link would lead to the loss of 48 channels out of 348, which means that $\sim$ 10% of the affected TFUs would become inefficient. Once a cabling error is identified it can be corrected only when there is access to the detector, which depends on the accelerator status and the needs of the collider experiments. But there are cases which can be "patched up" remotely. For example if the miscabling consists simply of a swap between ASD8 $\rightarrow$

TDC or TDC → TLB cables, and the information is still contained within the 48 bits of one optical link, it is possible to reprogram the TLB to properly distribute the signal into the WMs. It is also possible to program the TLB to send hardcoded ones (signals always on, to eliminate losses) to affected TFUs. This may however cause serious increase of the number of messages, overloading the FLT network, which increases the latency. The method used to search for miscablings consists of comparing the occupancies of WMs and the tracking system. Such a comparison is displayed in Figure 4.10 [98] for TFU 16. In this case hits where acquired just before data taking. The top of the figure shows the simulated WM from the OTR hit pattern. The lower plot in the figure shows the occupancy directly from the WM records. The lines delimit the regions covered by each TDC cable and optical link. The shape of the two plots in each figure should be (very close to) identical. At the beginning of the physics runs in October 2002, problems due

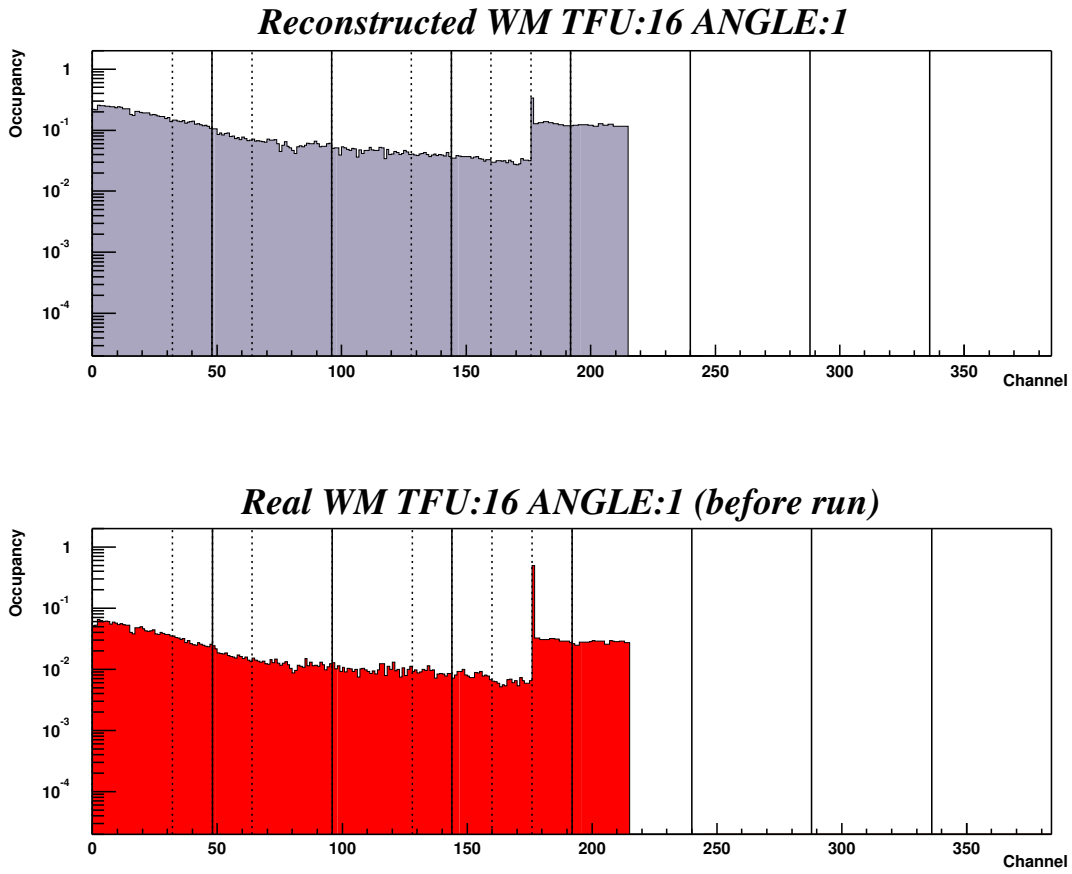

Figure 4.10: Wire memory occupancy for TFU 16, 0 ° stereo view (referred as angle 1 in the figure). The upper plot shows the *simulated* WM occupancy from the OTR hits. The lower plot shows the *recorded* WM occupancy. A difference in the two distributions would indicated a mapping or cabling problem. Occupancies are presented in arbitrary units.

to cabling and mapping were solved to a level that less than 1% channels were affected (mainly miscabling between TDCs and TLBs). Remaining channels were masked, *i.e.* the hit pattern positions were set to 1.

4.2.2 Testing the hardware and data transmission

A major problem for the FLT performance was the unreliability of the optical transmission between TLBs and TFUs. At the beginning of every run a test was performed to identify bad optical transmission links [95]. For this the receivers have programmable thresholds to discriminate between a logical 1 and 0. The test consists of increasing the threshold of the TFUs receivers and checking the counting of the 3 least significant bits. Approximately 5 % of the links showed problems. These were related to problems with the AUTOBAHN chips and optical transmitter/receiver [99]. Affected links were masked (setting all bits to 1 in the wire memory) during that particular run. Another stringent test was performed continuously during data taking. Inside the WM ASIC, the BX number of two consecutive messages are compared. Errors were counted and monitored via VME. For working links only a few showed bit error problems. The error rate observed was such that no direct influence on the FLT performance could be identified. Nevertheless, even some links that passed all this tests showed unstable or poor performance.

Another potential sources of inefficiency comes from the interconnection between the TFUs. Several tests of the data transition between the TFU and of the performance of the TFUs processing were performed. Non of these sources showed any problems [99].

4.2.3 Efficiencies

Due to the trigger set up which - during the data period 2002/2003 described here - required only one FLT track per event, it was possible to determine trigger efficiencies directly from triggered data. This could be done by selecting events where only two tracks were found in the final data analysis, and by checking whether the FLT had found the second track of the event as well. In this section we determine the trigger efficiency for offline reconstructed tracks. The reference tracks are selected using the following muon and electron criteria:

- a reconstructed segment with more than 5 hits in the VDS;
- at least 9 hits in the main tracker (OTR+ITR);
- for muons: at least 5 hits in the MUON chambers;
- consistency of the track with a SLT track;
- the transverse momentum of the reconstructed track between 0.7 an 5.0 GeV;
- the total momentum between 6 and 200 GeV;
- χ^2 probability of the track > 0.3 %;
- for muons: a muon likelihood > 0.05;

- for electrons: $-0.11 < (E/P - 0.99) < 0.21$.

The first step in the evaluation of the efficiency is to determine a matching criteria. Since there was no seeding with an FLT track, there is no standard matching between reconstructed tracks and FLT tracks. The matching criteria proposed in Ref. [100] is based on the geometrical distance between the tracks at two specific superlayers (PC1 and TC2). The distributions of the distances are shown Figure 4.11. The definition of the geometrical distance between the tracks are shown in Eq. 4.7 and 4.8 for electrons and muons, respectively. These definitions average the contributions of x and y deviations at each superlayer.

$$\Delta r_e = (|\Delta X_{PC1}| + \frac{|\Delta Y_{PC1}|}{1.5} + |\Delta X_{XTC2}| + \frac{|\Delta_{YTC2}|}{2})/4 \tag{4.7}$$

$$\Delta r_\mu = (|\Delta X_{PC1}| + \frac{|\Delta Y_{PC1}|}{4} + |\Delta X_{XTC2}| + \frac{|\Delta_{YTC2}|}{8})/4 \tag{4.8}$$

Each term of the equation is the distance between the FLT and the offline reconstructed track, at the corresponding layers, divided by a coefficient proportional to the corresponding resolutions. The values of the coefficients were determined by the distributions in Figure 4.11. For the x coordinate they are set to one and for the y directions at different bigger values since the widths are larger in this coordinate.

Figure 4.12 shows the resulting Δr. From these distributions a cut at 2 is applied to define the matching. At any cut some tracks will be lost but increasing it will also include fake matches. Different cuts values were tested (1, 2, 5 and 10) and the variation in the efficiency is taken into account in the systematic error. For events with only two reconstructed lepton candidates passing the standard requirements, one of them is matched to one of the FLT tracks in order to remove the trigger bias, and then it is checked whether or not the second reference track is found by the FLT or not. With this procedure it is possible to determine the FLT single track efficiency as:

$$\epsilon = \frac{n}{N} \tag{4.9}$$

where n is the number of matched tracks and N is the total number of reference tracks.

Figure 4.13 shows the single track efficiency as a function of the dilepton mass. An enhancement at the J/ψ mass is seen (mainly for electrons). This implies that in the presence of two real leptons the trigger probability increases.

An interesting feature of the trigger system is revealed when one studies the dependence of the OTR occupancy as function of the dilepton mass. In this distribution (Figure 4.14) it is seen that the occupancies decrease at the J/ψ mass region. This may imply (though not conclusively) that when there are two good leptons coming from a J/ψ , the probability to trigger is much less dependent on the occupancy of the detector, and the trigger tends

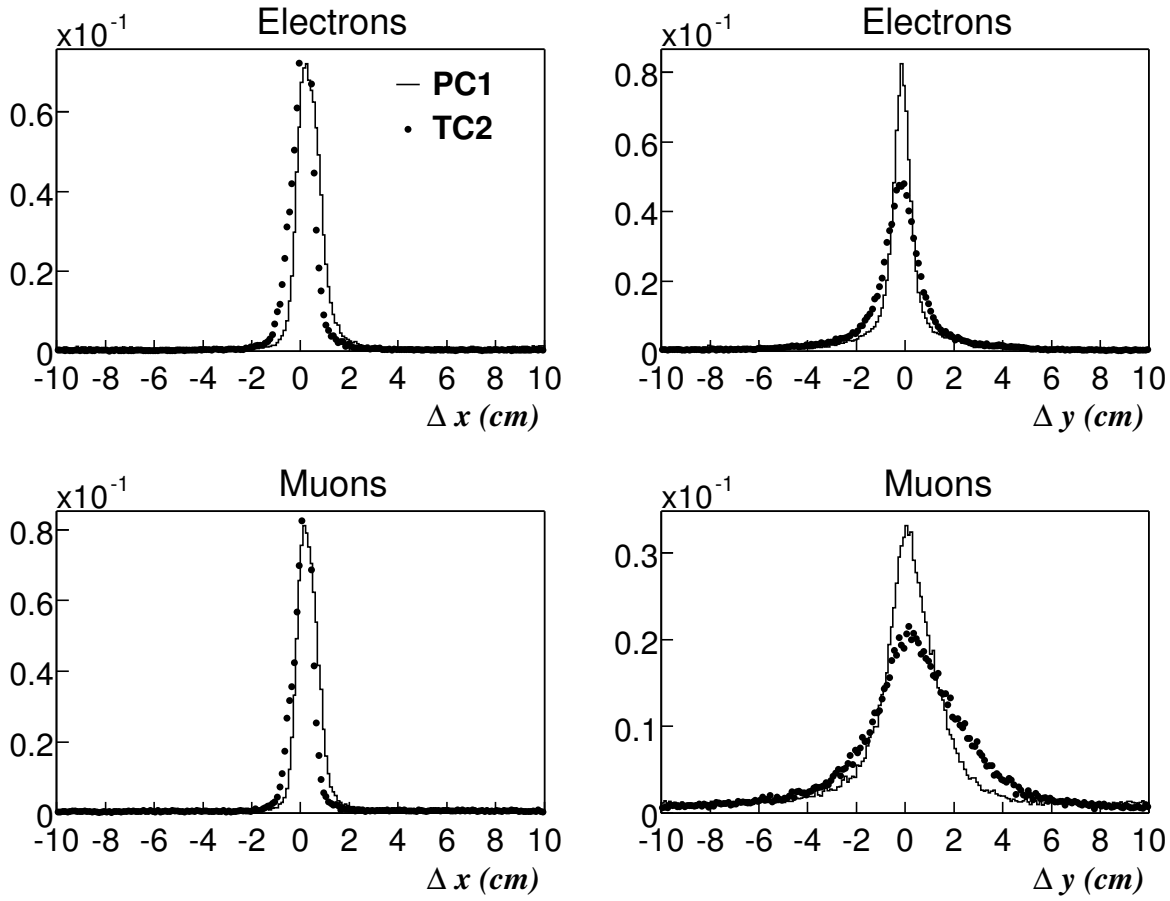

Figure 4.11: Distance between the FLT track and the closest lepton track from a J/ψ candidate. Top: Electron distributions in x (right) and y (left) coordinates for the superlayers PC1 and TC2. Bottom: Same distributions for muon tracks.

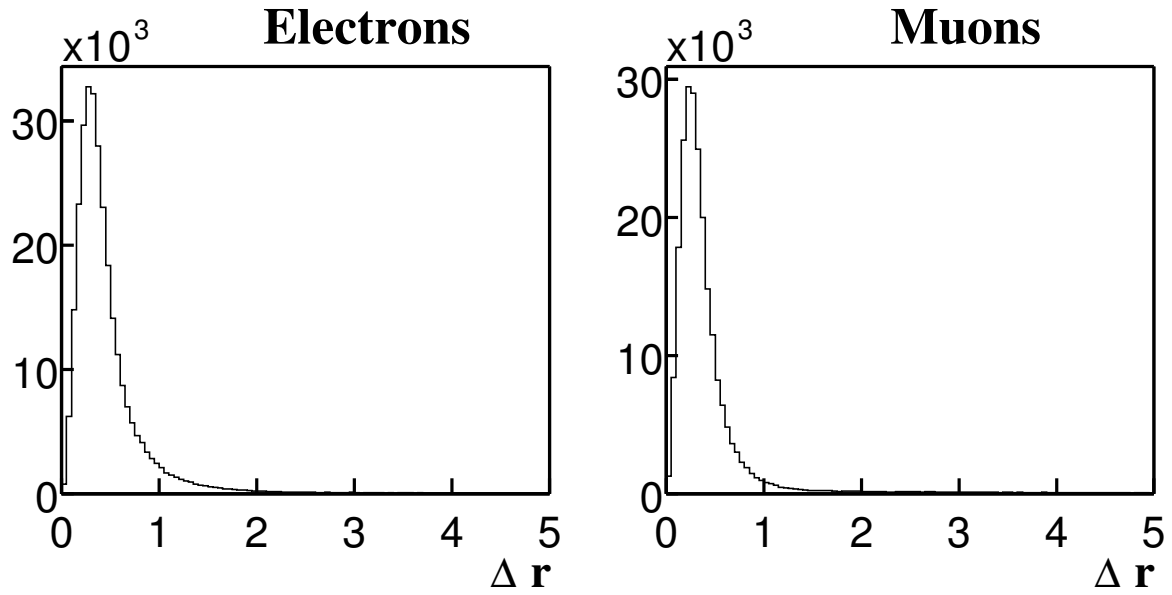

Figure 4.12: Δr between the FLT tracks and the closest lepton from a J/ψ candidate. Right: Electrons. Left: Muons.

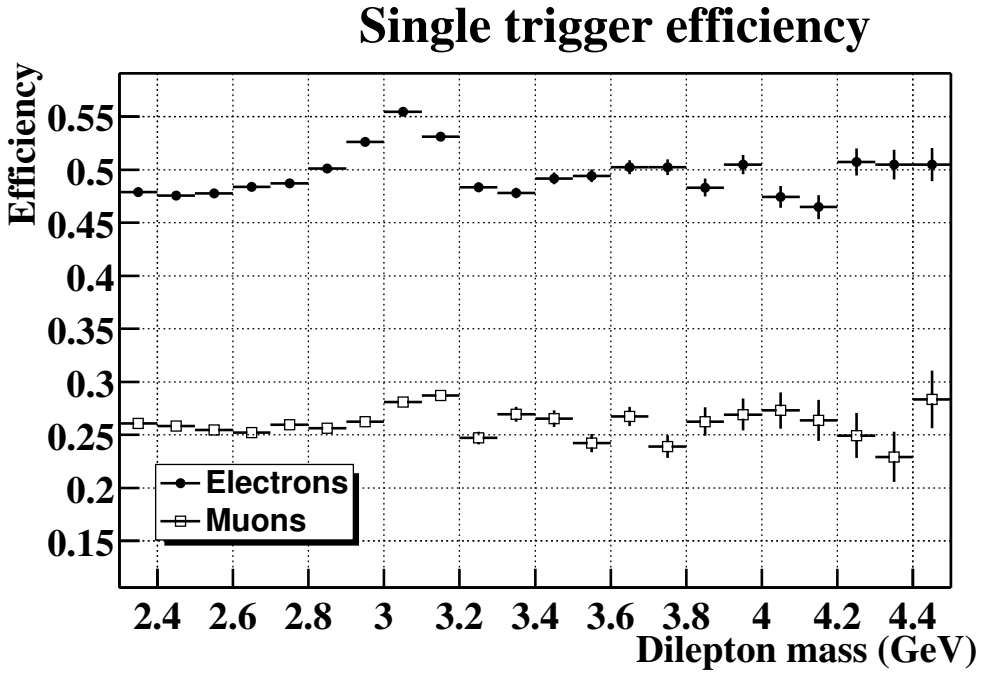

Figure 4.13: FLT trigger efficiencies. vs. dilepton mass.

Single track efficiency	October	November	December	January	February
Electrons (%)	47.2 ± 0.6	62.3 ± 0.4	65.9 ± 0.7	63.9 ± 0.3	52.3 ± 0.6
Muons (%)	22.0 ± 0.4	30.6 ± 0.3	34.7 ± 0.7	29.1 ± 0.2	22.3 ± 0.4

Table 4.3: Electron and muon efficiencies (with statistical errors) for different periods of data taking, grouped into periods of one month.

to fire based on the J/ψ leptons. The distributions suggest also that in the absence of a J/ψ , the trigger system tends to trigger more frequently on high occupancies events where it is more probable to reconstruct tracks.

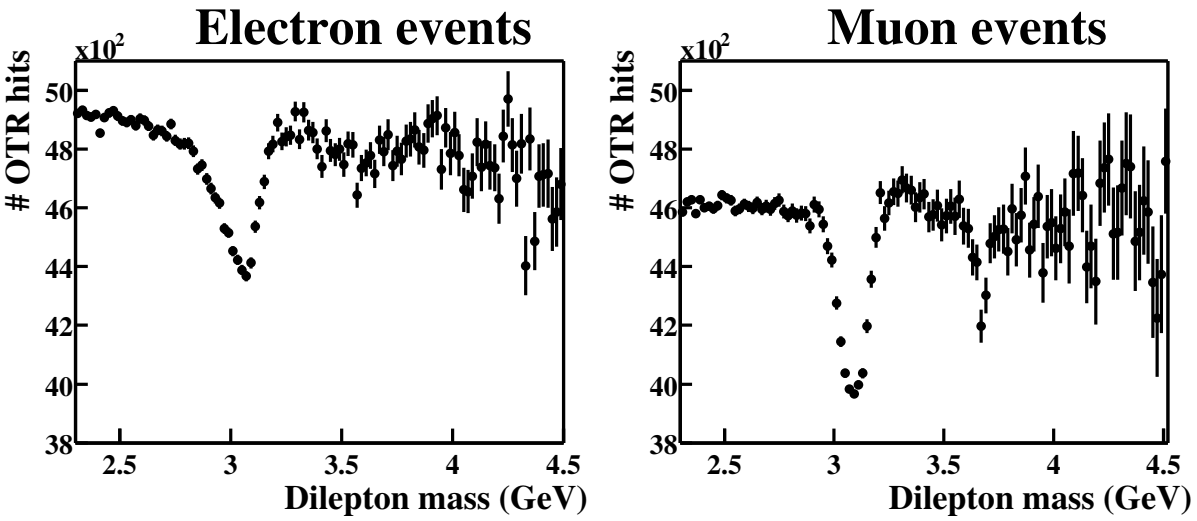

Figure 4.14: OTR hit occupancies vs. dilepton mass. Right: Electron triggered events. Left: Muon triggered events.

Here we are interested to determine the efficiency for J/ψ leptons only. For this, only pairs in the region of 300 MeV (total width) around the J/ψ mass (3.093 GeV) are selected. However, since this sample also contains non J/ψ events, the background is subtracted based on the behaviour of candidates in the side bands between 0.2 and 0.35 GeV to both sides of the J/ψ window.

It turned out that the efficiencies varied between different periods, and sometimes on a run to run basis. This was mainly due to the unstable performance of optical transmission links. Figure 4.15 shows the efficiency for different runs from October until February (the different periods are marked explicitly with vertical dashed lines). Tables 4.3 shows the efficiencies for monthly periods (with the statistical errors only).

The main systematic error in the efficiency determination comes from the definition of the matching between the tracks. The variation of the efficiency for different matching criteria is evaluated as shown in Table 4.4 for electrons and muons.

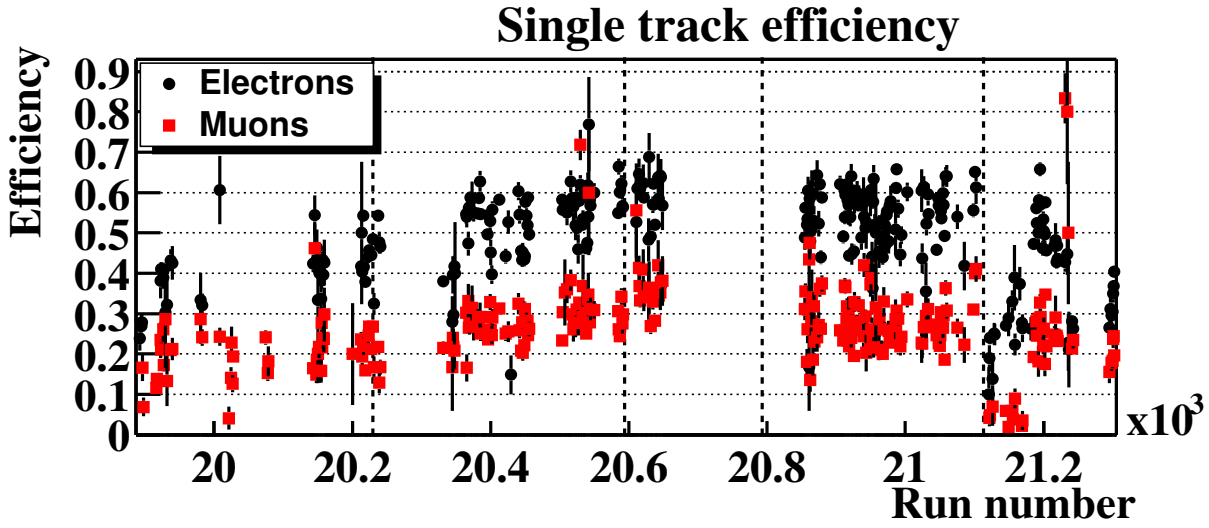

Figure 4.15: Trigger efficiencies for different runs. Dashed lines separate different runs periods.

Single track efficiency	Δ r $<$ 1	Δ r $<$ 2	Δ r $<$ 5	Δ r $<$ 10
Electrons (%)	59.6 $\pm$ 0.2	61.1 $\pm$ 0.2	62.1 $\pm$ 0.2	63.2 $\pm$ 0.2
Muons (%)	27.7 $\pm$ 0.1	28.0 $\pm$ 0.1	28.4 $\pm$ 0.1	29.8 $\pm$ 0.1

Table 4.4: Electron and muon efficiencies for different matching criteria. The systematic error contribution is evaluated based on the maximum and minimum efficiency values of this table : (max-min)/$\sqrt{12}$.

Finally, the average single track efficiency for the complete data taking of 2002-2003 is:

$$\text{Electron single track efficiency} = (\mathbf{61.1 \pm 0.2_{stat} \pm 1.0_{sys}})\% \tag{4.10}$$

$$\text{Muon single track efficiency} = (\mathbf{28.0 \pm 0.1_{stat} \pm 0.6_{sys}})\% \tag{4.11}$$

Once the average single track efficiency (ϵ) is determined for a large data sample of a certain run period, the average trigger probability can be estimated for events with only two leptons satisfying the selection cuts ($\sim$ 95% of the events):

$$\text{Trigger Efficiency} = 1 - (1 - \epsilon)^2 \ . \tag{4.12}$$

This allows to estimate the average trigger efficiency, for the complete data taking period as 85 % and 48 % for electrons and muons, respectively.

The performance of the detector is not homogeneous so that the FLT efficiency depends on several parameters. The strongest dependence is the geometrical position of the tracks, since different positions imply that the track passed through different sectors of the detector covered by different FLT hardware, which might have different performances. Most of the commissioning effort was concentrated in the regions of higher occupancies, at the expense of the performance of the hardware covering the outer parts of the detector. Efficiencies are also dependent on the particle momentum, which have also a correlation with the efficiencies from different areas of the detector. For example low momentum particles are deviated at the magnet and bent towards the outer part of the detector away from the beam pipe. In Figure 4.16 we show the single track efficiency versus the momentum of the track and the dependence on the radial distance to the beam position.

4.2.4 Difference between electrons and muons

There is a clear difference between the efficiencies for electrons and muons, the latter being lower. This was studied in Ref. [101, 94]. The inefficiencies are (geometrically) localised at the MUON chambers, particularly at MU1, where there is a large drop in efficiency. The main cause is that due to multiple scattering, sometimes the hits on MU1 are outside the projected ROI estimated at MU3. Figure 4.17 shows the evolution of the efficiency at the different layers. The study was done reading the hit occupancy of the detector and simulating the FLT performance, so that inefficiencies due to data transmission are not included. The dashed lines show the result without chamber inefficiencies since the reference tracks were selected with the requirement of hits in all tracking stations, and the solid lines include chamber inefficiencies.

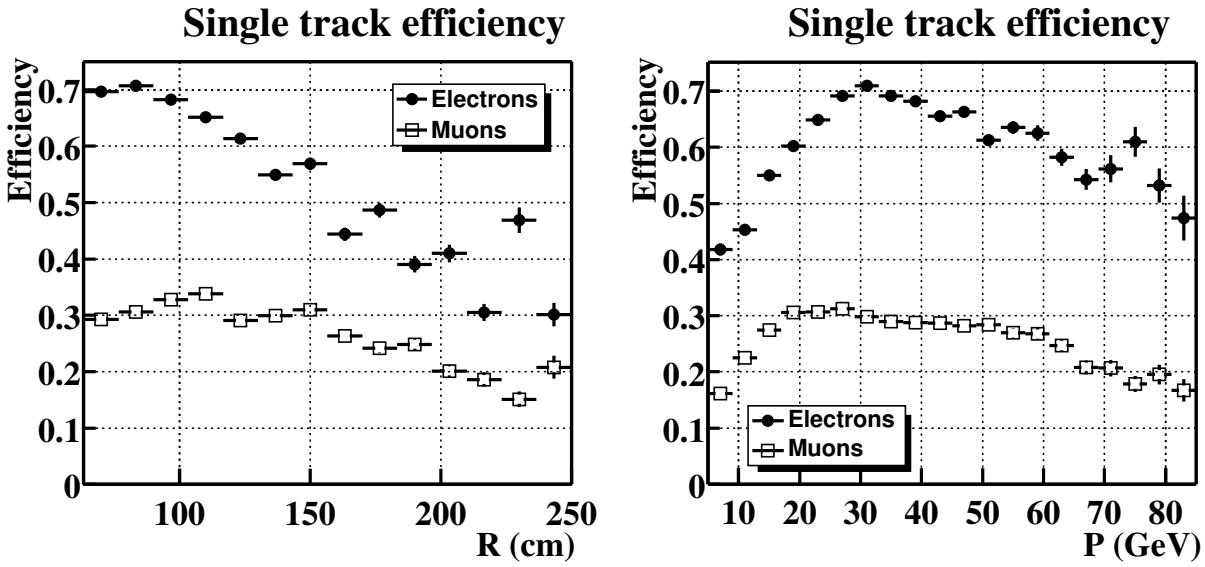

Figure 4.16: Left : Single track efficiency vs. radial distance (R) to the beam pipe at TC2. Right: Single track efficiency vs. lepton momentum.

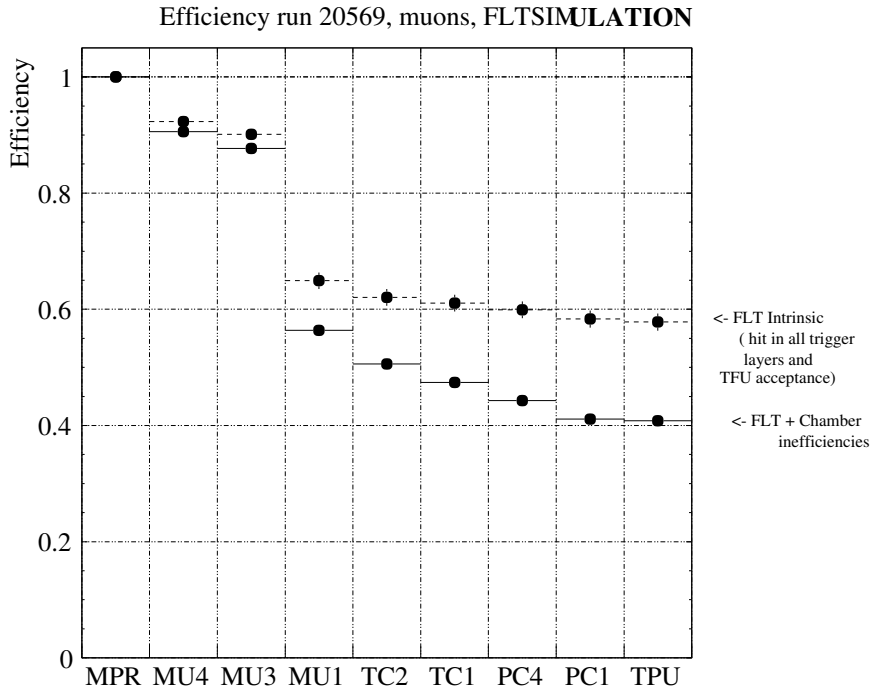

Figure 4.17: Muon efficiency at different track stations, taken from Ref. [101]. Solid lines show the total efficiency, dashed lines shows the intrinsic FLT efficiencies excluding the chamber inefficiencies. Inefficiencies due to data transmission are not included.

4.3 Simulation vs. hardware

Simulating the real performance of the trigger turned out to be problematic, mainly due to the instability of the optical transmission. The simulation was tested by giving as input the hit map from the detector and the simulation of the FLT processing. The simulation overestimates the hardware performance by 10-20 %. Figure 4.18 shows the systematic difference for different runs at different time periods. It highlights the inaccuracy of the simulation of the optical transmission performance.

For special runs all TFUs from a certain sector were connected to a TDU. Then track parameters at each station were known. The hit pattern of the detector was simultaneously passed to the simulation and a comparison was done step by step in the process. This allowed a clear identification of the problems on the optical data transmission on particular TFUs. This forced the development of an alternative method to simulate the FLT for acceptance studies.

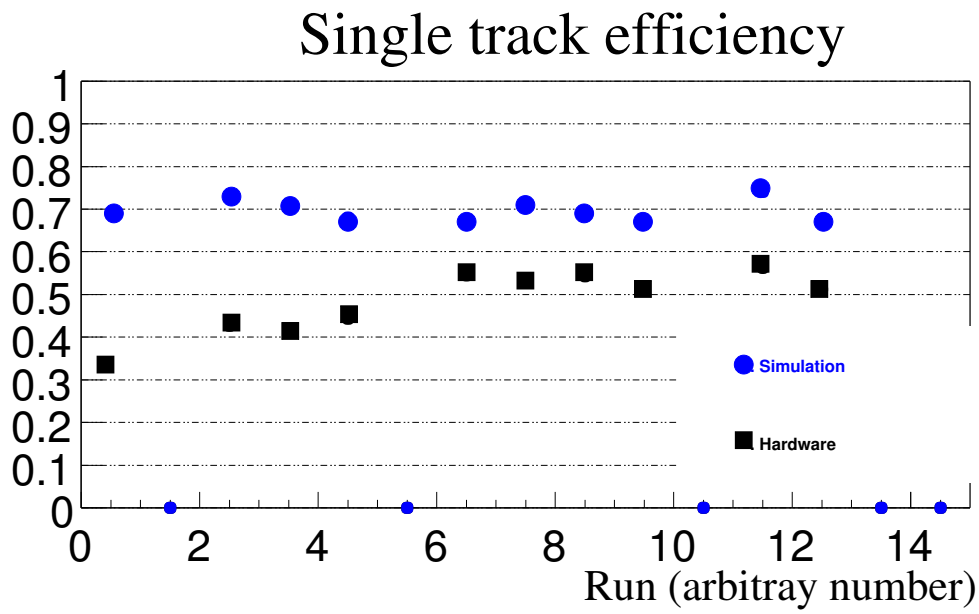

Figure 4.18: Comparison of the electron single track efficiencies for different runs (October period) for data and a simulation package of the FLT.

4.4 Efficiency map

As an alternative to the simulation one can determine a map of trigger efficiencies (from data) as function of the track position at TC2 and momentum defining three dimensional bins or cubes. The cubes are defined by the x and y positions at TC2 superlayer and a third variable proportional to the track momentum. The method to produce efficiency

maps is described in [100]. The overall single tracks efficiency map is shown in Figures 4.19 and 4.20, integrated over all track momenta.

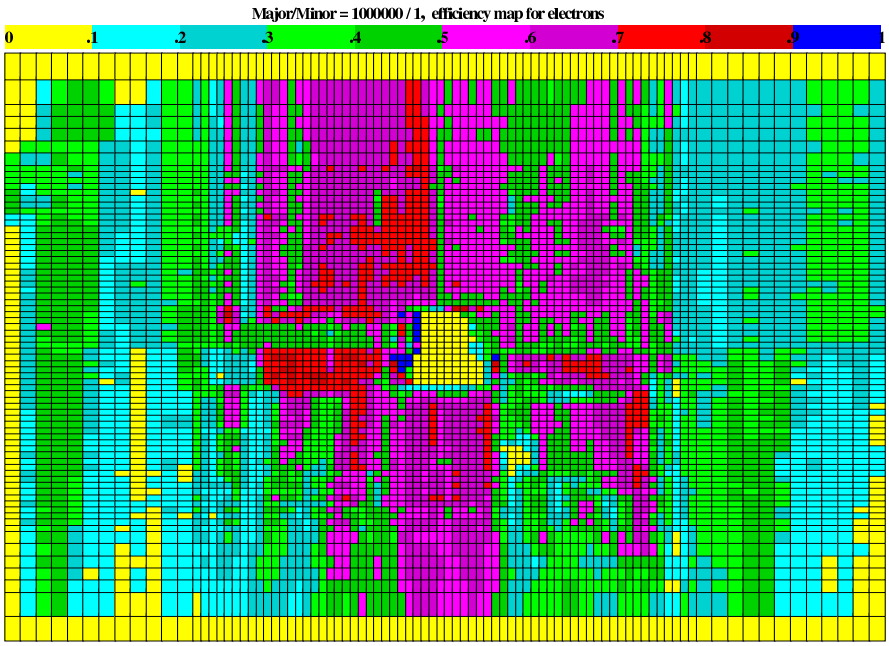

Figure 4.19: Display of the $x - y$ projection at TC2 of the efficiency map (integrated over momentum) for electrons.

The mapping is done with reference SLT tracks. Since the FLT and the SLT trigger independently on the event, their order can be reversed in the MC simulation. Figure 4.21 shows the data taking scheme and 4.22 shows the simulation scheme. In the MC simulation, the FLT efficiency map is used as a weight of the event after it was accepted by the SLT simulation. The weight of the event is the probability of the event to be triggered and is determined from the single track efficiency of all SLT tracks of the events as:

$$\text{Trigger Weight} = \left(1 - \prod_i (1 - \epsilon_i)\right) \tag{4.13}$$

where i runs over all the SLT tracks in the event (after a proper clone removal), and ϵ_i is the track efficiency determined through the efficiency map according to the track position at TC2 and momentum.

The efficiency map is applied at the MC to J/ψ events, but as we showed previously the trigger efficiencies are enhanced at the J/ψ mass due to the enhanced lepton presence at this particular mass range. Outside the J/ψ mass region the presence of fake tracks will produce an underestimate of the efficiencies. Thus taking SLT tracks without any lepton requirement results in an underestimate of the track efficiency because the sample is dominated by ghost and low quality tracks. To produce efficiency maps with only

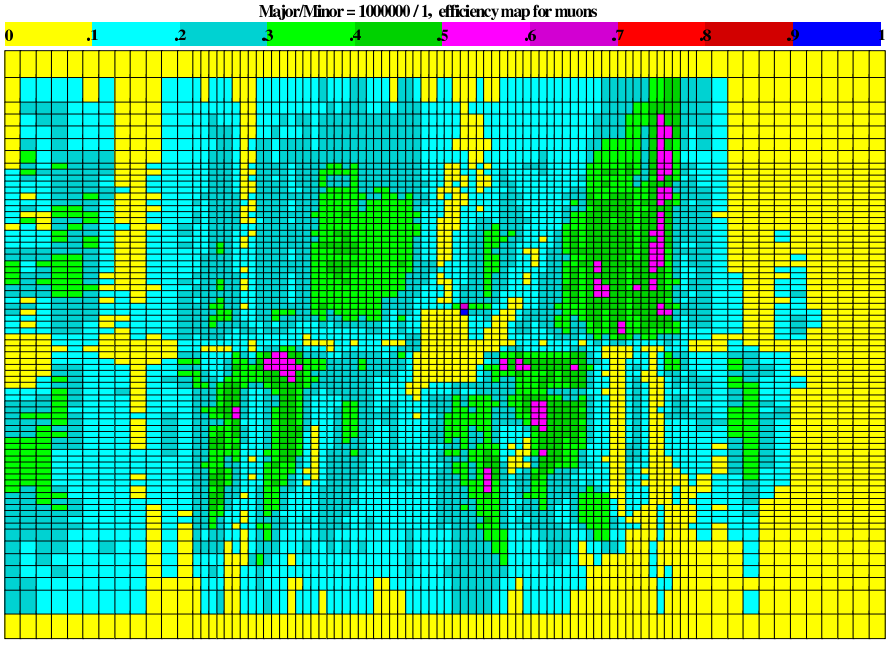

Figure 4.20: Display of the $x - y$ projection at TC2 of the efficiency map (integrated over momentum) for muons.

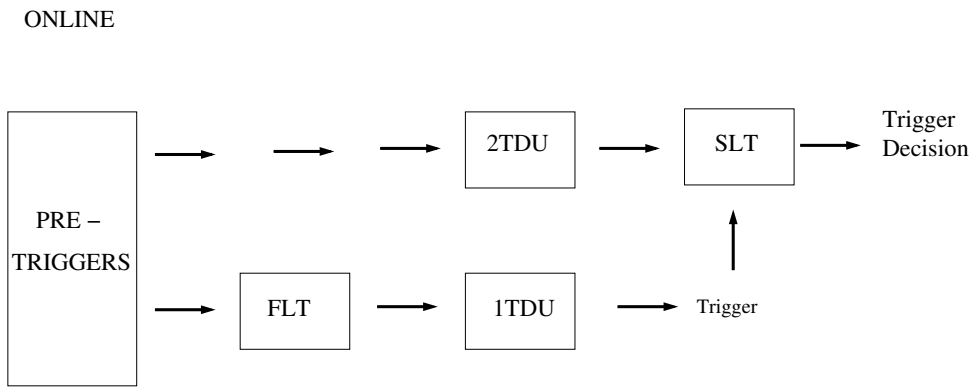

Figure 4.21: Data trigger scheme. From the pretrigger messages the FLT requires at least one reconstructed track. After a positive trigger the SLT start a tracks search based on the pretrigger seeds transmitted directly from the second TDU. The SLT issues a trigger based on dilepton candidates.

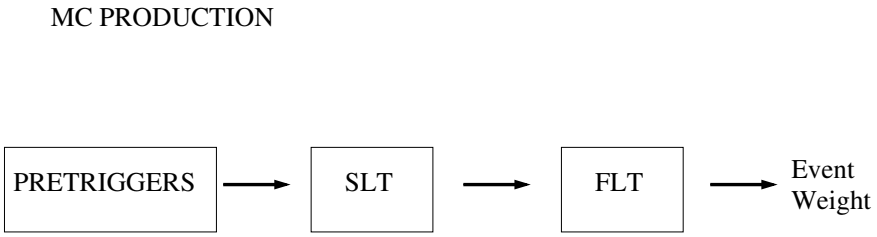

Figure 4.22: MC simulation trigger scheme. Since the SLT is not seeded by FLT tracks but makes a track search from pretrigger information, the order between FLT and SLT can be switched. The performance of the FLT is then simulated by an efficiency map, that gives a event weight based on the tracks found by the SLT (Eq. 4.13).

J/ψ leptons is not possible because of the limited statistics. Thus quality cuts must be applied to select good leptons as reference tracks but without an invariant mass cut in order to keep the statistics at a reasonable level [102]. A compromise that allows events in the wider mass region but still assures the leptonic quality of the reference tracks must be made. For muons a standard muon likelihood cut of 0.05 was enough to have a reliable reference sample. For electrons it was required that the reference track have a bremsstrahlung photon associated to it. Bremsstrahlung photons are emitted before the magnet because of the interaction of the electron with detector material. Before the magnet both electron and photon will travel in the same line, while in the magnet the electron will be deviated. It is possible to recover the emitted photon by extrapolating the VDS segment of the electron track as a straight line to the ECAL and look there for an energy deposit. This helps to correct the momentum of the electron but serves also as a strong electron tag [103].

4.5 No matching

There are some events where the FLT triggers on something different than J/ψ leptons. It is not clear what triggered these events, but for consistency, these events must be excluded from the analysis, since is not possible to determine the efficiency of such events in the simulation. Table 4.5 shows the percentage of events without matching for different matching criteria.

	Δ r < 1	Δ r < 2	Δ r < 5	Δ r < 10
Electrons (%)	6.2	4.0	2.7	1.4
Muons (%)	6.9	5.1	3.1	1.8

Table 4.5: Percentage of events with no matching between the J/ψ leptons and the FLT tracks.

4.6 Comparison between data and MC

In order to establish how well the MC describes the data, a comparison is made. The calculation of the single track efficiencies in real data is done as explained before.

The "average" trigger efficiencies can be compared in data and simulation events for a large sample of events. The average trigger efficiency from data is then compared with the average MC trigger weight for events with only two SLT tracks corresponding to the J/ψ leptons. Here we show a study for the data taken during November period. Table 4.6 shows the average trigger efficiencies for data and MC events. There is reasonably good agreement.

	Data	Simulation
Electrons (%)	85.8 ± 0.3	82
Muons (%)	51.8 ± 0.4	51

Table 4.6: Average efficiencies for data and MC for November period

A proper description of the x_F and p_T distributions is important especially for differential J/ψ production studies. In Figure 4.23 we show the distributions for data and MC. For x_F there is in general a good agreement. A discrepancy can be seen at the larger x_F for muons. This difference is not properly understood but it involves the edges of the detector. In p_T there is good agreement and the efficiency is independent of p_T.

4.7 Summary and conclusions

In this chapter we presented a detailed description of the first level trigger. During the data taking of 2002-2003 it was operating at 5 MHz interaction rate, with a reduction factor of ~ 200. A average single track efficiency for J/ψ leptons for electrons and muons of $(61.1 \pm 0.2_{stat} \pm 1.0_{sys})\%$ and $(28.0 \pm 0.1_{stat} \pm 0.6_{sys})\%$, was measured respectively. This together with the rest of the trigger chain resulted in 1200 J/ψ per hour on tape giving a final collection of 300,000 J/ψ events in a sample of 150 million triggered events. Optical data transmission between the detector and the FLT network turned out to be problematic and its simulation not reliable. As an alternative to an FLT simulation, an efficiency map was proposed. Implementation of the map substantially improved the agreement between the MC event simulation and data.

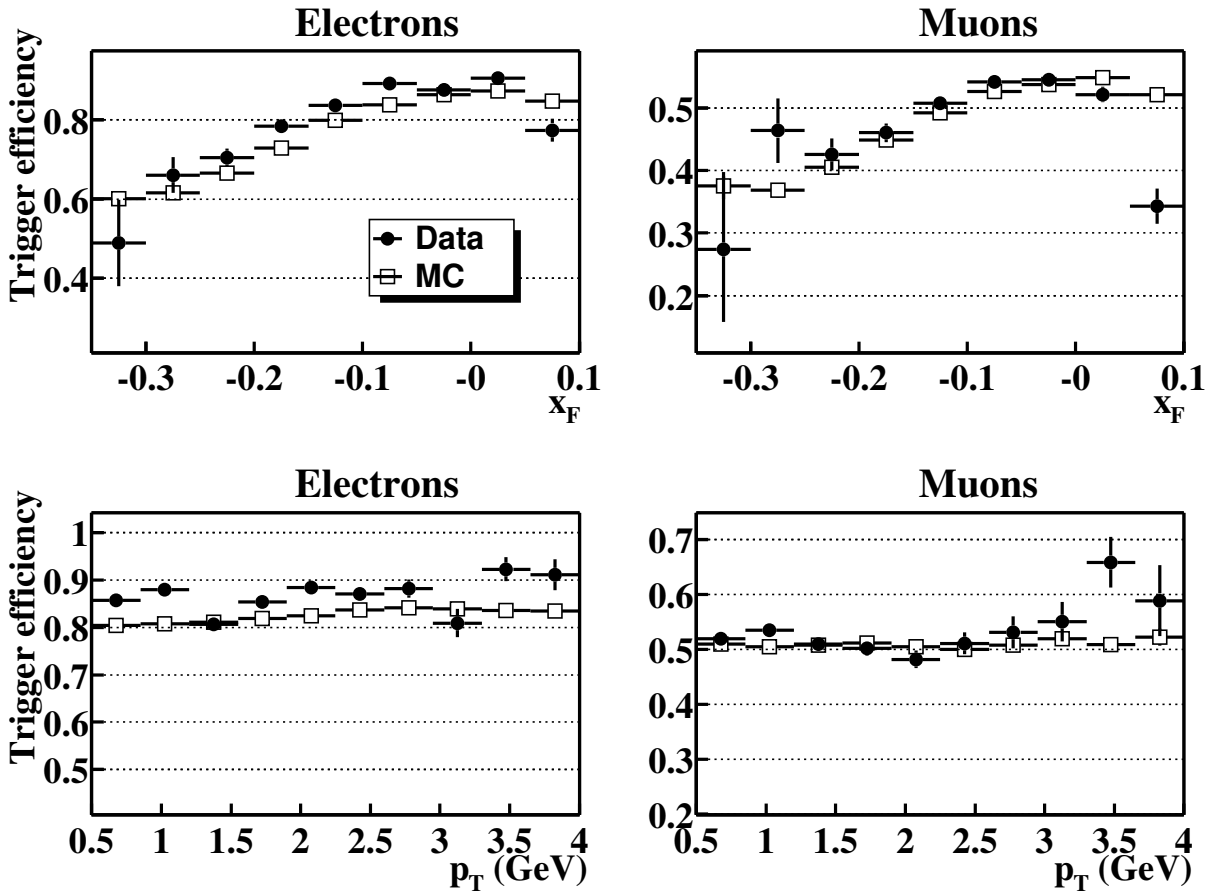

Figure 4.23: Trigger Efficiency vs J/ψ x_F and p_T

Chapter 5

The Inclusive $b\bar{b}$ Cross Section.

In this chapter we discuss the determination of the $b\bar{b}$ cross section as well as the cross section ratio to J/ψ production. First we describe the method to measure the $b\bar{b}$ cross section through the inclusive decay $b \to J/\psi$, normalised to the direct J/ψ production. Then the analysis is described, and finally the measured values are presented and compared with theoretical predictions and previous measurements.

5.1 Method

5.1.1 General

To determine the $b\bar{b}$ cross section, we identify the inclusive decay of one b particle through its decay into a J/ψ + X. Since in proton-nucleon collisions the b quarks are always produced in $b\bar{b}$ pairs, the identification of one B meson [1] is sufficient to insure the production of the $b\bar{b}$ pair. To reduce the uncertainties in the efficiencies and to avoid the determination of the luminosity, we will normalise the $b\bar{b}$ production yield to the prompt J/ψ yield. To distinguish between the prompt J/ψ and those coming from a B meson decay we will use the long lifetime of the B mesons, which leads to a typical flight path of approx. 9 mm in the HERA – B kinematics. Since there are no other long lived particles that decay into a J/ψ , a J/ψ vertex which is detached from the primary vertex is a unique indication of the presence of a B meson in the event. In Figure 5.1 the differences between detached and prompt J/ψ s are shown schematically. A J/ψ produced in the primary interaction decays immediately into two leptons (left on Fig. 5.1). The tracks of the two leptons point back to the primary vertex. In contrast, a J/ψ from a b decay occurs at some macroscopic distance from the primary interaction (right on Fig. 5.1). The two leptons, in general,

[1] As an abuse of notation we will sometimes refer the $b \to J/\psi$ decay as a B meson decay, since it is the predominant contribution, although not completely accurate since there are b baryons that also decay into a J/ψ .

do not point back to the target, giving a non zero impact parameter with respect to the wire (Iw)

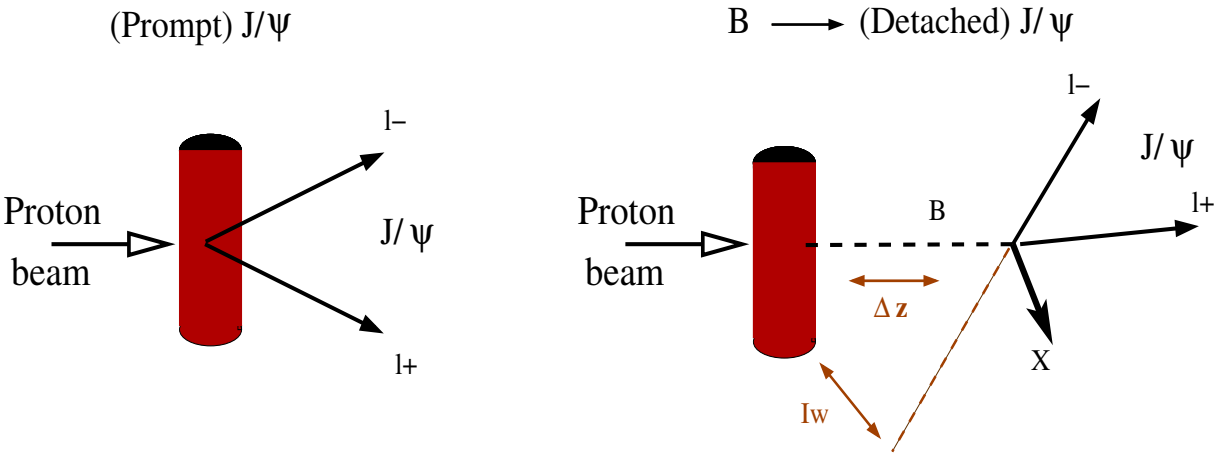

Figure 5.1: Schematic draw showing the geometrical difference between a prompt J/ψ and a detached J/ψ originated in a B decay.

5.1.2 Cross section formula

In this analysis, the $b\bar{b}$ cross section is measured through the ratio between the numbers of detached J/ψ and prompt J/ψ corrected for efficiencies and branching ratios. The measurement relative to the J/ψ cross section minimises the systematic errors related to trigger efficiencies and detector behaviour, and it also avoids the measurement of the absolute luminosity.

To determine a cross section in general, one needs to know the number of events found in the detector, the luminosity and the efficiencies to reconstruct the events. If the detection process involves a decay to some daughter particles, one needs to know the branching ratios as well. For the case of the determination of the $b\bar{b}$ production cross section through the decay to J/ψ + X, we write it, in our acceptance ($\Delta\sigma$) , as:

$$\Delta\sigma_B^A = \frac{n_B}{\mathcal{L} \cdot \epsilon_B^{tot} \cdot \mathrm{Br}(b\bar{b} \rightarrow J/\psi\ X) \cdot \mathrm{Br}(J/\psi \rightarrow l^+l^-)}, \tag{5.1}$$

where n_B is the number of reconstructed B mesons (as detached J/ψ), $\mathcal{L}$ is the luminosity, ϵ_B^{tot} the total efficiency for the b selection, and $\mathrm{Br}(b\bar{b} \rightarrow J/\psi\ X)$ and $\mathrm{Br}(J/\psi \rightarrow l^+l^-)$ are the branching ratios for a B meson decaying into a J/ψ + anything, and J/ψ decaying in to two leptons, respectively. These last two values are taken from other experiments; see Section 5.1.3. We have written explicitly σ_B^A, where A stands for the atomic number of the target material. This takes into account nuclear effects discussed in Section 1.10.

Similar to Eq. 5.1, we can write the prompt J/ψ cross section in our acceptance as:

$$\Delta\sigma_P^A = \frac{n_P}{\mathcal{L} \cdot \epsilon_P^{tot} \cdot \mathrm{Br}(J/\psi \to l^+l^-)}. \tag{5.2}$$

Here, n_P is the number of reconstructed prompt J/ψ , and ϵ_P^{tot} is the corresponding efficiency.

We can split the efficiencies in the following way:

$$\epsilon_B^{tot} = \epsilon_B^{J/\psi} \cdot \epsilon_B^{\Delta z}, \quad \epsilon_P^{tot} = \epsilon_P^{J/\psi}, \quad \epsilon_R = \frac{\epsilon_B^{J/\psi}}{\epsilon_P^{J/\psi}}. \tag{5.3}$$

The main feature is that we have factorised ϵ_B^{tot} into two parts, the first one representing the efficiency to reconstruct the J/ψ ($\epsilon_B^{J/\psi}$), and the second representing the effect of the cuts applied to distinguish between a prompt J/ψ and a detached one ($\epsilon_B^{\Delta z}$). We expect that in ϵ_R most of the uncertainties involved in the efficiency determination cancel. In principle, ϵ_R should be close to one. The differences in the kinematics of a prompt J/ψ and a J/ψ from a B decay may alter this value only in a minor way.

Inserting Eq. 5.2 into Eq. 5.1 and using Eq. 5.3, we can express $\Delta\sigma_B^A$ as

$$\Delta\sigma_B^A = \Delta\sigma_P^A \cdot \frac{n_B}{n_P} \cdot \frac{1}{\epsilon_R.\epsilon_B^{\Delta z}.\mathrm{Br}(b\bar{b} \to J/\psi X)}, \tag{5.4}$$

where n_B and n_P are extracted from the measurement, whereas ϵ_R and $\epsilon_B^{\Delta z}$ are determined from simulations.

Taking the respective nuclear dependencies into account, and considering that the efficiencies may be different for different wires due to their geometrical locations, atomic number, detector configuration and performance, etc., we write finally:

$$\Delta\sigma(b\bar{b}) = \Delta\sigma_P \cdot \frac{n_B}{\mathrm{Br}(b\bar{b} \to J/\psi\ X) \sum_i n_P^i \cdot \epsilon_R^i \cdot \epsilon_{B,i}^{\Delta z} \cdot A_i^{1-\alpha}}. \tag{5.5}$$

Here, i identifies the wire in the different configurations. The number of prompt J/ψ is taken for each wire individually. Since the statistics is too limited to do the same with the b candidates, we decided to obtain n_B from a fit to the total sample. We finally extrapolate the cross section to the full acceptance ($\sigma(b\bar{b})$),

$$\sigma(b\bar{b}) = \frac{\Delta\sigma(b\bar{b})}{f_B}, \tag{5.6}$$

where f_B is the fraction of $b \to J/\psi$ in the HERA – B acceptance ($f_B = (90.6 \pm 0.5)\%$) determined from theoretical models as shown in Section 3.2. We can also express our

result as a cross section ratio, which is a measurement independent of the reference cross section as can be seen in Eq. 5.7. This way of presenting the results makes it easy to update the absolute $b\bar{b}$ cross section if new updated values for the J/ψ cross section appear.

$$R_{\Delta\sigma} = \frac{\Delta\sigma_B}{\Delta\sigma_P} = \frac{n_B}{\mathrm{Br}(b\bar{b} \to J/\psi\ X) \sum_i n_P^i \cdot \epsilon_R^i \cdot \epsilon_{B,i}^{\Delta z} \cdot A_i^{1-\alpha}} \tag{5.7}$$

The extrapolation to the full acceptance becomes finally:

$$R_\sigma = \frac{\sigma(b\bar{b})}{\sigma_{J/\psi}} = \frac{\Delta\sigma(b\bar{b})}{f_B} \cdot \frac{f_P}{\Delta\sigma_P} = R_{\Delta\sigma} \cdot \frac{f_P}{f_B} = \frac{f_P \cdot n_B}{f_B \cdot \mathrm{Br}(b\bar{b} \to J/\psi\ X) \cdot \Sigma_i n_P^i \cdot \varepsilon_{R,i} \cdot \varepsilon_{B,i}^{\Delta z} \cdot A_i^{1-\alpha}}, \tag{5.8}$$

where f_P is the fraction of prompt J/ψ in the HERA – B acceptance ($f_P = (77 \pm 1)\%$).

5.1.3 Information taken from the literature

The J/ψ cross section and the $b\bar{b}$ to J/ψ + X branching ratio are taken from other experiments. At energies close to the one used in our experiment, the J/ψ cross section has been measured twice at Fermilab by the E789 [43] and E771 [104] collaborations. These measurements were done using the parametrisation $\sigma_P^A = \sigma(pN \to J/\psi) \cdot A^\alpha$, but with different values of α. They also used old values of the J/ψ branching ratio (5.97 $\pm$ 0.25) %. Because of this, their values are updated with the new measurements of α [46] and the J/ψ decay branching ratio (5.88 $\pm$ 0.10) %. The characteristics of these experiments and their results are summarised in Table 5.1.

	E789	E771
Beam Energy (GeV)	800	800
Target Material	Gold	Silicon
Target Mass (A)	196.97	28.09
x_f acceptance	-0.035:1.0	-0.05:0.25
α used	0.90 ± 0.02	0.920 ± 0.008
α updated	0.96 ± 0.1	0.96 ± 0.1
$\sigma(pN \to J/\psi)$ quoted (nb/nucleon)	$449 \pm 2_{stat} \pm 88_{sys}$	$381 \pm 4_{stat} \pm 27_{sys}$
$\sigma(pN \to J/\psi)$ rescaled (nb/nucleon)	$327.0 \pm 1.5_{stat} \pm 64.1_{sys}$	$333.4 \pm 3.5_{stat} \pm 23.6_{sys}$

Table 5.1: The J/ψ production cross section at 800 GeV. Characteristics and results from the Fermilab experiments E771 and E789. The cross sections per nucleon are recalculated using the latest values for α, recently measured by E866.

These measurements have been performed at $\sqrt{s} = 38.7$ GeV, slightly different from the energy at HERA – B ($\sqrt{s} = 41.6$ GeV). Thus they must be properly extrapolated to HERA – B energy according to the energy dependence given in Ref. [105], resulting in an upwards shift of 7.3 ± 0.3 %. Extrapolation of the average of the two experiments to our center of mass energy results in a reference value of $\sigma(pN \rightarrow J/\psi) = 352 \pm 2_{stat} \pm 26_{sys}$ nb/nucleon. Only $(77 \pm 1)\%$ (f_P) of all prompt J/ψ are produced within the acceptance of the HERA – B detector (-0.35 < x_F < 0.15). Then the reference prompt J/ψ cross section becomes:

$$\sigma(pN \rightarrow J/\psi) \cdot f_P = \Delta\sigma(pN \rightarrow J/\psi) = 271 \pm 4_{stat} \pm 20_{sys} \text{ nb/nucleon.} \quad (5.9)$$

The branching ratio Br ($b \rightarrow J/\psi X$) is taken from LEP1 [106], which obtained as result (1.16 ± 0.10) %. Since always two quarks are produced simultaneously, we have to double this value: Br ($b\bar{b} \rightarrow J/\psi X$) = 2· Br ($b \rightarrow J/\psi X$) = (2.32 ± 0.20)%.

5.2 Selection of dilepton pairs

5.2.1 Muon identification

Since not many particles can pass through the hadron absorber in front of the MUON chambers, a small set of cuts is sufficient to properly identify a muon. We use the following cuts:

- a track segment reconstructed in the VDS with more than 5 hits;
- at least 9 hits in the main tracker (OTR+ITR) associated with the track;
- χ^2 probability of the track > 0.3 %.

Ghost (or fake) tracks are mostly due to random hits, or to wrong matching between hits in different layers of the detector. They tend to have less hits than good tracks. Thus, requiring a minimum number of hits belonging to a given track and a minimum χ^2 probability rejects preferentially ghost tracks.

- at least 5 hits in the muon chambers;
- a muon likelihood > 0.05;

Since mainly muons can traverse the absorbers in the MUON system, a minimum number of hits in the systems serves as a clear muon identification. The muon likelihood is obtained from the MUON system and is based on the value of χ^2 of the fitted track with respect to the hits which form this track [86]. A lower cut is applied to the muon likelihood particle identification.

- the track is consistent with an SLT track;

Since the FLT efficiencies are determined with respect to tracks confirmed by the SLT, we require that the two tracks are consistent with the SLT trigger tracks which initiated the recording of the event. This avoids events where the trigger was caused by something different than the dilepton candidate. These latter cases may not be well reproduced by MC.

- the transverse momentum is between 0.7 an 5.0 GeV;
- the total momentum is between 6 and 200 GeV

A lower cut is applied to the off-line reconstructed momentum p and transverse momentum p_T to reject muons from hadronic showers in the absorbers and muons from pions and kaons decays in flight. It was determined that only particles with a momentum greater than 4.5 GeV can reach the muon system due to the absorber. Then a lower and an upper limit are applied on the momentum to eliminate unphysical tracks, with energies below and above the expected limits in our experiment. These tracks may come from wrong matching between the tracker system and the VDS, or from a random combinations of hits.

5.2.2 Selection of prompt $J/\psi \rightarrow \mu^+\mu^-$

If two good lepton candidates with opposite charge are found, a non constrained common vertex fit is performed with the GROVER package [89]. We restrict our analysis to pairs fulfilling the following conditions:

- x_F between -0.35 and 0.15;
- Vertex probability larger than 1%.

The restriction in x_F eliminates background events outside the acceptance of the detector.

In Figure 5.2 the dimuon mass distribution, including all wires and all wire configurations, is shown for candidates with a vertex at the target position ("prompt" candidates).

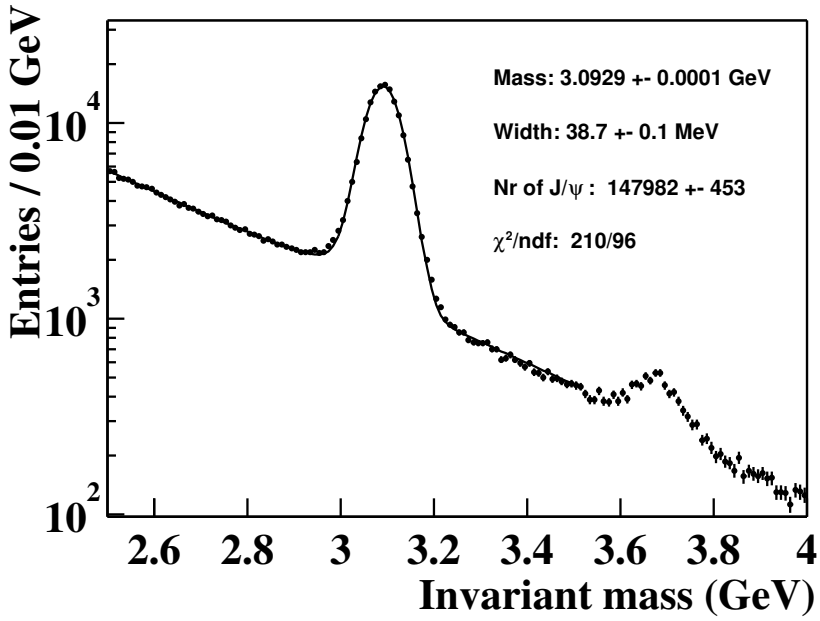

Figure 5.2: Dimuon invariant mass distribution for all the runs included in this analysis. Values of the fit of the J/ψ signal are shown. The ψ' signal is also clearly seen.

The dimuon mass distribution is commonly fitted with a function (Eq. 5.10) consisting of a Gaussian for the signal and an exponential for the background:

$$N(m) = C_{Bckgrnd} \cdot e^{-bm} + C_{Signal} \cdot exp\left(\frac{-(m - m_{J/\psi})^2}{2\sigma^2_{J/\psi}}\right). \tag{5.10}$$

This,however, does not take into account the radiative decays of the $J/\psi \rightarrow \mu^+\mu^-\gamma$, which affect the distribution at the lower mass region. An additional gaussian function with a mass dependent width is therefore added to account for this effect at masses below a certain invariant mass m_s, that is determined for the continuity of the proposed function. The proposed extra function is shown in Eq. 5.2.2 and described in [107]. As a whole, the fit function consists of:

$$\mathcal{P}(m) = \begin{cases} G(m|m_R, \sigma_R), m \geq m_s \\ \\ c_s \cdot G(m|m_R, \sigma_R(m)), m < m_s \end{cases}$$

where $G(m|m_R, \sigma_R)$ is the Gaussian function

$$G(m|m_R, \sigma_R) = \frac{1}{\sqrt{2\pi}\sigma_R} exp\left(-\frac{(m - m_R)^2}{2\sigma^2_R}\right), \tag{5.11}$$

Wire conf.	Wire	# J/ψ
I2	I2	27852 ± 195
B2	B2	7367 ± 103
I1I2	I1	8304 ± 112
	I2	8595 ± 106
I1B1	I1	8691 ± 114
	B1	8541 ± 106
B1O2	B1	17802 ± 154
	O2	20906 ± 174
B1I2	I2	8074 ± 103
	B1	10321 ± 117
B1	B1	9238 ± 111
O2	O2	3634 ± 74
B1B2	B1	3608 ± 69
	B2	5221 ± 87
TOTAL	ALL	147982 ± 453

Table 5.2: J/ψ counts in the different wire configurations and from the different wires.

m_R is the mean mass value, σ_R the standard deviation and c_s a scaling factor. Then $G(m|m_R, \sigma_R(m))$ is a similar function but with a mass dependent width $\sigma_R(m)$, which is described with a polynomial with terms to be determined by the fit procedure. The parameters c_s and m_s are determined from the continuity requirement of $\mathcal{P}(m)$ and $\mathcal{P}'(m)$ at $m = m_s$.

The final J/ψ fit function can be written then as

$$N(m, \sigma) = N \cdot \left[(1 - \epsilon_{rad}) \cdot G(m|m_R, \sigma) + \epsilon_{rad} \cdot \mathcal{P}(m, \sigma)\right], \tag{5.12}$$

ϵ_{rad} is the weight defining the relative contribution of the radiative tail to the mass spectrum and N is the number of prompt J/ψ events counted with this method. Figure 5.2 shows this function fitting the mass spectra. The fitted function differs barely from the data points. It is also possible to add an extra term to fit the ψ' spectra centred at 3.68 GeV, but this is not included in this analysis.

The mean value of the J/ψ mass is shifted by about 4 MeV with respect to the value of 3.09687 GeV given by the Particle Data Group [108]. This effect is most likely related to detector miss alignment, since differences in the global alignment (for example between VDS and OTR) can generate an incorrectly reconstructed momentum of the particle and thereby a wrong particle mass. In Table 5.2 the measured number of prompt J/ψ is shown for each wire in each wire configuration.

5.3 Primary vertex assignment

Since we base the identification of the presence of a B meson exclusively on the separation between the primary interaction and the J/ψ vertex, it is, in the case of more than one primary vertex, important to identify unambiguously the primary interaction in which ultimately the J/ψ particle had been produced. For this assignment we use the sum of the Closest Distances of Approach (CDA) between the primary vertices and the two muon tracks, plus the CDA between the reconstructed J/ψ and the primary vertex:

$$S = \frac{CDA_1^2}{\delta^2_{CDA_1}} + \frac{{CDA_2}^2}{\delta^2_{CDA_2}} + \frac{CDA^2_{J/\psi}}{\delta^2_{CDA_{J/\psi}}}. \tag{5.13}$$

We express these CDAs in terms of experimental uncertainties δ_{CDA}. Finally we select the primary vertex for which this sum is minimal.

After this assignment, the primary vertex is re-fitted without the two leptons forming the J/ψ , so that we have an unbiased determination of the primary vertex, independent of the place of production of the J/ψ . Despite the exclusion of the J/ψ leptons, there are in the case of b events still tracks belonging to the b particle which are included in the primary vertex and thus bias its position, as will be shown in Fig 5.4. In order to avoid this bias we prefer to use a cut on the distance to the wire, in order to determine the detaching distance of the dilepton vertex.

5.4 Wire assignment

For several reasons it is important in multiwire runs to determine on which wire the primary interaction that led to the J/ψ particle took place. The first reason is naturally the A-dependence of the J/ψ production cross section. In our analysis, it is even more crucial since the detachment of the dilepton candidate from the wire is the main cut which is used to separate the prompt J/ψ from those produced in the b decay (see Fig. 5.1). In addition, the trigger and reconstruction efficiencies of the prompt J/ψ and b mesons may also depend on the wire where they were produced (a detailed Table (5.5) is shown in Section 5.8) . We proceed in a similar way as for the selection of the primary vertex: first, the sum of the impact parameters of the two leptons and the J/ψ itself to each wire (5.14)

$$S = \frac{imp_1^2}{\delta^2_{imp_1}} + \frac{{imp_2}^2}{\delta^2_{imp_2}} + \frac{imp^2_{J/\psi}}{\delta^2_{imp_{J/\psi}}} \tag{5.14}$$

is calculated. Then the wire with the minimum distance is assigned to the dilepton pair. The primary vertex has also a wire assigned, and in cases that the assigned primary to the J/ψ is not reconstructed on the same wire the event is discarded. It happens that within

one event, two primary interactions occur simultaneously on two different wires. It is then possible to combine two leptons from different wires. This combination will normally result in a candidate detached from both wires, leading to a fake detached candidate. To suppress this kind of background, the leptons are required to be incompatible with the primary at the wire not assigned to it. It is estimated from simulation that the wire assigning procedure leads to less than 1% wrong wire assignments.

5.5 Selection criteria for detached $J/\psi \rightarrow \mu^+\mu^-$ events

In principle, any J/ψ count which occurs downstream of a primary interaction would be interpreted as a detached J/ψ and therefore as a B candidate. However, the experimental resolution of the reconstructed tracks and primaries, as well as the limited precision of the wire position, can transform a prompt J/ψ into a detached candidate. In order to suppress this background the limits of acceptance are set well above the experimental resolution (400 μm) with a fiducial cut of 2 mm. This cut rejects 99 % of the prompt J/ψ while keeping more than 75 % of the $b \rightarrow J/\psi$ events. Still, random combinations can cause unphysical events to pass these cuts, but such events should not generate any peak in the J/ψ mass region but present an exponential distribution as will be shown in Section 5.7. Furthermore, since they are unphysical events they can occur upstream as well as downstream of the target. Like sign lepton pairs on data allow an estimate of this kind of background. Additional physical background can arise from double semileptonic decays from $b\bar{b}$ or $c\bar{c}$ pairs. The requirement that they form a common vertex together with a requirement that this vertex must be detached will reduce this background significantly.

The principle of the selection is as follows:

- Δz (J/ψ - target wire): A lower limit of the distance between the target and the vertex of the dilepton candidate. This cut which must be passed in terms of the absolute value and of the resolution, rejects candidates coming from the target (prompt candidates).
- Closest Distance of Approach (CDA) to the primary vertex: Leptons coming from a J/ψ detached from the primary will in general not point back to the primary vertex. Thus, a lower limit on the CDA between the lepton trajectory and the primary will reject prompt J/ψ events.
- Impact to wire for each lepton: Applying a lower limit to the impact parameter of the track to the target wire rejects prompt candidates. Impact parameters to the wire are only known in two dimensions, in contrast to the impacts or CDA to the primary vertex where a full three dimensional distance can be determined. However, it has the advantage that the wire position is better known than the position of the vertex (100 μm vs. 400 μm), and it is not influenced by other tracks from a B decay as is the case of the primary vertex position.

- J/ψ Impact to wire: The large mass J/ψ , which originated in a b decay should not point too far away from the target where the primary interaction occurred. In other words the direction of flight of the J/ψ should not deviate significantly from the direction of the b particle, which is the primary interaction, thus an upper limit applied to this quantity will eliminate unphysical background events of dilepton candidates presenting a big impact parameter at the z position of the associated wire.

All these cuts together enhance the probability of detecting dilepton pairs which are produced in a secondary B decay. In addition, the requirement of a good quality vertex of the two leptons, will reject combinatorial background as well as background from double semileptonic decays of $b\bar{b}$ and $c\overline{c}$ pairs.

5.6 Comparison between data and simulation

We investigate in this section in how far the simulations reproduce the behaviour of the data. The reference sample consists of dilepton candidates in a window of 300 MeV (total width) around the J/ψ mass (3.093 GeV), this region is dominated by prompt J/ψ events, but still present background events. The background is subtracted based on the behaviour of candidates in the side bands between 0.2 and 0.35 GeV to both sides. Both samples are shown in Figure 5.3, for prompt J/ψ data candidates. The J/ψ mass region is highlighted explicitly together with the side bands, which accounts for the background events in the region of interest. The characteristics of the data after background subtraction are then compared with both MC generated prompt J/ψ and B $\rightarrow$ J/ψ events. The distributions for the main quantities which will allow us to identify detached candidates are shown in Fig. 5.4.

- Δz (J/ψ - target wire): The distribution is shown in picture a) and in terms of σ in b). In the data the J/ψ is systematically shifted 100 μm with respect to the target which is not the case in the simulation. This shift may be due to misalignment of the vertex detector, which is not reproduced in MC. Since a 9 σ cut is applied to select candidates (to be described in the next section) we are not sensitive in the analysis to this displacement.

- Δz (primary - target wire): The resolution is about 400 μm for both MC and J/ψ data samples. In the case of the B sample in picture c), a shift is clearly seen, which is probably the result of including in the vertex fit of the primary also those particles which belong to a B decay such as extra kaons, pions, or of leptons coming from the associated b particle in the event. As these particles are detached from the vertex, their inclusion into the fit tends to shift the position of the primary in the downstream direction.

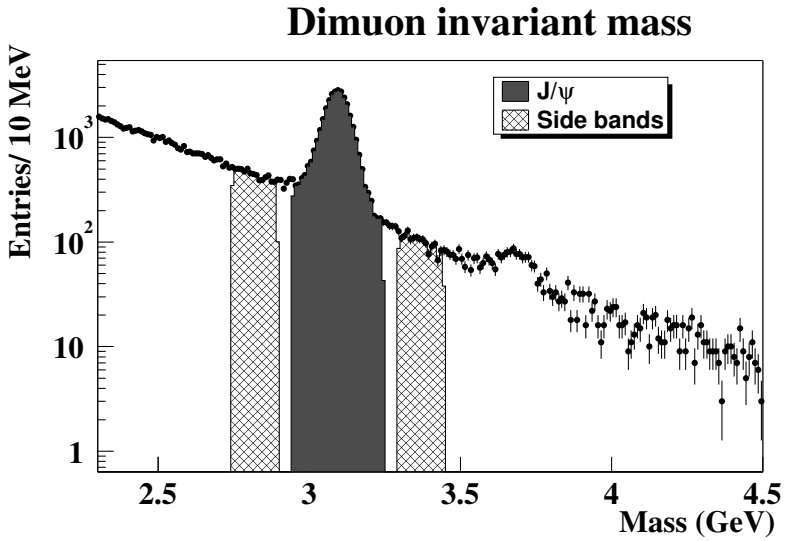

Figure 5.3: Invariant mass of dileptons pairs on data events. The J/ψ mass region and selected side bands corresponding to the background are explicitly shown.

- Single lepton CDA to primary: Good agreement in the entire range (picture e)).
- Single lepton impact to wire and J/ψ impact to wire: Shown in pictures d) and f), present good agreement in the central region . There seems to be a systematic difference for large impact parameters, but the distributions are overall compatible taking into account the reduced statistics for these large impacts.

5.7 Background description

We are interested in a proper simulation and understanding of the background, since it is an integral part of the optimisation procedure. One possible approach to simulate the background of $b \to J/\psi$ events is to take side bands of the J/ψ peak in the dilepton mass distribution. Since the statistics in data is limited, the contributions of the side bands - and therewith the final result - is very sensitive to statistical fluctuations. Also the fact that side bands in the optimisation procedure are forced to be reduced with respect to the signal may enhance artificially the signal. To avoid these problems a mixture of MC samples and data was taken to simulate the background. This includes the following samples (taking the dilepton pairs at the J/ψ mass region):

- MC $b\bar{b} \to ll$ and $c\bar{c} \to ll$, in order to simulate the double semileptonic events in the exponential background;
- Like-sign leptons from data, in order to simulate combinatorial background

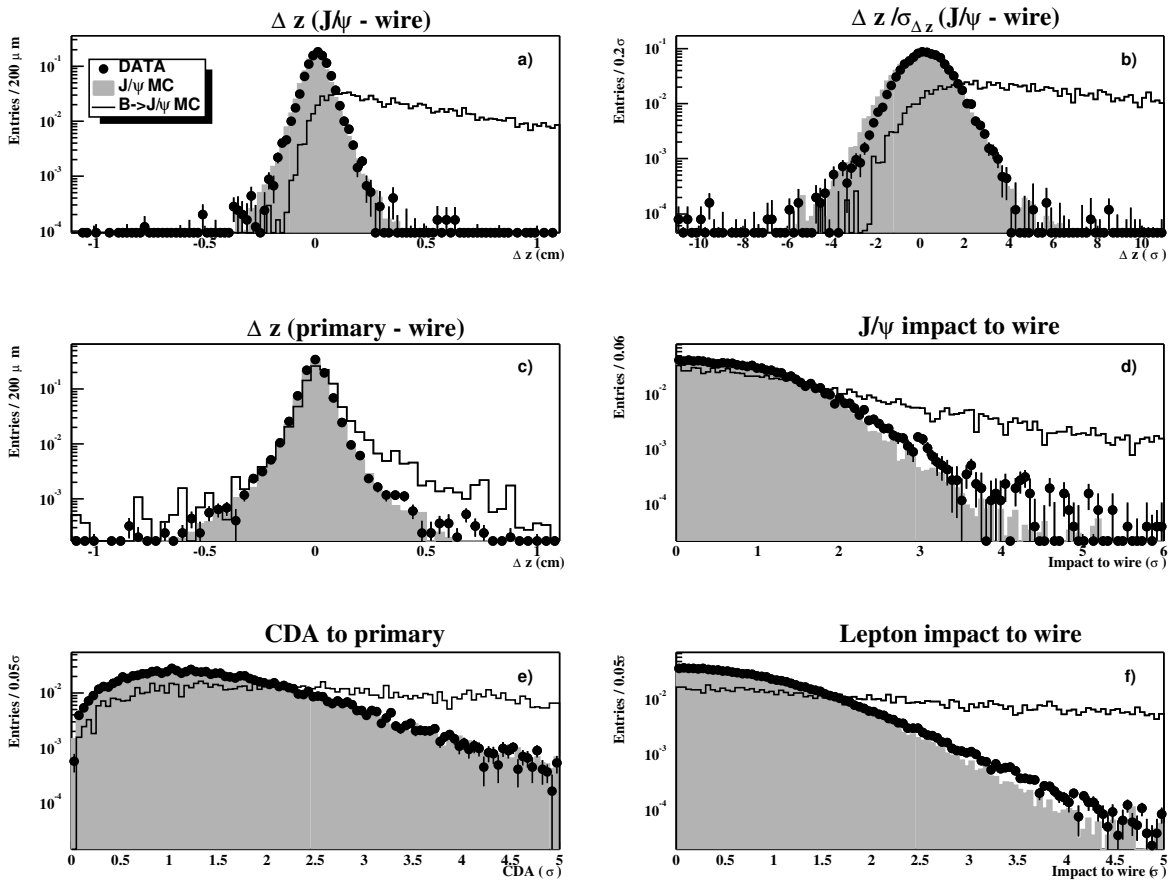

Figure 5.4: Comparison between J/ψ data with subtracted background (points with error bars), MC B $\rightarrow J/\psi$ (solid line histogram), and prompt J/ψ (shadowed histogram). a) Δ z between J/ψ and target wire ; b) Δ z between J/ψ and target wire in units of σ ; c) Δ z between primary vertex and target wire; d) J/ψ impact parameter to the wire in units of σ ; e) Closest Distance of Approach of leptons to the primary vertex ; f) Impact parameter of leptons to the target wire in units of σ.

- Prompt J/ψ MC: To simulate the prompt J/ψ background. After the optimisation procedure it is also important to consider any prompt J/ψ contamination in the detached spectrum, since (if any) they will be directly counted as signal events.

To verify how well the background is understood we investigate the following subsamples in detail: I2 , I2I1, I1B1 (only the events on the I1 wire were used in this wire configuration). The four background contributions assumed are $c\bar{c}$ and $b\bar{b}$ double semileptonic decays, prompt J/ψ and random combinatorial. For each of the MC samples a normalisation procedure is needed to estimate their real contribution. This is:

- $b\bar{b}$: This MC sample contains also $\mathrm{B} \rightarrow J/\psi$ events, which are used to normalise the sample to the number of B events on data;
- $c\bar{c}$: Normalised to the number of measured prompt J/ψ , using the known ratio of the respective cross sections;
- Prompt J/ψ : Normalised to the measured number of prompt J/ψ on data.

Figure 5.5 shows the invariant mass distribution with the detailed background contributions upstream and downstream of the target after all cuts are applied. In picture a) the background contribution in the unphysical region upstream the target is shown. Here no $b\bar{b}$ and $c\bar{c}$ events are present, but only combinatorial background. Picture b) shows the three background contributions downstream of the target. Picture c) shows the invariant mass of opposite sign pairs for events downstream of the target, together with the summed background contributions. Within statistical fluctuations the background is properly simulated and reasonably understood.

We conclude that the main contribution to the background comes from combinatorial (44.1%) and $b\bar{b}$ (43.4%) double semileptonic decays. Since charm particles do not have a long life time, their contribution to the background is suppressed (12.6%) after detached cuts are applied. No prompt J/ψ events survives the selection of detached events. In the region upstream of the target there is no physical but only combinatorial background (Picture a).

5.8 Optimisation and efficiencies

The cuts are strongly correlated, and in order to to avoid any bias, they have been optimised blindly (without looking at the signal of the data), all together, based on the criterion of the best significance ($Signal/\sqrt{(Signal + Background)}$). The signal is taken from MC decays. The background is accounted as described in the previous section. The optimisation essentially consists of making a discrete variations of all the four cuts under study and for each set of cuts determine the corresponding significance. Finally the set of

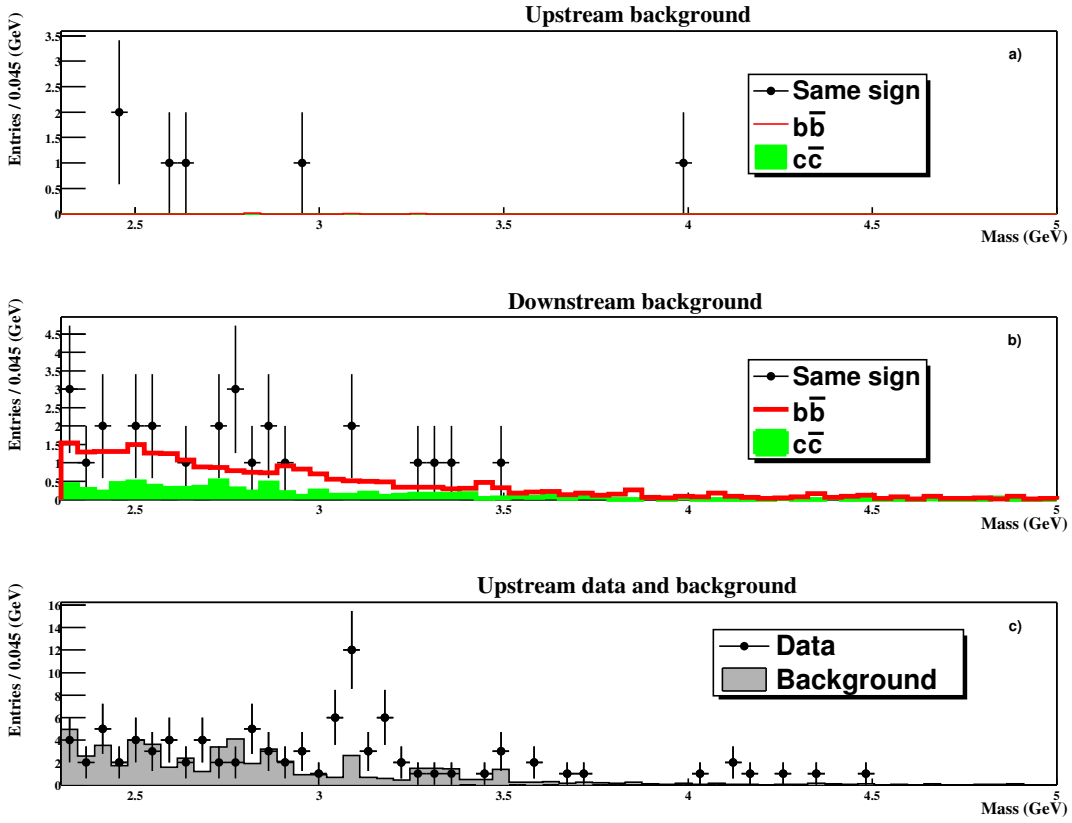

Figure 5.5: Background spectrum of detached dilepton candidates. The background consists of random combinatorial of tracks described by same sign pairs from data and double semileptonic decays in $b\bar{b}$ and $c\bar{c}$ events taken form MC and properly normalised. a) Background distribution in the unphysical region upstream of the target. Only random combinatorial background is present. b) Background distribution downstream the target. c) All three background contributions together (filled histogram) and unlike sign dimuon pairs (dots with errors), where the detached J/ψ signal can be clearly seen.

cuts at maximum significance is selected [109]. As an example, we show the result of the optimisation for the I2 wire configuration. Signal, background, significance and efficiency distributions for the main cuts (vertex displacement in z and lepton impact to the wire) are shown in Figures 5.6 and 5.7. The cuts (indicated by arrows) are placed at the value where the significance has it maximum. For each distribution all the other variables are set to the optimised values shown in Table 5.3.

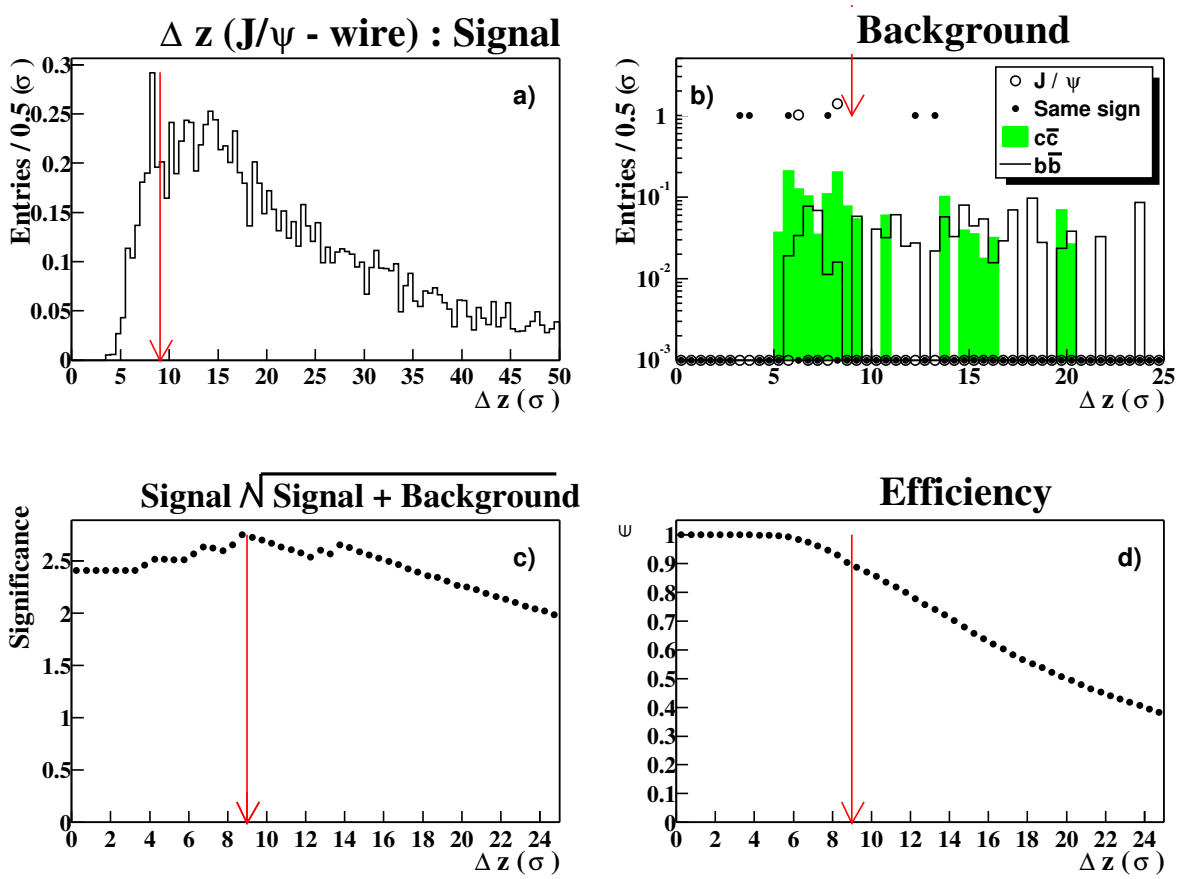

Figure 5.6: Distributions of the z distance between the J/ψ vertex and the wire position in terms of σ. a) Signal events from MC B$\rightarrow J/\psi$. b) Normalised background events composed of: MC prompt J/ψ , pairs of same sign leptons form data, double semileptonic decays of $c\bar{c}$ MC events, double semileptonic decays of $b\bar{b}$ MC events. c) Significance at each of the value cut on Δ z . d) Efficiency of the signal at each cut values. The arrows indicate the value of the cut applied to this variable.

The optimised values are shown in Table 5.3. The optimisation was applied to different single samples and samples together showing stable values on the optimal cuts.

After the cuts are set, the efficiencies are determined. Table 5.4 shows in detail the efficiencies determined for the prompt J/ψ and $b\bar{b}\rightarrow J/\psi\ X$ MC samples. The acceptance efficiency is determined based on those J/ψ events that are produced within the HERA – B

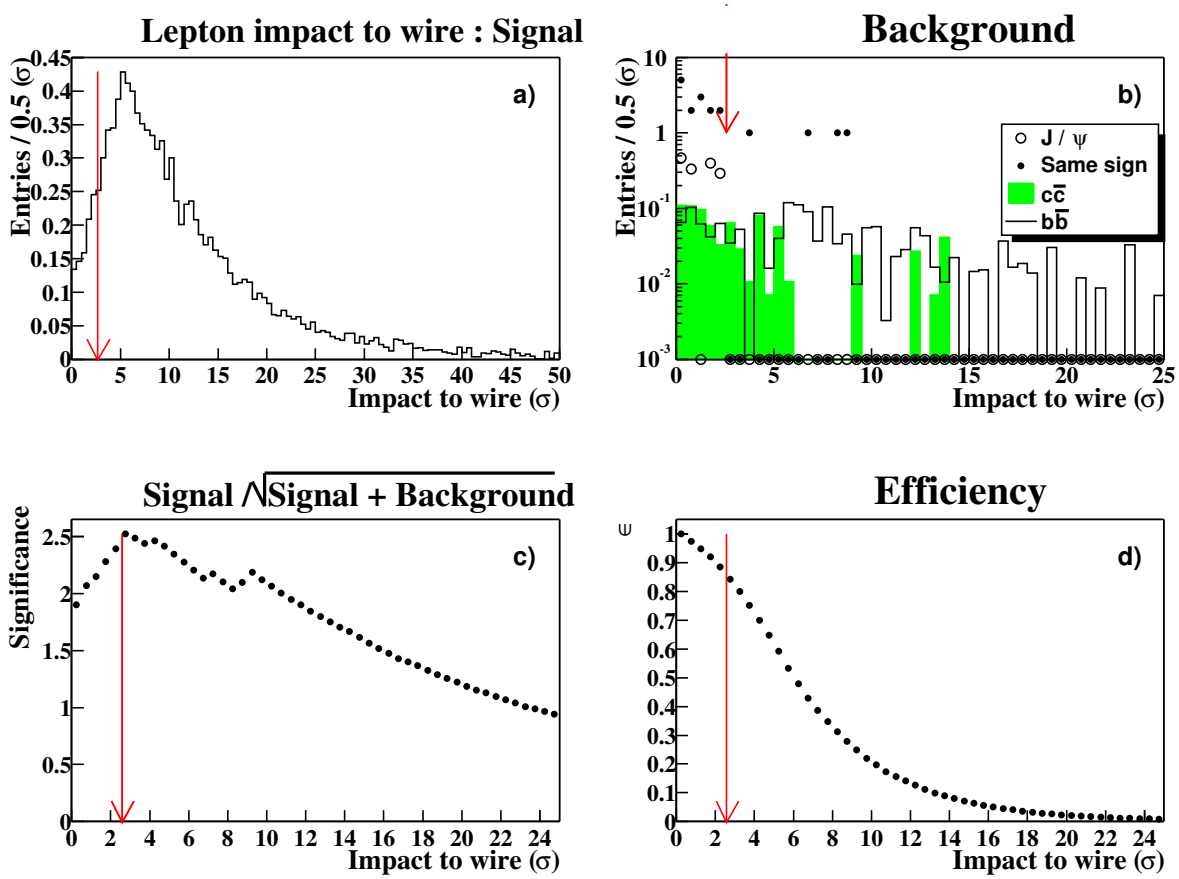

Figure 5.7: Distributions of the single lepton impact to the wire in terms of σ. a) Signal events from MC B $\rightarrow J/\psi$. b) Normalised background events composed of: MC prompt J/ψ, pairs of same sign leptons from data, double semileptonic decays of $c\bar{c}$ MC events, double semileptonic decays of $b\bar{b}$ MC events. c) Significance at each of the value cut on the lepton impact to the wire. d) Efficiency of the signal at each cut value. The arrows indicate the value of the cut applied to this variable.

Cut	Value
Absolute Δz	> 0.2 cm
Δz	$> 9.0\ \sigma$
Lepton impact parameter to wire	$> 2.6\ \sigma$
Lepton CDA to Primary in sigma	$> 0.0\ \sigma$
J/ψ Impact to wire	$< 9\ \sigma$

Table 5.3: Results of the optimisation of the cuts resulting in the maximum significance of the signal of detached J/ψ .

Cut	J/ψ MC	B MC
Acceptance+SLT	3.0	3.1
FLT	50	53
Reconstruction	88	83
J/ψ eff.	1.3 ($\epsilon_P^{J/\psi}$)	1.3 ($\epsilon_B^{J/\psi}$)
Same wire	97	99
Δz sigma	0.01	57
Δz absolute	100	100
J/ψ impact wire	85	96
Lepton impact to wire	0.0	81
Detached J/ψ eff.	0.0	44 ($\epsilon_B^{\Delta z}$)

Table 5.4: Efficiency for each individual cut for I2 wire configuration, for prompt J/ψ and $B \to J/\psi$ events, based on the corresponding MC samples. The values are in % and are determined with respect to the preceding value (in descending order). The corresponding values of $\epsilon_P^{J/\psi}$, $\epsilon_B^{J/\psi}$ and $\epsilon_B^{\Delta z}$ needed for the cross section determination are stated explicitly.

x_F acceptance. With only these events the combined probability that both leptons have hits in the detector and that the SLT accepts the event is calculated ("Acceptance + SLT"). The FLT efficiency is then determined by weighting these events through the FLT efficiency map. The fact that the FLT efficiency is higher for $b\bar{b}$ events than for prompt J/ψ events is possibly due to the presence of semi leptonic decays from the spectator B meson, which occurs in $\approx 10\%$ of the B events. These events produce an additional hard lepton which can give rise to an increase of the trigger probability. The fraction of reconstructed long tracks after the prompt selection cuts represent the reconstruction efficiency. A 5% difference is seen in the reconstruction efficiency, but in this case it is lower for the $b\bar{b}$ sample. Part of this difference may be explained as being due to the compatibility required with an SLT track for the reconstructed tracks. Since b events have a higher possibility to be triggered by an extra lepton and not necessarily by the two J/ψ leptons, the requirement of compatibility of the J/ψ leptons with a trigger track may reduce the reconstruction efficiency, since the event might have been triggered by one of the J/ψ leptons and the extra track and not by the two J/ψ leptons. After the prompt selection is done, a requirement that the primary is reconstructed (after the dilepton subtraction) and that the J/ψ and its associated primary are both associated to the same wire is required (labelled as "Same wire" in the table). We found no prompt J/ψ events surviving the detached selection cuts. This was also the case for all the other samples of different wires and wire configuration. Finally, in Table 5.5 we show $\epsilon_R = (\epsilon_B^{J/\psi}/\epsilon_P^{J/\psi})$ and $\epsilon_B^{\Delta z}$ for every wire in all wire configurations, values that are needed for the $b\bar{b}$ cross section determination Eq. 5.5.

Wire conf.	Wire	ϵ_R	$\epsilon_B^{\Delta z}$
I2	I2	0.99	0.44
B2	B2	1.01	0.37
I1I2	I1	1.03	0.47
	I2	0.96	0.39
I1B1	B1	0.98	0.32
	I1	0.99	0.42
B1O2	B1	1.04	0.35
	O2	1.03	0.35
B1I2	B1	0.97	0.35
	I2	0.97	0.40
B1	B1	0.98	0.35
O2	O2	1.01	0.42
B1B2	B1	0.99	0.36
	B2	1.02	0.32

Table 5.5: Relative $b \to J/\psi \to \mu^+\mu^-$ over $J/\psi \to \mu^+\mu^-$ efficiency ratios ($\epsilon_R = \epsilon_B^{J/\psi}/\epsilon_P^{J/\psi}$) and detachment cuts efficiency for B events ($\epsilon_B^{\Delta z}$) for all wires in all configurations.

5.9 Event counting and characteristics

In Figure 5.8 the dilepton mass distribution after applying the optimised cuts is shown. Not only those events surviving the cut of 0.2 cm and 9 σ downstream of the target wire are shown, which include the signal, but also those with a cut at 0.2 cm and 9 σ upstream from the target. The latter events are in the unphysical region in front of the target and must come from random combinations of tracks. In addition, other background contributions come from double semileptonic decays of $b\bar{b}$ and $c\bar{c}$ events.

In order to obtain the number of b events in the sample, an unbinned likelihood fit is performed on the mass spectrum:

$$L(n_s, n_b) = \left(\frac{(n_s + n_b)^N e^{-(n_s+n_b)}}{N!} \right) \cdot \prod_{i=1}^{N} \left(\frac{n_s P_s(m_i) + n_b P_b(m_i)}{n_s + n_b} \right). \tag{5.15}$$

Here, n_s and n_b are the number of signal and background events, respectively. N is the total number of events and m_i is the mass of the dilepton candidate. An exponential probability function for the background ($P_b(m)$) is assumed, as observed in Figure 5.5. The probability function for the signal ($P_s(m)$) is based on a gaussian distribution For the full statistics fit the parameters are not constrained, only initial values are set to improve the convergence of the fit procedure. With this procedure we find:

$$47.7 \pm 8.7 \;\; b \to J/\psi \;\; events. \tag{5.16}$$

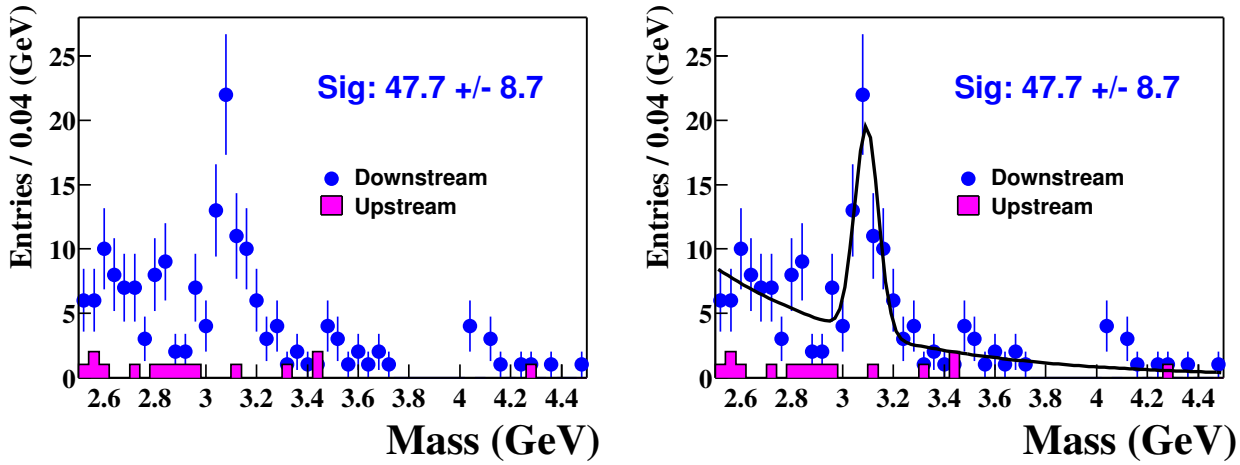

Figure 5.8: Mass spectrum of detached J/ψ . Dots: downstream signal. Histogram: upstream background. Exponential slope = -1.6, mass = 3.095 GeV and width = 0.047 GeV. Both panels show the same data; the right panel includes the fit.

5.10 Sample confirmation

Since we do not fully reconstruct the final state B meson, it is important to test if the J/ψ sample has some of the characteristics of the B particle as, *e.g.*, the long life time. For this the dilepton mass of the selected candidates is plotted against the separation between the J/ψ vertex and the target (Figure 5.9). As expected, one recognises an enhancement at the J/ψ mass region for downstream events, indicative of a delayed production mechanism. At the same time the (unphysical) upstream region is shown, where there is clearly no enhancement at the J/ψ mass region.

5.11 Systematics uncertainties

The two most important contributions to the systematic uncertainties come from the $b \rightarrow J/\psi$X branching ratio, 8.6 %, and from the the reference J/ψ cross section $\sigma_{J/\psi}$, 7.6 % .

Most of the detector and simulation effects cancel when determining the efficiency ratio ϵ_R. Variations in trigger and detector efficiencies show stable results in the cross section determination. A conservative error of 5 % is assumed for ϵ_R.

The distribution of p_T and x_F are not the same for prompt J/ψ and those from b-decays. This introduces a systematic error that does not cancel in the ratio. The systematic error arises from differences in the prediction from generation models of the MC. They are

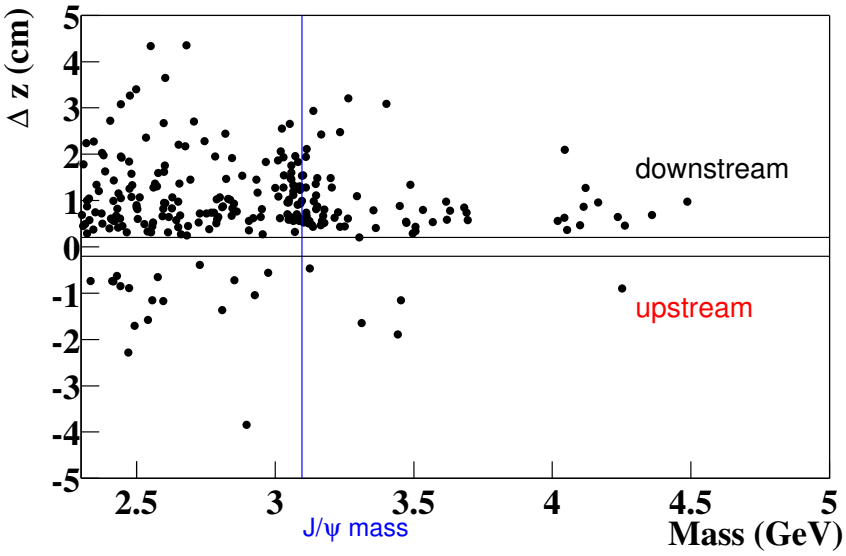

Figure 5.9: Dilepton mass vs z distance to the wire. An enhancement of events is seen at the J/ψ mas region (vertical line), signal of the long life time of these events. In contrast no enhancement is seen in the non-physical upstream region.

estimated as follows:

- $\epsilon_P^{J/\psi}$: As explained in Section 3.2, these distributions are known from experimental data. The effect due to the uncertainties in these distributions is estimated to be 2.5 %.
- $\varepsilon_B^{\rm tot}$: To have a proper distribution from our simulation, the events are weighted with a function depending on the following parameters which all together gives a change in the detection efficiency of 5 %:
  - Parton distribution functions: It was varied from the MRST [17] to the CTEQ5 [16];
  - b quark mass: varied from 4.5 to 5.0 GeV;
  - QCD normalisation scale: varied from 0.5 $\sqrt{m_b^2 + p_T^2}$ to 2 $\sqrt{m_b^2 + p_T^2}$;
  - Intrinsic transverse momenta of the incoming parton: varied from 0.125 to 2.0 GeV;
  - Fragmentation function: Peterson Eq. 1.35 with parameter ϵ from 0.0022 to 0.008, to Kartvelishvili Eq. 1.36 with parameter $\alpha = 13.7$ [29].

The specific efficiency of the detached J/ψ ($\epsilon_B^{\Delta z}$) does not cancel out in the efficiency ratio. The main contributions to the uncertainty come from:

- b lifetime: The average b lifetime, 1.564 ± 0.014 ps [108], is a well determined quantity and contributes less than 1 % uncertainty.
- Vertex resolution: The cut on the displacement of the J/ψ vertex is 5-10 times larger than the vertex resolution, so this contribution is negligible.
- b decay model: The boost of the b particles depends on their energy and also on the production and decay models used. This contribution is already taken into account in $\epsilon_B^{J/\psi}$.
- SLT Target Box: The possible shift of the target box during data taking may produce a loss of detached events. From MC simulation a variation of $\sim$ 1.3 % is seen when modifying the target box position within reasonable ranges. This value is already included in the trigger simulation uncertainty.

The cuts are optimised blindly without looking at the signal over background on data. Inaccuracy of describing the background may bias the value of the cuts. The stability of the signal while modifying the cuts in a reasonable range is studied (see Section 5.13). A variation up to 5 % was observed in the final cross section.

The MC simulation is intended to simulate the behaviour of data taking during different periods. Short terms variations of the behaviour of the detector or data taking conditions are difficult to simulate properly. These variation occurs in the interaction rate which affect the event multiplicity leading to a variation of 1% in the efficiency. Beam sharing between wires, beam shape and position variations influence the efficiencies on 0.5 %.

In Table 5.6 we summarise the contribution of each quantity to the systematic error. Since they are (almost) independent we sum them in quadrature. The final systematic uncertainty for $\sigma(b\bar{b})/\sigma_{J/\psi}$ is 13 % and 15% for $\sigma(b\bar{b})$ where the prompt J/ψ cross section is included.

5.12 Cross section determination

With the values determined in the previous sections, we obtain the following cross section within the acceptance of HERA – B :

$$\Delta\sigma(b\bar{b}) = 8.5 \pm 1.6_{stat} \pm 1.2_{sys} \text{ nb/nucleon.} \tag{5.17}$$

As estimated from theoretical models, 90.6% of all J/ψ from B decays are within the HERA – B x_F range, which implies a total cross section of

$$\sigma(b\bar{b}) = 9.4 \pm 1.7_{stat} \pm 1.3_{sys} \text{ nb/nucleon.} \tag{5.18}$$

The cross section ratios are:

Systematic source	Relative systematic uncertainty in $\sigma(b\bar{b})$
J/ψ cross section ($\sigma_{J/\psi}$)	7.6 %
b to J/ψ branching ratio (Br($b\bar{b} \to J/\psi\ X$))	8.6 %
Trigger simulation (ε_R)	5 %
b production and decay model ($\varepsilon_B^{\rm tot}$)	5 %
Prompt J/ψ MC production models ($\varepsilon_P^{J/\psi}$)	2.5 %
b lifetime error ($\varepsilon_B^{\Delta z}$)	<1%
MC event multiplicity	1 %
Beam sharing between wires	0.5 %
Cuts	5 %
Total contribution to $\sigma(b\bar{b})/\sigma_{J/\psi}$	13 %
Total contribution to $\sigma(b\bar{b})$	15 %

Table 5.6: Systematic uncertainties for $\sigma(b\bar{b})$ in the muon channel, reported here. The dominant contributions are due to the reference measurements of Br($b\bar{b} \to J/\psi\ X$) and the prompt J/ψ cross section.

$$\Delta R_\sigma = \frac{\Delta\sigma_B}{\Delta\sigma_P} = 0.031 \pm 0.006_{stat} \pm 0.004_{sys} \tag{5.19}$$

and

$$R_\sigma = 0.027 \pm 0.005_{stat} \pm 0.004_{sys}. \tag{5.20}$$

5.13 Stability studies

In this section we study the stability of the signal while modifying the selection criteria. For each of the cuts under study all the other cuts are set to the optimised values. Figure 5.10 shows the variation of the $b\bar{b}$ cross section in the HERA – B acceptance under the variation of the cuts on the J/ψ and lepton impact parameter to the wire, lepton CDA to the primary and Δz between the J/ψ vertex and the target wire. The largest variation (defined as (maximum - minimum)/$\sqrt{12}$) occurs on the lepton impact to wire distribution, but the first two bins in the plot suffer from prompt J/ψ contamination, which is not subtracted in this analysis.

From this study we conclude that the variations are of the order of 5 % within reasonable variation of the cut values, which shows the good stability of our cross section determination.

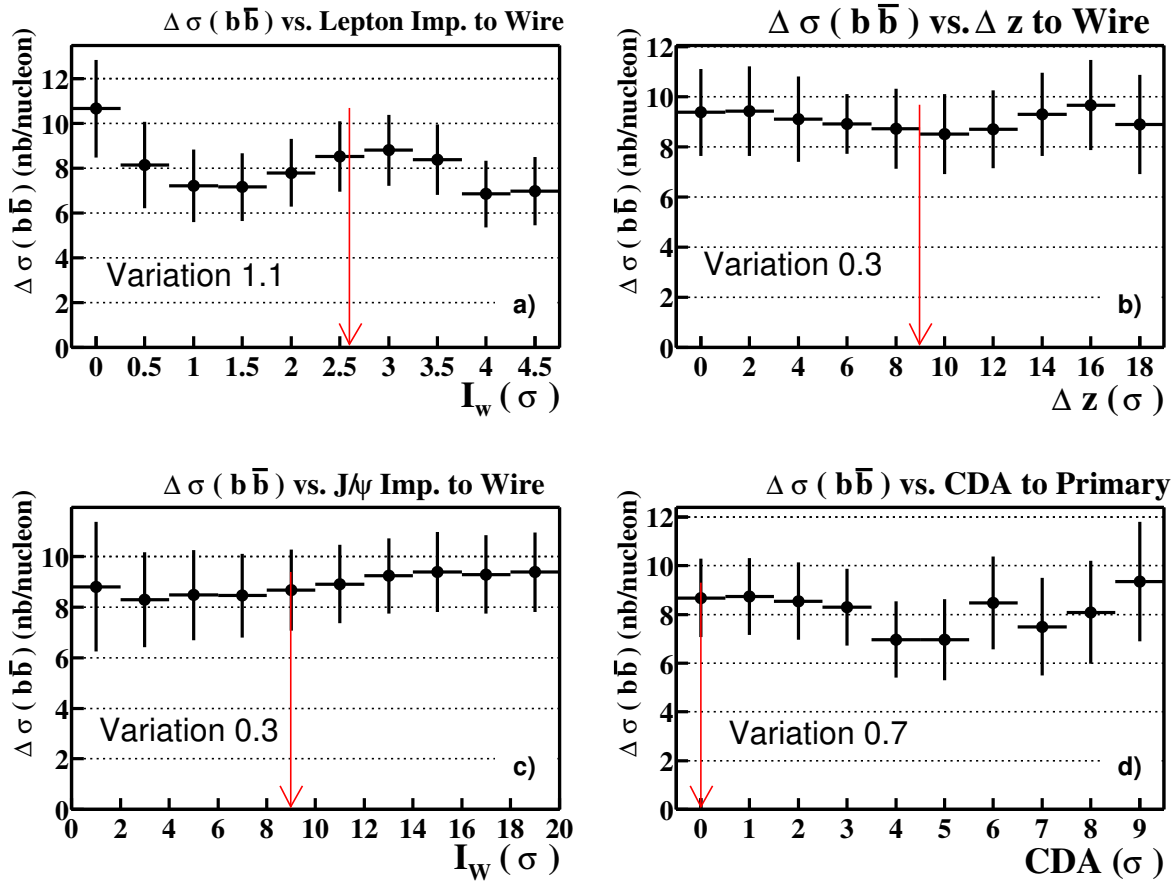

Figure 5.10: Cross section stability plots. The $b\bar{b}$ corssection in HERA – B acceptance is determined for different cut values. The cut on the variable under study is modified while the rest of the cuts are set to their optimised values. The variation is defined as (maximum - minimum)/$\sqrt{12}$. The prompt J/ψ contamination is not subtracted from the number of detached J/ψ so that in the cases of the lepton impact to wire and Δ z the first bins present an overestimated cross section.

5.14 Studies on different materials

Since the statistics allows it, we calculate the cross section ratio and the $b\bar{b}$ cross section for each target material separately. The invariant mass plot for the detached events is shown in Fig. 5.11. The final result is summarised in Table 5.7. As can be seen the values are consistent with each other within the errors. This result is thus a confirmation of the assumption that there is no material dependence in the $b\bar{b}$ cross section.

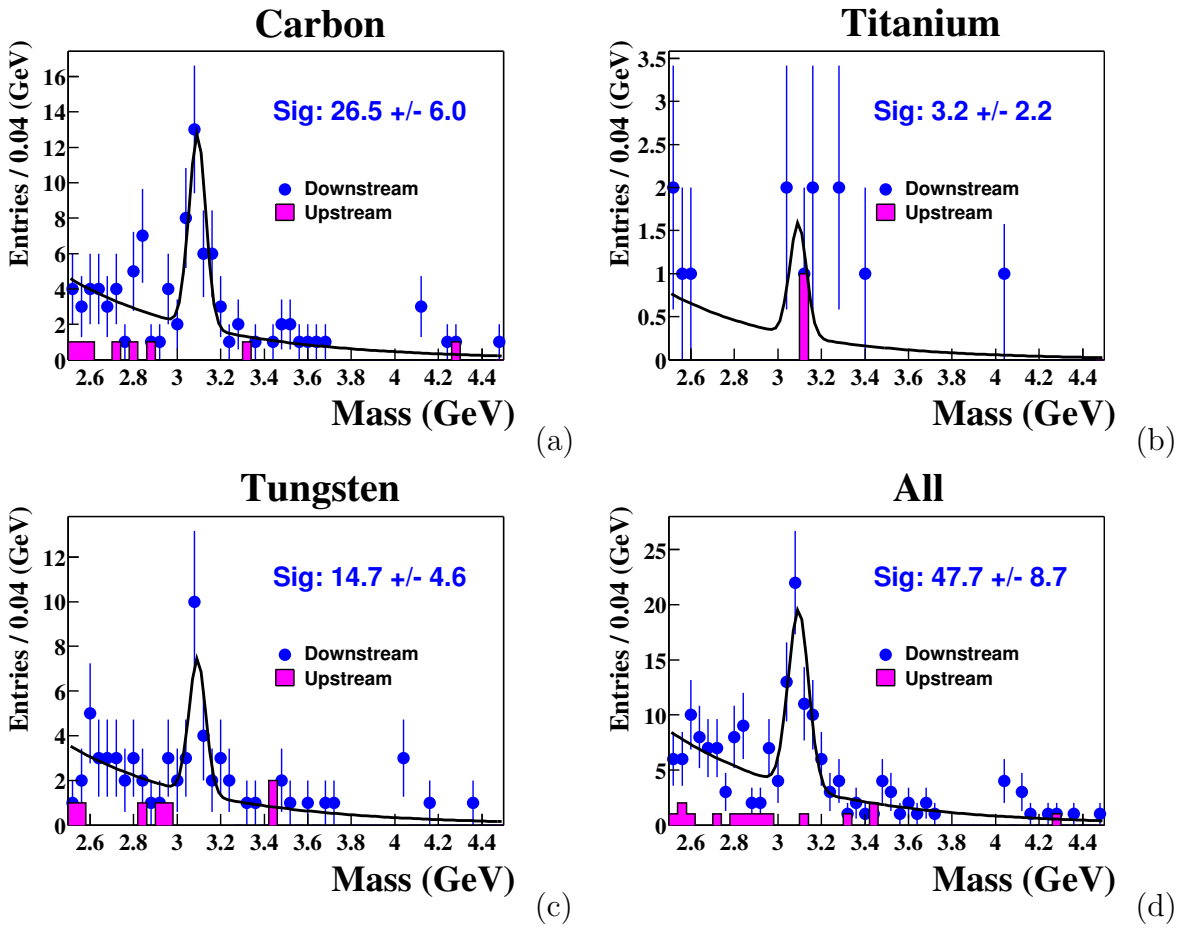

Figure 5.11: Invariant mass distribution of the detached candidates, for the different materials. a) Carbon ; b) Titanium ; c) Tungsten ; d) All.

5.15 Outlook and discussion

HERA – B has also the possibility of measuring the J/ψ decay in the electron channel, which involves partially different detector components in the analysis together with a different background composition. The combination of both analyses provide a cross check of the result. The $b\bar{b}$ cross section within the HERA – B acceptance measured in

Material	A	# J/ψ	# B	$\Delta\sigma(b\bar{b})/\Delta\sigma_{J/\psi}$ 10^{-2}	$\Delta\sigma(b\bar{b})$ nb/nucleon
Carbon	12	94244 ± 355	26.5 ± 6.0	$2.9 \pm 0.7_{stat}$	$7.8 \pm 1.8_{stat}$
Titanium	48	8245 ± 108	3.2 ± 2.2	$4.1 \pm 2.9_{stat}$	$11.1 \pm 7.7_{stat}$
Tungsten	184	47050 ± 264	14.7 ± 4.6	$2.8 \pm 0.9_{stat}$	$7.7 \pm 2.4_{stat}$
Total	-	147982 ± 453	47.7 ± 8.8	$3.1 \pm 0.6_{stat}$	$8.5 \pm 1.6_{stat}$

Table 5.7: Results for the different target wire materials.

the electron channel [80] based on 103800 ± 1000 prompt J/ψ and 36.9 ± 8.1 $b \to J/\psi$ events, is :

$$\Delta\sigma(b\bar{b}) = 9.8 \pm 2.1_{stat} \text{ nb/nucleon}, \tag{5.21}$$

a result which is compatible with the one in the muon channel.

The "official" HERA – B value [80] for the total cross section based on the combined electron and muon analysis [2]:

$$R_\sigma = \frac{\sigma(b\bar{b})}{\sigma(J/\psi)} = 0.027 \pm 0.004_{stat} \pm 0.004_{sys}, \tag{5.22}$$

$$\sigma(b\bar{b}) = 9.6 \pm 1.5_{stat} \pm 1.4_{sys} \text{ nb/nucleon}. \tag{5.23}$$

The main systematic uncertainty in the cross section ratio comes from the Br ($b \to J/\psi$ X) (8.6%), that equals the sum of all the other contributions. In the total cross section the prompt J/ψ production uncertainty also contributes substantially to the total systematic error.

Figure 5.12 shows the comparison with theoretical calculations ([22] and [21]) and with the previous measurements.

The new HERA – B result is more than one σ below the previous one of HERA – B , extracted from the data taken in 2000 which was published in 2002. It was determined by a similar technique and with the same J/ψ normalisation, but suffers from lower statistics (10 events) compared to the present combined result based on 83 events. The new result is closer to the lower bound of the theoretical predictions, and seems to be in better agreement with E789 [24] than with E771 [26], as shown in Table 5.8.

[2]The published cross section based on the muon decay channel ($\Delta\sigma(b\bar{b}) = 8.2 \pm 1.5_{stat}$nb/nucleon), differs slightly from the one presented in this thesis, due to different fit functions applied in slightly different mass ranges, and due to a difference in the selection where only one dilepton pair is allowed per event based on the best muon likelihood of the pair. In the analysis presented here the presence of more than one dilepton pair per event is allowed. There is a small difference in the total number of processed events.

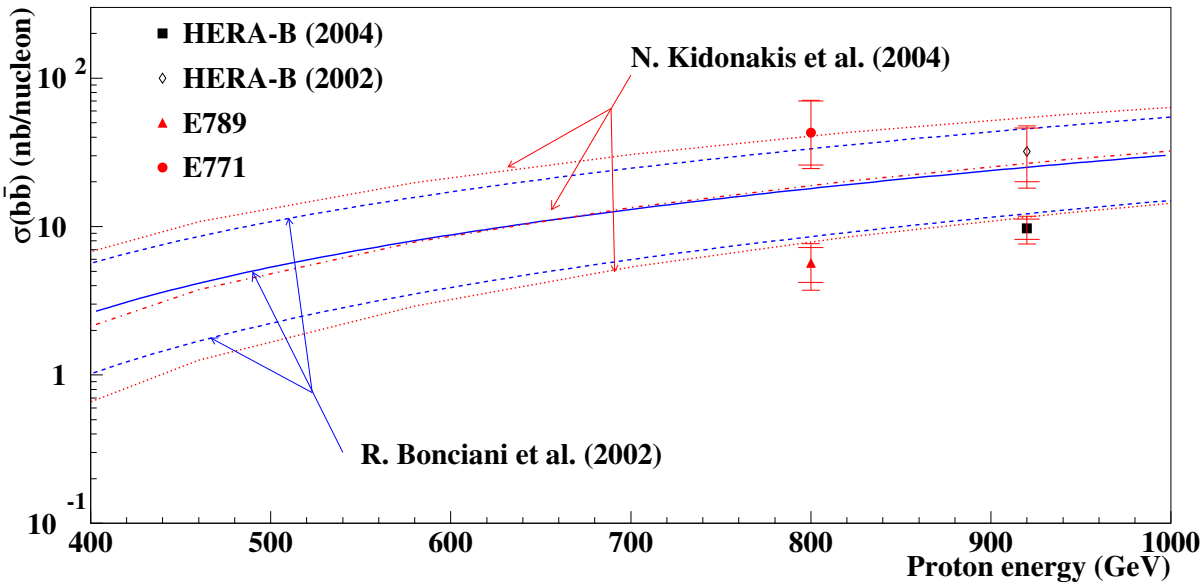

Figure 5.12: Comparison with other experiments and theoretical predictions. The new HERA – B result is the average of the electron and muons decay channels measurements. HERA – B (2004) refers to this analysis based on data taken in 2002-2003; HERA – B (2002) is the previous publication, of the year 2002, based on data of the year 2000.

The HERA – B measurements in 2000 and 2002-2003 were performed with a similar technique and with the same experimental apparatus, thus they can be combined in a final result which yields a cross section ratio of the $b\bar{b}$ and J/ψ production of $R_\sigma = 0.028 \pm 0.004_{stat} \pm 0.004_{sys}$. This implies $\sigma(b\bar{b}) = 9.9 \pm 1.5_{stat} \pm 1.4_{sys}$ nb/nucleon. These values are obtained with the largest data sample for $b \to J/\psi$ events (93), and should thus represent the most accurate data at present, as shown in Table 5.8 which summarises the present experimental situation.

			p	Events	$\sigma(bb)$	$\sigma(bb)$	
Exper.	Year	Target	GeV		(nb/nucleon)	@ 920 GeV	Ref.
E789	1995	Au	800	19	$5.7 \pm 1.5 \pm 1.3$	$8.1 \pm 2.2 \pm 1.8$	[24]
E771	1999	Si	800	15	$43^{+27}_{-17} \pm 7$	$61^{+38}_{-24} \pm 10$	[26]
HERA – B	2002	C/Ti	920	10	$32^{+14\ +6}_{-12\ -7}$	$32^{+14\ +6}_{-12\ -7}$	[25]
HERA – B	2004	C/Ti/W	920	83	$9.6 \pm 1.5 \pm 1.4$	$9.6 \pm 1.5 \pm 1.4$	[80]
HERA – B	2002/4	C/Ti/W	920	93	$9.9 \pm 1.5 \pm 1.4$	$9.9 \pm 1.5 \pm 1.4$	[80]

Table 5.8: Present experimental situation, with previous and new HERA – B measurement, all compared at HERA – B proton beam energy (920 GeV)

Finally we add one note of caution: The obtained cross section ratio is almost independent of any other measurement, and depends mainly on quantities obtained from the HERA – B measurement itself. This is different for the deduced value of the cross section,

which depend on the literature value of the J/ψ cross section. Updated values of the J/ψ cross section will affect our measurement of the $b\bar{b}$ cross section, which must be then also updated accordingly.

Chapter 6

Exclusive B search

In this section we identify completely reconstructed B decays. After an estimate of the expected number of events, the results for the two most promising channels are presented. These are:

- $B^+ \rightarrow J/\psi\ K^+$;
- $B^0 \rightarrow J/\psi\ K^+\ \pi^-$.

They are characterised by relatively large branching ratios and a low number of final state particles needed for the full reconstruction. We present detailed results for the sub-channel $J/\psi \rightarrow \mu^+\mu^-$ and summarise only the results for the electron channel.

6.1 Event selection

The selection of an exclusive decay proceeds in several steps. First, the standard selection for prompt dilepton candidates is applied as described in Section 5.2. However, in contrast to the determination of the $b\overline{b}$ cross section, which relies crucially on the displacement between the primary vertex and the B decay vertex which gives rise to the production of the J/ψ , we aim to reduce the cut on the distance between the primary vertex and the J/ψ vertex at a first step in the search. We require that the dileptons have an invariant mass between 2.9 and 3.3 GeV in order to eliminate the non-J/ψ events. After this, a search for additional tracks is performed, aiming to select a kaon candidate. Since most of the particles in a proton hadron collisions are pions and only 10% are kaons [110], our selection must aim at separating the kaons from the pion background. In the first selection, however, we do not yet stress this point, but require a good quality track:

- VDS hits ≥ 5;
- Hits in the main tracker ≥ 10;

- Probability $\chi^2 \geq 0.3$ %;
- $p_T \geq 0.5$ GeV.

As mentioned before, we do not yet require that the kaon track candidate must be positively identified by the RICH counter as a kaon track since we aim to modify the kaon selection together with the displacement of the B candidate to test different scenarios to look for exclusive decays. In the case of the $B^0 \rightarrow J/\psi\, K^+\, \pi^-$ channel a search of a fourth track with pion characteristics is done with the same criteria as above, and, in addition, this track must have a combined (pion + electron + muon likelihood) larger than 0.05. Since the p_T distribution for pions peaks at a smaller values than the one for kaons, we cannot use a cut on the pion p_T as a preliminary selection. Rather, we require (in order to eliminate kaons and protons) the combined RICH likelihood for pions, muons and electrons to be larger than 0.05. Since the electron-pion separation is only clear for low momentum particles (Figure 2.10) a combined likelihood is applied to allow higher momentum particles to be selected. An upper cut on the kaon likely hood is applied since there are no pions with a kaon likelihood bigger than 0.35 [67]. The pion selection is:

- VDS hits ≥ 5;
- Hits in the main tracker ≥ 10;
- Probability $\chi^2 \geq 0.3$ %;
- (pion + electron + muon) likelihood ≥ 0.05;
- Kaon likelihood ≤ 0.35.

If a third (and possibly a fourth) track is found, a three (four) particle fit is performed with a constraint that the two leptons combine to the J/ψ mass. This latter constraint improves the mass and the vertex resolution, allowing the vertex routine (GROVER [89]) to modify the slopes and momentum of each of the lepton tracks within their errors, to match the mass constraint. Candidates with a vertex probability greater than 1 % are selected for further analysis. For the $B^0 \rightarrow J/\psi\, K^+\, \pi^-$ search, only events for which the invariant mass of the kaon and pion lies between 0.77 and 1.02 GeV are allowed, since this decay proceeds (predominantly) through K^* resonance at 0.892 GeV.

6.2 Expected number of events

The production ratios of b particles, are given by the PDG as follows:

- PR(B^+) = (39.7 $\pm$1.0) %

- PR(B^0) = (39.7 ±1.0) %
- PR(B_s^0) = (10.7 ±1.1) %
- PR(b-baryons) = (9.9 ±1.7) %

For the $B^+ \to J/\psi\, K^+$ channel, the branching ratio ($(1.00 \pm 0.04) \times 10^{-3}$) [108], represents 8.6 % of the total inclusive branching ratio (Br($b \to J/\psi X$) = 1.16 %) [108]. In order to estimate the number of events which can be completely reconstructed, we start with the 47.7 b hadron events measured in the inclusive $B \to J/\psi + X \to \mu\mu$ channel (see Sect. 5.9). The selection efficiency for this sample with respect to the prompt J/ψ selection (*i.e.* the cut on the vertex displacement) was determined to be 38.8%, implying a total number of 123 b events with a reconstructed J/ψ before the detachment cut is applied. Table 6.1 shows the expected number of events in the $B^+ \to J/\psi\, K^+$ channel starting from a total of 123 reconstructed $b \to J/\psi$ events in the collected data sample. The quoted acceptances for the kaon and the reconstruction efficiencies are obtained through Monte Carlo simulations. The final result is that we should expect ~ 2 fully reconstructed decays $B^+ \to J/\psi\, K^+$, or an upper limit of 5 at 90 % confidence level , without yet applying any detached selection.

	%	Events
$B \to J/\psi$ (J/ψ reconstructed)	100	123
PR $B^+ \to J/\psi$ X	39.7	48.8
$B^+ \to J/\psi\, K^+$	8.6	4.2
Kaon inside the detector	70.5	3.0
Kaon and vertex reconstruction	62.1	1.8
Total	**1.5**	**1.8**

Table 6.1: Expected number of $B^+ \to J/\psi\, K^+$ events before the cuts on vertex detachment and kaon likelihood. Branching ratios are taken from PDG [108]. The kaon reconstruction efficiency is estimated from MC studies.

For the $B^0 \to J/\psi\, K^+\, \pi^-$ channel the branching ratio is 1.2 ± 10^{-3}. Table 6.2 shows the expected number of events in the $B^0 \to J/\psi\, K^+\, \pi^-$ channel starting again from a total of 123 reconstructed $b \to J/\psi$ events in the collected data sample. The quoted acceptances for the kaon and the reconstruction efficiencies are obtained through Monte Carlo simulations. One expects about 1 fully reconstructed decay $B^0 \to J/\psi\, K^+\, \pi^-$. This corresponds of an upper limit of 4 events at 90 % confidence level.

6.3 Event characteristics from MC studies

The MC sample used is the same as the one used in the inclusive analysis. Fig. 6.1 shows the mass resolution for both decays. The mass resolution is 22 MeV for $B^+ \to J/\psi\, K^+$

	%	Events
$B \to J/\psi$ (J/ψ reconstructed)	100	123
$B^0 \to J/\psi$ X	39.7	48.8
$B^0 \to J/\psi\ K^+\ \pi^-$	10.4	5.1
Kaon inside the detector	70.9	3.6
Pion inside the detector	76.4	2.8
Kaon, pion and vertex reconstruction	27.1	0.8
Total	**0.6**	**0.8**

Table 6.2: Expected number of $B^0 \to J/\psi\ K^+\ \pi^-$ events before the cuts on vertex detachment and kaon likelihood. Branching ratios are taken from PDG [108]. The kaon reconstruction efficiency is estimated from MC studies.

and 27 MeV for $B^0 \to J/\psi\ K^+\ \pi^-$. Such good values are achieved by fixing the invariant mass of the two leptons to the nominal J/ψ mass.

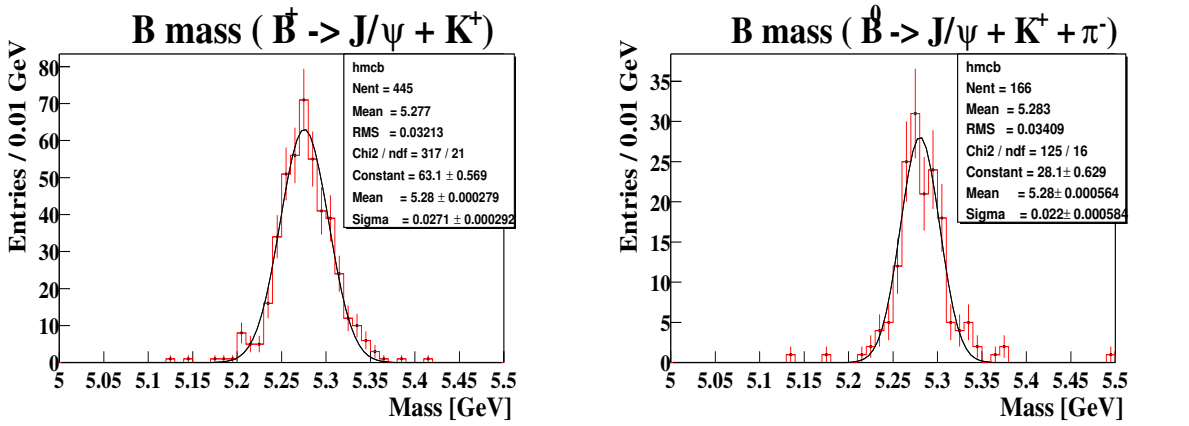

(a) (b)

Figure 6.1: Monte Carlo studies. The left figure shows the invariant mass for $B^+ \to J/\psi\ K^+$ and the right one for $B^0 \to J/\psi\ K^+\ \pi^-$.

Figures 6.2 and 6.3 show the distributions of some relevant variables – p_T, RICH likelihood, impact parameter to the J/ψ vertex, kaon impact to the wire, and reconstructed B-impact to wire – which allow to identify a B decay candidate. In the same figures the combinatorial background for prompt events of data are shown as a reference of the behaviour of background events.

6.4 Identification of B meson decays

Due to the low number of expected events, the aim of this study is not to determine a cross section but simply to positively identify in our data sample events with strong B

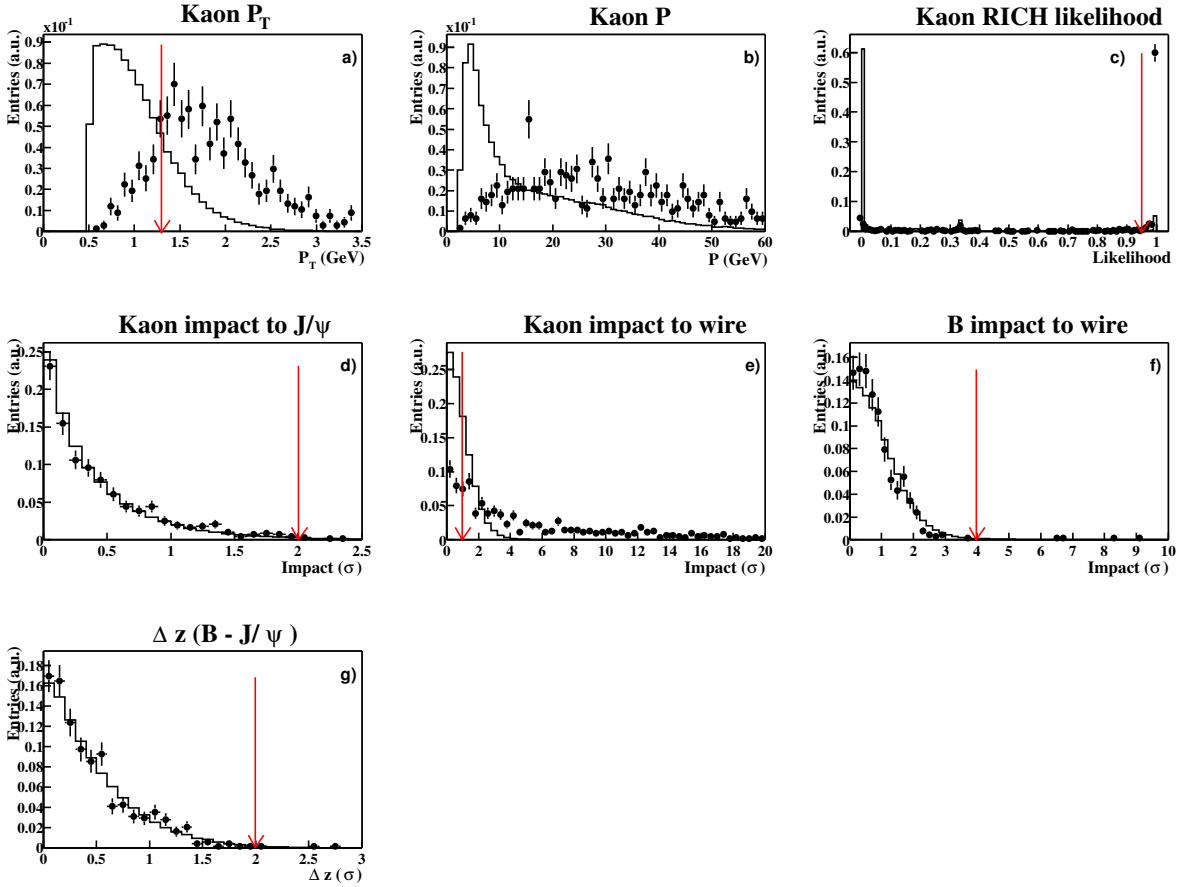

Figure 6.2: Distribution of the reconstructed $B^+ \rightarrow J/\psi\ K^+$ characteristics of the MC truth events (dots with error bars). The histograms show the behaviour of the prompt background from real data, selected as described in text, without detaching cuts. Arrows show the selection cuts applied as described in the next section (6.4).

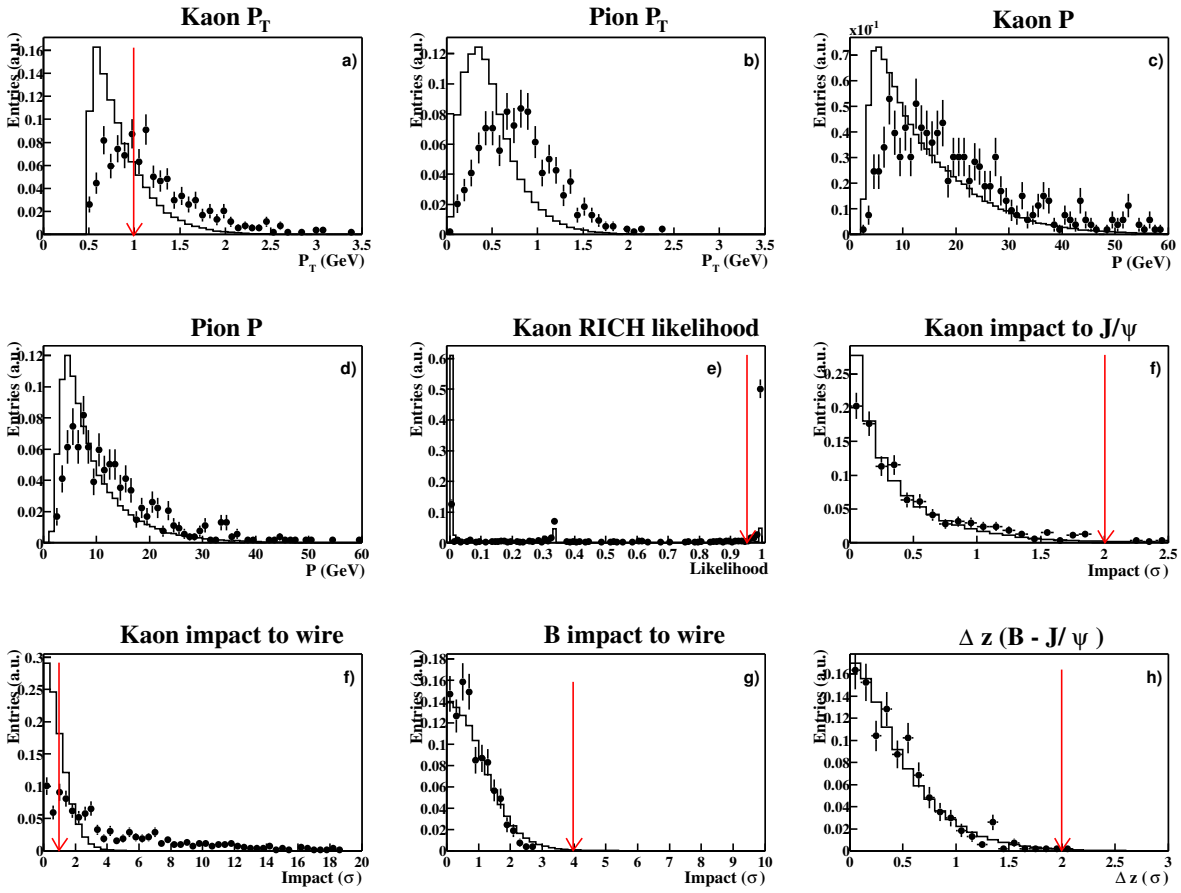

Figure 6.3: Distribution of the reconstructed $B^0 \rightarrow J/\psi\ K^+\ \pi^-$ characteristics of the MC truth events (dots with error bars). The histograms show the behaviour of the prompt background from real data, selected as described in text, without detachment cuts. Arrows show the selection cuts applied as described in section (6.4).

characteristics with low background contamination. For this reason the cuts are not determined blindly, but through an analysis of potentially good candidates and background events. The following cuts are then applied to discriminate between signal events and background:

- Kaon impact to wire $> 1\ \sigma$: Since the B meson vertex is separated from the primary vertex one expects that the B decay products do not point back to the the primary vertex.
- Kaon impact to $J/\psi < 2\ \sigma$: The kaon and the J/ψ are produced at the same space point.
- B impact to target $< 4\ \sigma$: b hadrons are produced in the primary interaction.
- Δz (B - J/ψ)$< 2\ \sigma$: The B vertex should be at the same position as the J/ψ vertex.
- Kaon p_T : Kaons originating in a B decay have a high transverse momentum. This cut is varied together with the detached cuts so as to test different secenarios. A cut with a p_T greater than 1.3 GeV is the maximum cut tested.
- Kaon likelihood: The kaon RICH likelihood will be fixed to three different values, the maximum value being larger than 0.95 as the strongest cut.

The requirement of an additional particle allows us to apply different less stringent cuts for the vertex detachment than the ones which have been used in the previous section, when we derived the $b\bar{b}$ production cross section from detached J/ψ vertex. This may increase the probability to find a fully reconstruced event. At this stage of the analysis, the kaon identification cuts are not yet fixed; rather, they are varied simultaneously with the cuts on the separation between primary and dilepton vertex in order to investigate the signal-to-background ratio.

6.5 Mass spectrum and individual events

We test in this section different scenarios to search for exclusive events, going from the standard requirements on the vertex detachment combined with minimum quality cuts on the kaon track, towards scenarios with loose cuts on the vertex displacement, but simultaneously strong requirements on the kaon identification. These different scenarios can be described as follows (the values in parenthesis refer to the $B^0 \rightarrow J/\psi\ K^+\ \pi^-$ channel):

- Cuts on the vertex detachment:
  - Hard, using the values found in section 5.8;
  - Soft: 1/2 of the optimised values;

– Minimal: 1/4 of the optimised values;

- Kaon cuts:
  - Hard: $p_T > 1.3$ (1.0) GeV and likelihood > 0.95;
  - Soft: $p_T > 0.65$ (0.5) GeV and likelihood > 0.35;
  - Minimal: $p_T > 1.3$ (1.0) GeV and no likelihood requirement.

The kaons in the $B^0 \to J/\psi\ K^+\ \pi^-$ channels present lower transverse momentum (Fig. 6.3), so that we relax the requirement. The results of four of the nine possible combinations of these cuts are shown in Figure 6.4 for the decay $B^+ \to J/\psi\ K^+$ and in Figure 6.5 for the case $B^0 \to J/\psi\ K^+\ \pi^-$.

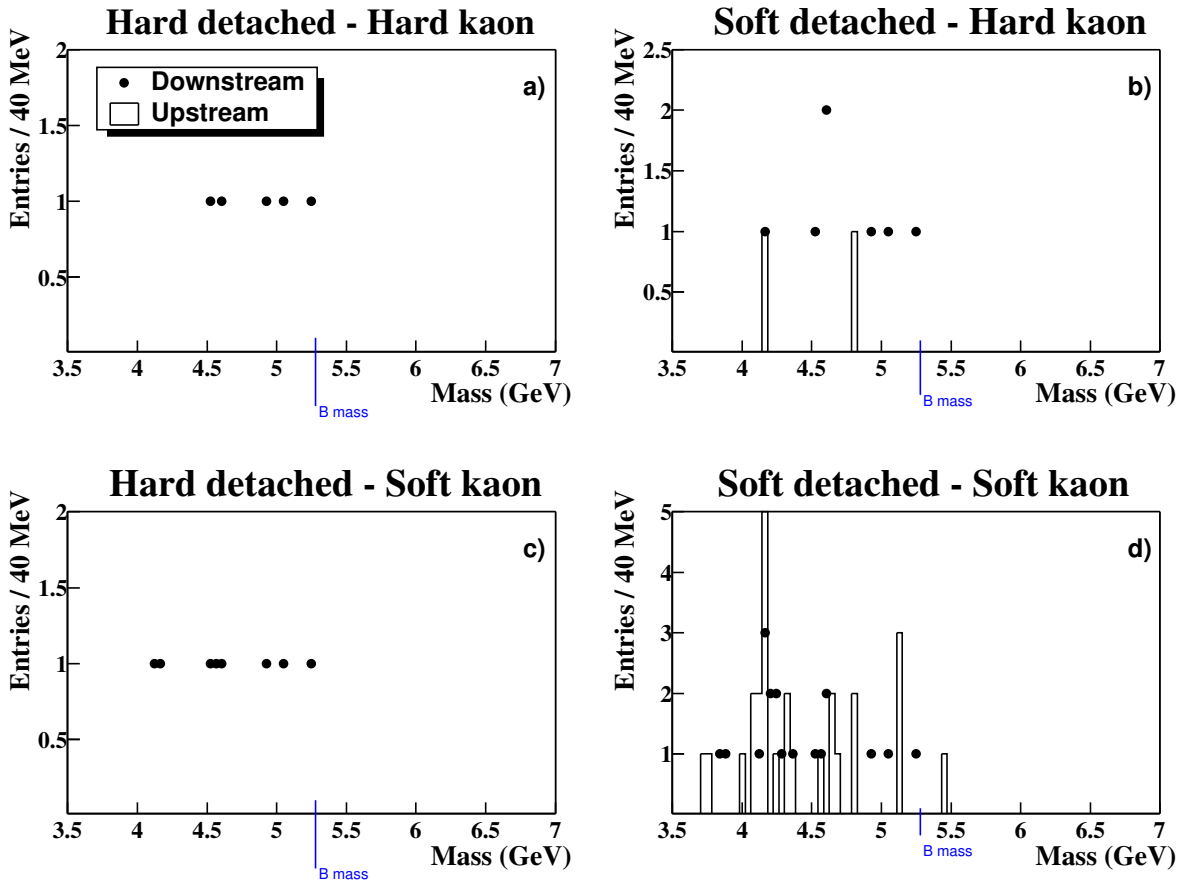

Figure 6.4: The invariant mass of a J/ψ + kaon under different requirements of kaon identification and the detachment from the primary interaction as described in the text. Dots: Downstream (signal) events . Histograms: Upstream (background) events.

As can be seen there is no clear signal at the B-mass of 5.3 GeV, in agreement with the estimate made in Table 6.1. The plots corresponding to the "soft" conditions are evidently

background dominated showing that one must stay clear of the primary interaction. In the vicinity of the primary vertex, prompt dilepton candidates have a high probability to form a good vertex together with an extra particle, leading to a rapid increase of the background. In these softer scenarios the upstream non physical events give a good estimate of the background. In the distributions obtained with the more stringent "Hard" conditions on the detachment, one notices the absence of upstream events, as well as the fact that there are no events at mass values beyond the B mass. This might indicate that there is no background, but that the events in the continuum at masses below the B-mass are incompletely reconstructed events, where one or more particles are missing. From the branching ratios of other B decays into a J/ψ and a kaon, it is possible to determine that the $B^+ \to J/\psi\, K^+$ channel represents 20 % of the $B^+ \to J/\psi\, K^+$ X decays. Assuming similar efficiencies we can expect 4-5 B events with masses lower than the B mass for each signal events found. This is compatible with the number of events seen in Figure 6.4.

A closer look at the event in the B mass region reveals strong B characteristics; this event with the number 373074 of run 20639 is shown in Table 6.4. Starting from a correct mass, this event also has a strong detachment from the primary interaction, together with large impact parameters of both leptons. The kaon candidate shows optimal RICH likelihood and high transverse momentum. As expected the B vertex is compatible with the J/ψ vertex and the kaon candidate is also pointing to the J/ψ vertex and away from the primary interaction. Finally the B vertex has a good probability χ^2.

As previously, also for the case of $B^0 \to J/\psi\, K^+\, \pi^-$ the three kaon conditions and three detachment conditions have been combined, whereas we kept constant the definition of the additional π, which is already a fairly weak one. This is favourable since it helps to avoid that the efficiency is still further reduced due to additional requirements, whereas on the other hand, the requirement of an additional particle helps to suppress background. Figure 6.5 shows the invariant mass distributions for four of the nine different scenarios thus tested.

As before, the "Soft" requirements leads to background domination. Similarly, if a "Hard" condition for the vertex detachment is chosen (left panels), there are no events left with a mass exceeding the B-mass of 5.3 GeV. There are a few events with a reconstructed mass below the B mass, which might indicate again b events with additional unreconstructed extra particles. In this channel we expect a relation of 3-4 B events bellow the B mass value for each signal event (since the $B^0 \to J/\psi\, K^+\, \pi^-$ decay represent 30 % of the total $B^0 \to J/\psi\, K^+\, \pi^-$ X decays). A detailed inspection of the event in the B mass region shows good B characteristics. Table 6.4 shows the characteristics of this event. The reconstructed masses of the B and J/ψ agree well with the PDG values, and also the other characteristics - such as vertex detachment and impact parameters or kaon identification - seem to support an interpretation as genuine B-decay.

Finally, Table 6.3 shows the efficiency of the B selection and the expected number of events for the different scenarios for the different channels.

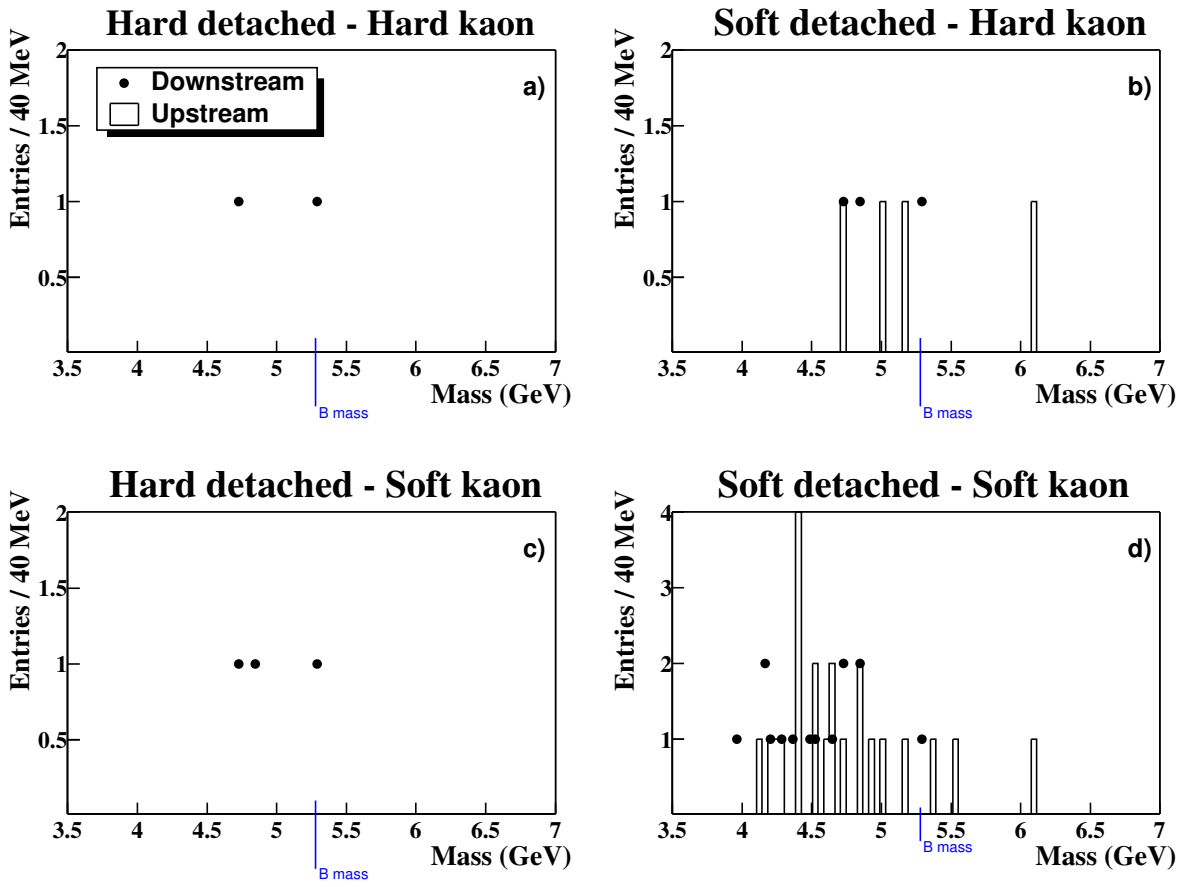

Figure 6.5: The invariant mass of J/ψ + kaon + π originating from a $B^0 \to J/\psi\ K^+\ \pi^-$ decay under different requirements on kaon identification and the detachment from the primary interaction as described on the text. Dots: Downstream events . Histograms: Upstream background events.

Selection	$B^+ \to J/\psi\ K^+$		$B^0 \to J/\psi\ K^+\ \pi^-$	
	Eff. (%)	Nr. B	Eff. (%)	Nr. B
Hard-Hard	19	0.34	13	0.10
Hard-Soft	26	0.47	22	0.18
Hard-Min	32	0.58	15	0.12
Soft-Hard	31	0.56	24	0.19
Soft-Soft	42	0.76	39	0.31
Soft-Min	50	0.90	28	0.22
Min-Hard	39	0.70	29	0.23
Min-Soft	53	0.95	48	0.39
Min-Min	65	1.2	33	0.27

Table 6.3: Efficiencies and expected number of events for each scenario for each decay channel.

Candidate	a - $B^+ \to J/\psi\, K^+$	b - $B^+ \to J/\psi\, K^+$	c - $B^0 \to J/\psi\, K^+\, \pi^-$
Run Number	20639	20967	20229
Event Number	373074	33045	2396199
Wire Configuration	I1I2	B1O2	B1I1
Primary X (cm)	0.26	0.35	0.34
Primary Y (cm)	-0.12	-0.16	-0.03
Primary Z (cm)	-4.47	-1.13	-0.57
B Mass (GeV)	5.261	5.309	5.277
B Vertex Prob χ^2	0.32	0.1304	0.54
Δz (B - Wire) (cm)	0.31	0.92	1.11
δz (B - Wire) (σ)	12.2	36.0	39.4
B impact to Wire (σ)	2.07	1.12	0.17
δz (B - J/ψ) (cm)	-0.046	-0.065	0.010
δz (B - J/ψ) (σ)	-1.10	-1.54	0.20
J/ψ mass (GeV)	3.073	3.128	3.079
J/ψ Vertex Prob. χ^2	0.22	0.28	0.05
δz (J/ψ- Wire) (cm)	0.36	0.98	1.10
δz (J/ψ- Wire) (σ)	9.2	25.1	26.6
J/ψ impact to wire (σ)	3.60	5.19	1.73
$K + \pi$ inv. mass (GeV)	-	-	0.890

	a - $B^+ \to J/\psi\, K^+$			b - $B^+ \to J/\psi\, K^+$			c - $B^0 \to J/\psi\, K^+\, \pi^-$			
	μ^-	μ^+	K^+	e^-	e^+	K^+	μ^-	μ^+	K^+	π^-
RTRA Index	1	2	3	1	2	9	1	2	15	5
P (GeV)	22.2	20.3	27.4	33.9	25.5	13.7	15.8	28.8	28.2	9.5
P_T (GeV)	1.92	2.23	2.0	2.3	1.4	1.4	1.7	1.2	1.5	0.7
Hits in VDS	12	11	11	11	15	10	9	9	15	9
Hits in OTR	38	41	39	44	43	33	39	36	35	40
Hits in MUONS	17	19	-	-	-	-	18	18	-	-
$\mathcal{L}_\mu^{MUON}$	0.98	1	-	-	-	-	1	0.98	-	-
$\mathcal{L}_\mu^{RICH}$	-	-	0.0	-	-	0.0	-	-	0.0	0.71
$\mathcal{L}_K^{RICH}$	-	-	1.0	-	-	1.0	-	-	1.0	0.0
$\mathcal{L}_e^{RICH}$	-	-	0.0	-	-	0.0	-	-	0.0	0.09
$\mathcal{L}_\pi^{RICH}$	-	-	0.0	-	-	0.0	-	-	0.0	0.20
Track χ^2 Probability	0.04	0.46	0.29	0.08	0.99	0.91	0.50	0.97	0.86	0.98
Impact to Wire (σ)	2.74	4.72	2.19	0.82	9.64	4.86	24.14	12.48	4.40	1.28
CDA_{prim} (σ)	2.12	2.86	4.10	7.26	7.58	13.81	24.1	14.2	11.7	20.6
Impact to J/ψ (σ)	-	-	0.13	-	-	0.056	-	-	0.05	0.24

Table 6.4: Selected characteristics of the $B^+ \to J/\psi\, K^+$ and $B^0 \to J/\psi\, K^+\, \pi^-$ candidates

6.6 Electron channel

A search is also performed among events with the J/ψ decaying into two electrons. In this channel a total sample of 103800 $\pm$ 1000 of prompt J/ψ was found with 36.9 $\pm$ 8.1 b events, in the inclusive $b \to J/\psi$ decay with a similar technique as described in previous section for the muon channel, but different cut values [80]. Taking into account efficiencies from MC studies we expect in the electron channel 1.4 and 0.5 events in the $B^+ \to J/\psi\, K^+$ and $B^0 \to J/\psi\, K^+\, \pi^-$ channels, respectively, without any detached vertex requirement. The selection procedure is identical to the one described previously for the muon channel. Since no good events were found in which a decay of the type $B^+ \to J/\psi\, K^+$ or $B^0 \to J/\psi\, K^+\, \pi^-$ was fully reconstructed, we loosened somewhat one of the detached selection criteria. Instead of requiring that both electrons have an impact parameter to the wire exceeding $3\,\sigma$ (optimised value for the electron channel [80]), it was required that the sum of their impact parameters must exceed $6\,\sigma$. A detailed look at the event characteristics reveals one event with good B characteristics in the $B^+ \to J/\psi\, K^+$ decay. Table 6.4 shows all the characteristics of this event.

6.7 Event display

The selected events are displayed in Figs. 6.6, 6.7 and 6.8 using the HERA – B event display PRISM [111]. The event display has the limitation that particles assigned to a common vertex are actually displayed as coming from a common vertex. Thus at vertex level the display is not accurate. We show here only general pictures of the event.

6.8 Summary and conclusions

As for the muon channel we can assume one event with no background seen in the scenarios with the strongest detachment and kaon selection in each decay for both $B^+ \to J/\psi\, K^+$ and $B^0 \to J/\psi\, K^+\, \pi^-$ decay channels. Based on the Feldman and Cousins tables [112] this represents a confidence belt between 0.11 - 4.36 at 90 % C.L. in the number of events. This value is compatible with the expected values shown in Table 6.3: 0.37 events for $B^+ \to J/\psi\, K^+$ and 0.1 for $B^0 \to J/\psi\, K^+\, \pi^-$ decay channels.

Figure 6.9 shows the invariant mass of the B candidates for muon and electron channels together, for both B decays under study, in the scenario with hard cuts applied. Figure 6.10 sums up both decay channels in the same scenario. A note of caution must be made since it may happen that some events in the $B^0 \to J/\psi\, K^+\, \pi^-$ distribution happen to pass the selection for the $B^+ \to J/\psi\, K^+$ channel.

In the combined invariant mass distribution there might be a small group of events

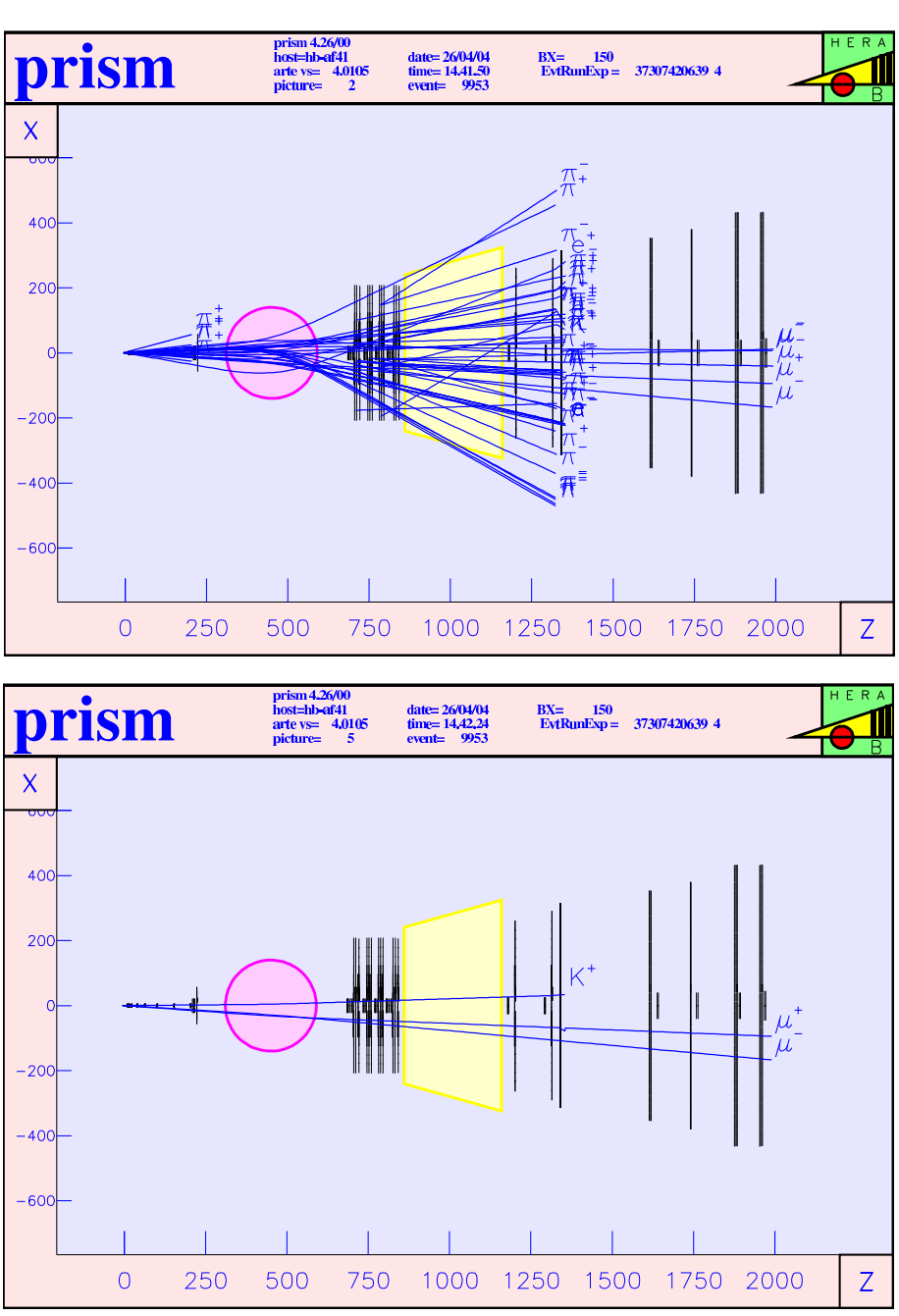

Figure 6.6: Run 20639; Event 373074. (a) All particles in the $x - z$ plane; (b) $B^+ \to J/\psi\, K^+$ in the $x - z$ plane.

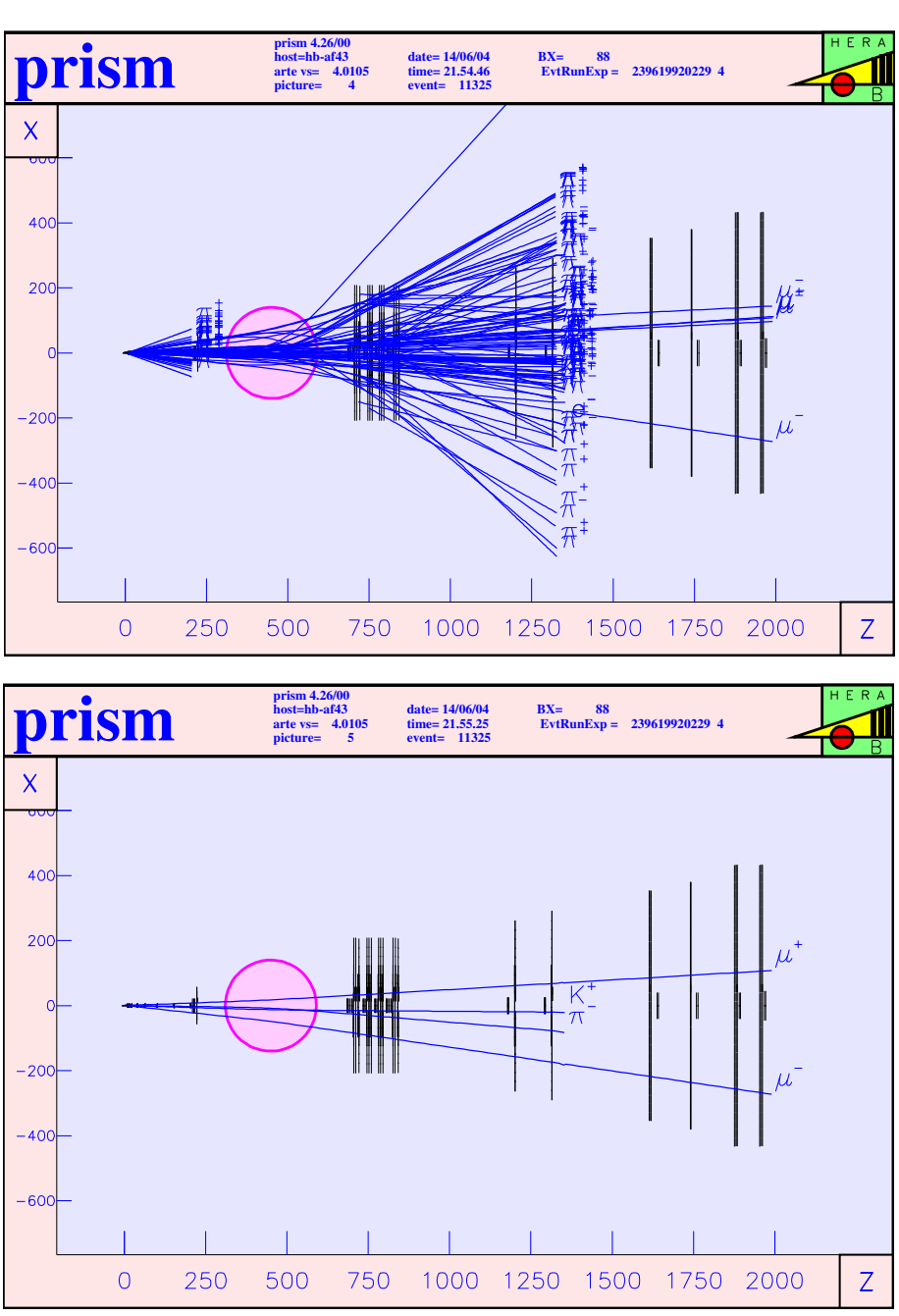

Figure 6.7: Run 20229; Event 2396199. (a) All particles in the $x - z$ plane; (b) $B^0 \to J/\psi\, K^+\, \pi^-$ in the $x - z$ plane.

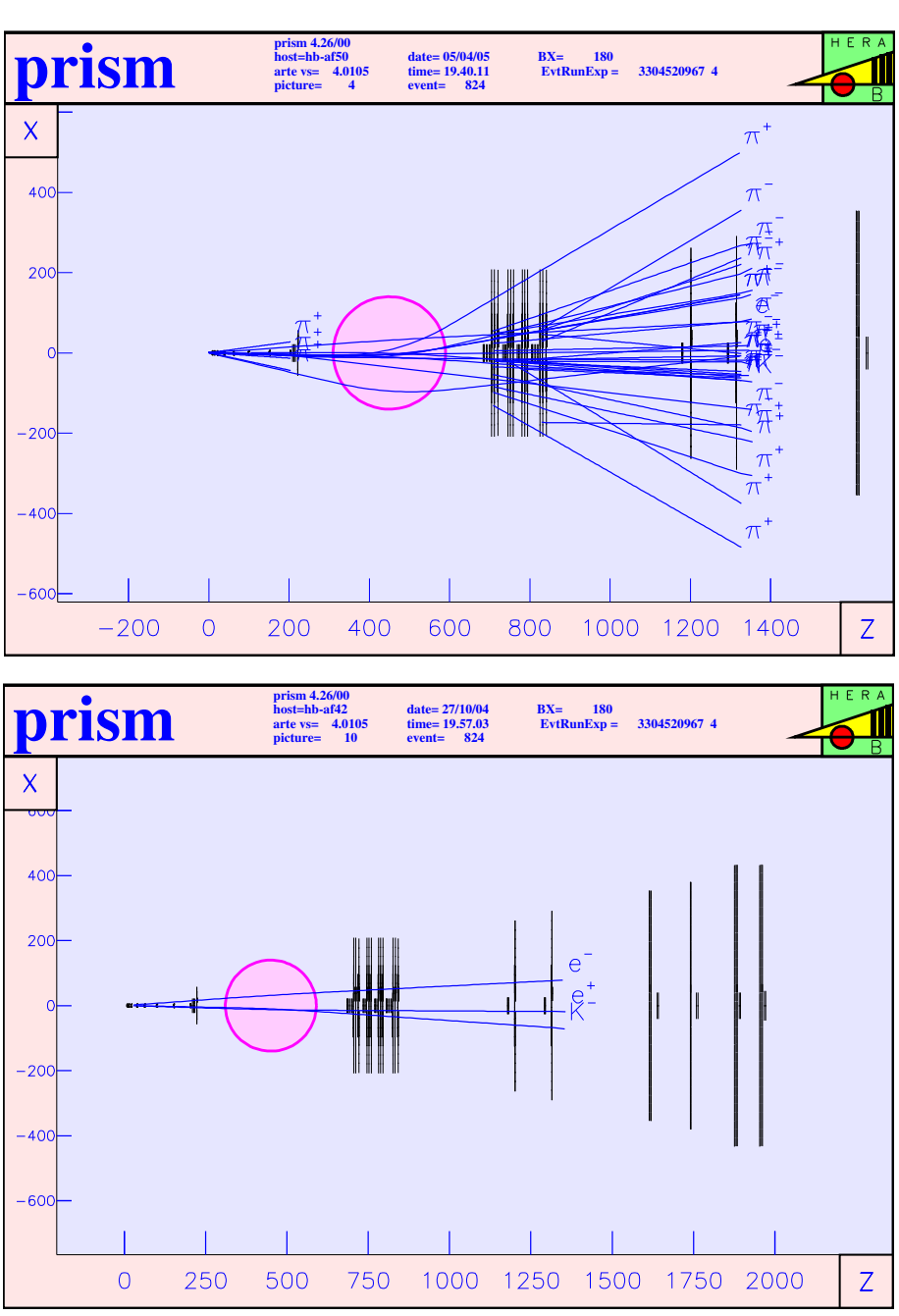

Figure 6.8: Run 20967; Event 33045. (a) All particles in the $x-z$ plane; in the $x-z$ plane; (b) $B^+ \to J/\psi\, K^+$ in the $x-z$ plane.

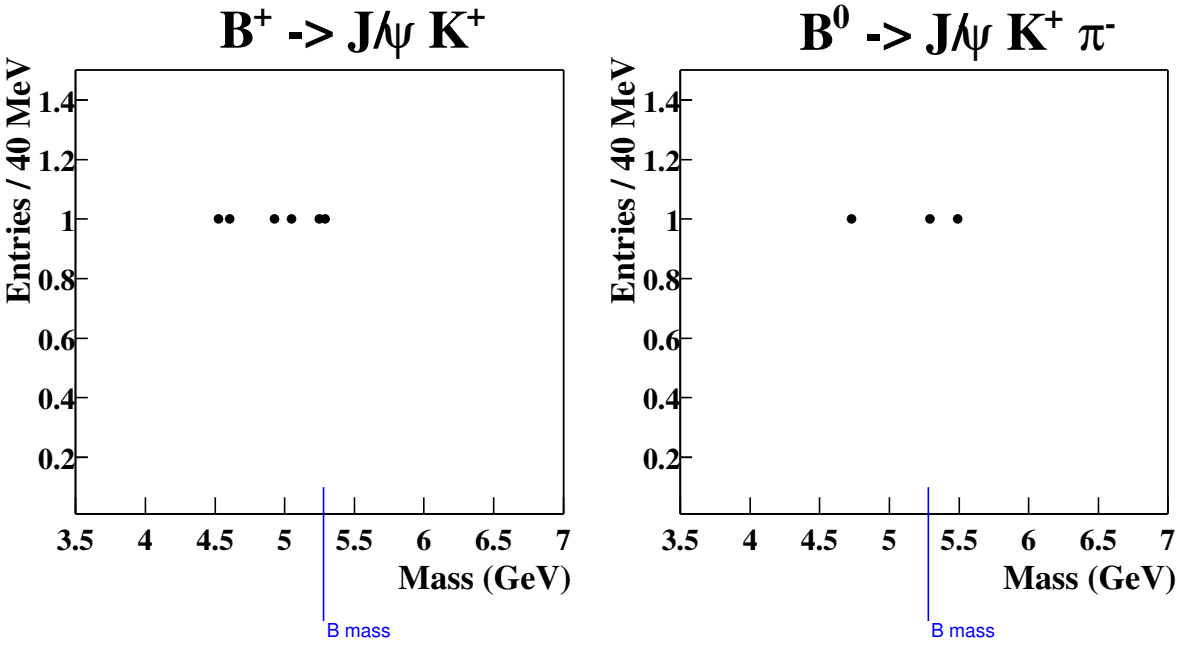

Figure 6.9: Invariant mass of the B candidates with the decay together in both muon and electron channel in the scenario with hard detaching selection and and kaon identification. a) $B^+ \to J/\psi\ K^+$. b) $B^0 \to J/\psi\ K^+\ \pi^-$

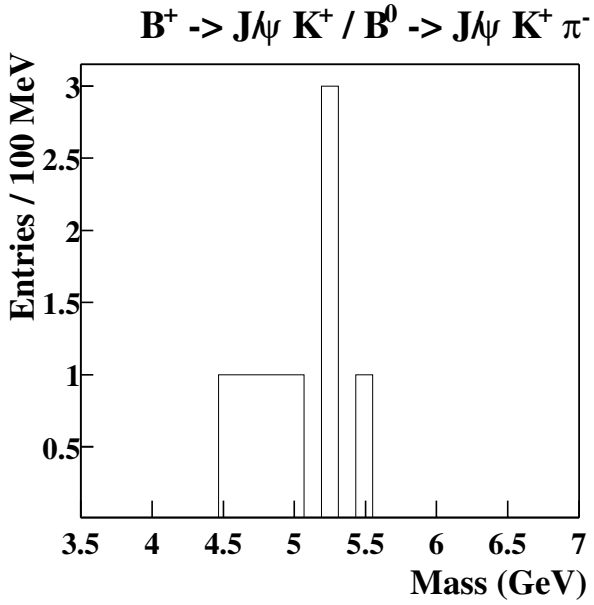

Figure 6.10: Invariant mass for both decay channels together for electrons and muons. Events are selected with hard detaching cuts and kaon identification.

in the region of the B mass, which could be taken as a hint of a signal. The total number of candidates is in accordance with the expectations of signal and a background consisting of B decays with unreconstructed final state particles. The statistics is clearly insufficient to claim a signal, not to speak of a determination of the production cross section. However, the analysis presented in this section shows the potential of HERA – B for the reconstruction of B events and strengthens our confidence in the inclusive b samples presented in previous chapter.

Bibliography

[1] J.C. Collins, D.E. Soper and G. Steran, Nucl. Phys. **B261** (1985) 104.

[2] G.T. Bodwin, Phys. Rev. **D31** (1985) 2616, E. Erratum-ibid.**D34**,(1986) 3932.

[3] M. Mangano, P. Nason and G. Ridolfi, Nucl. Phys. **B373** (1992) 295.

[4] P. Nason, S. Dawson and R. K. Ellis, Nucl. Phys. **B327** (1988) 49.

[5] W. Beenakker, H. Kuijf, W.L. van Neerven and J. Smith, Phys. Rev. **D40** (1989) 54.

[6] W. Beenakker, W.L. van Neerven, R. Meng, G.A. Schuler and J. Smith, Nucl. Phys. **B351** (1991) 507.

[7] F. Halzen and A.D. Martin, *Quarks & Leptons*, Jhon Wiley and Sons, 1984.

[8] G. 't Hooft, M.J.G. Veltman, Nucl. Phys. **B44** (1972) 189.

[9] L. H. Ryder, *Quantum Field Theory*, Cambridge University Press, 1996.

[10] CLEO Collaboration, R. Ammar *et al.*, Phys. Rev. **D57** (1998) 1350.

[11] P. Nason, S. Dawson, R.K. Ellis, Nucl. Phys. **B303** (1988) 607.

[12] P. Nason, *Introduction to QCD*, Prepared for The 1997 European School of High-Energy Physics, Menstrup, Denmark, 25 May - 7 Jun 1997.

[13] R.K. Ellis, H. Georgi, M. Machacek, H.D. Politzer and G.G. Ross, Phys. Lett. **B78** (1978) 281.

[14] G. Altarelli and G. Parisi, Nucl. Phys. **B126** (1977) 298.

[15] W. A. Barden *et al.*, Phys. Rev. **D18** (1978) 3998.

[16] H. L. Lai *et al.*, Eur. Phys. J. **C12** (2000) 375.

[17] A. D. Martin, R. G. Roberts, W. J. Stirling, and R. S. Thorne, Phys. Lett. **B531** (2002) 216.

[18] M. Glück, E. Reya, A. Vogt, Eur. Phys. J. **5** (1998) 461.

[19] N. Tuning, *Proton structure functions at HERA*, Ph.D. thesis, Univ. Amsterdam, 2001.

[20] S. Frixione *et al.*, Nucl. Phys. **B431** (1994) 453.

[21] R. Bonciani, S. Catani, M.L Mangano and P. Nason, Nucl. Phys. **B529** (1998) 24.

[22] N. Kidonakis, E. Laenen, S. Moch and R. Vogt, Phys. Rev. **D64** (2001) 114001.

[23] N. Kidonakis and R. Vogt, Eur. Phys. J. **36** (2004) 201.

[24] E789 Collaboration, D.M. Jansen *et al.*, Phys. Rev. Lett. **74** (1995) 3118.

[25] HERA – B Collaboration, I. Abt *et al.*, Eur. Phys. J. **26** (2003) 345.

[26] E771 Collaboration, T. Alexopoulos *et al.*, Phys. Rev. Lett. **82** (1999) 41.

[27] C. Peterson *et al.*, Phys. Rev. **D27** (1983) 105.

[28] V. G. Kartvelishvili, A. K. Likhoded and V. A. Petrov, Phys. Lett. **B78** (1978) 615.

[29] ALEPH Collaboration, A. Heister *et al.*, Phys. Lett. **B512** (2001) 30.

[30] M. Bruinsma, *J/ψ in pA*, Ph.D. thesis, Univ. Utrecht, 2002.

[31] R. Baier and R. Rückl, Phys. Lett. **B102** (1981) 364.

[32] R. Baier and R. Rückl, Z. Phys. **C19** (1983) 251.

[33] G.T. Bodwin, E. Braaten and G.P. Lepage, Phys. Rev. **D51** (1995) 1125.

[34] P. Cho and A. Leibovich, Phys. Rev. **D53** (1996) 6203.

[35] H. Fritzsch, Phys. Lett. **B67** (1977) 217.

[36] F. Halzen, Phys. Phys. Lett. **B69** (1977) 105.

[37] F. Halzen and S. Matsuda, Phys. Rev. **D17** (1978) 1344.

[38] M. Glück, J. Owens and E. Reya, Phys. Rev. **D17** (1978) 2324.

[39] R. Gavai *et al.*, Int. J. Mod. Phys. **A10** (1995) 3043.

[40] J.F. Amundson *et al.*, Phys. Lett. **B372** (1996) 127.

[41] J.F. Amundson *et al.*, Phys. Lett. **B390** (1997) 323.

[42] T. Affolder *et al.*, Phys. Rev. Lett. **85** (2000) 2886.

[43] E789 Collaboration, M.H. Schub *et al.*, Phys. Rev. **D52** (1995) 1307.

[44] R. Vogt, Int. J. Mod. Phys. **E12** (2003) 211.

[45] E789 Collaboration, M. J. Leitch *et al.*, Phys. Rev. Lett. **72** (1994) 2542.

[46] FNAL E866/NuSea Collaboration, M. J. Leitch *et al.*, Phys. Rev. Lett. **84** (2000) 3256.

[47] T. Lohse *et al.*, *HERA – B Proposal*, DESY-PRC 94/02 (1994) .

[48] A. Hartouni *et al.*, *HERA – B Technical Design Report*, DESY-PRC 95/01 .

[49] BABAR Collaboration, B. Aubert *et al.*, Phys. Rev. Lett. **89** (2002) 201802.

[50] Belle Collaboration, K. Abe *et al.*, Phys. Rev. **D66** (2002) 071102.

[51] The HERA – B Collaboration, *Report on Status and Prospects*, DESY-PRC 00/04 (2000) .

[52] M.C. Abreu *et al.*, Phys. Lett. **B477** (2000) 28.

[53] I. Abt *et al.*, Phys. Lett. **B561** (2003) 61.

[54] A. Lanyov and T. Bauer, *Analysis Note on the Upsilon Production Cross Section in pA Collisions at HERA – B* , HERA – B Note 05-007 (2005) .

[55] HERA – B Collaboration, I. Abt *et al.*, Phys. Lett. **B596** (2004) 173.

[56] I. Abt *et al.*, Eur. Phys. J. **29** (2003) 181.

[57] LEPS Collaboration, T. Nakano *et al.*, Phys. Rev. Lett. **91** (2003) 012002.

[58] CLAS Collaboration, S. Stepanyan *et al.*, Phys. Rev. Lett. **91** (2003) 252001.

[59] DIANA Collaboration, V. V. Barmin *et al.*, Phys. Atom. Nucl. **66** (2003) 1715.

[60] SVD Collaboration, A. Aleev *et al.*, hep-ex/0401024, 2004.

[61] ZEUS Collaboration, S. Chekanov *et al.*, Phys. Lett. **B591** (2004) 7.

[62] NA49 Collaboration, C. Alt *et al.*, Phys. Rev. Lett. **92** (2004) 042003.

[63] H1 Collaboration, A. Aktas *et al.*, Phys. Lett. **B588** (2004) 17.

[64] HERA – B Collaboration, I. Abt *et al.*, Phys. Rev. Lett. **93** (2004) 212003.

[65] HERA – B Outer Tracker Group Collaboration, C. Stegmann, *The Outer Tracker for HERA – B* , Nucl. Instrum. Meth. **A453** (2000) 153.

[66] HERA – B Outer Tracker Group Collaboration, *The Outer Tracker Detector for the HERA – B Experiment*, in preparation.

[67] I. Arino *et al.*, hep-ex/0303012, 2003.

[68] I. Matchikhilian for the HERA – B ECAL collaboration, *Proceedings of the XI International Conference on Calorimetry in High Energy Physics*, March 2004, Perugia, Italy. To be published by World Scientific.

[69] U. Husemann, *Measurement of Nuclear Effects in the Production of J/ψ Mesons with the HERA – B Detector*, Ph.D. thesis, Univ. Siegeneng, 2005.

[70] R. Frühwirth, Nucl. Instr. Methods **262** (1987) 444.

[71] J. Ivarsson *et al.*, *PYTHIA and FRITIOF: Event Generators for HERA – B* , HERA – B Note 99-067 (1999) .

[72] T. Sjöstrand, Comput. Phys. Commun. **82** (1994) 74.

[73] H. Pi, Comput. Phys. Commun. **71** (1992) 173.

[74] R. Brun *et al.*, *GEANT3*, CERN-DD-EE-84-1 (1987) .

[75] W. Hulsbergen, HERA – B Note 02-075 (2002) .

[76] J. Chirn, Z. Phys. **36** (1987) 163.

[77] D. Decamp *et al.*., Phys. Lett. **B244** (1990) 551.

[78] P. Nason and C. Oleari, Nucl. Phys. **B565** (2000) 245.

[79] J. Chay, S. D. Ellis and W. J. Stirling, Phys. Rev. **D45** (1992) 46.

[80] B. Giacobbe *et al.*, *A New Measurement of the b-bbar Production Cross Section at HERA – B* , HERA – B Note, 04-036 (2004) .

[81] The HERA – B software group, *The Event Reconstruction and Analysis Tool for HERA – B - ARTE*, March 1996.

[82] I. Kisel and S. Masciocchi, *A Cellular Automaton for Tracking in Silicon for the HERA – B Vertex Detector*, HERA – B Note 99-242 (1999) .

[83] D. Emeliyanov, I. Gorbounov and I. Kisel, *OTR/ITR-CATS: Tracking Based on Cellular Automaton and Kalman Filter*, HERA – B Note 01-137 (2001) .

[84] R. Mankel, *A concurrent track evolution algorithm for pattern recognition in the HERA – B main tracking system*, Nucl. Instrum. Meth. **A395** (1997) 169.

[85] M. Villa, *Progress report on the ECAL reconstruction software*, HERA – B Note 97-135 (1999) .

[86] B. Fominykh, HERA – B Note 00-171 (2000) .

[87] *Track based particle identification algorithm - RITER*, http://www-hera-b.desy.de/subgroup/detector/rich/riter/, 1999.

[88] O. Igonkina, *MARPLE -Version 1.03-*, HERA – B Note 98-129 (1998) .

[89] D. Emeliyanov *et al.*, *Generic Reconstruction Of VERtices - GROVER v2.01*, March 2001.

[90] T. Lohse, *Vertex Reconstruction & Fitting*, 1995.

[91] D. Emeliyanov, *Primary Vertex Reconstruction by Grover*, Tracking meeting , March 27th 2002.

[92] M. Bruinsma, J. Hogenbirk and O. Steinkamp, *Documentation on the First Level Trigger Linkboard*, HERA – B Note 98-066 (1998) .

[93] I. Negri, *Mapping of the OTR and the Muon detectors for the First Level Trigger*, FLT internal Note .

[94] Holger Fleckenstein, *Performance of the TFU network of the First Level Trigger of HERA – B and determination of efficiencies for* $J/\psi \to \mu^+\mu^-$, Ph.D. thesis, Univ. Hamburg, 2002.

[95] A. Somov, *FLT online initialization software*, HERA – B Note 02-120 (2002) .

[96] J.Flammer, *Track Parameter Unit Documentation*, HERA – B Note 01-055 (2001) .

[97] Michael Nörenberg, *Objektorientierte Simulation der Trigger Decision Unit des HERA – B First Level Triggers.*

[98] A. Sbrizzi, private comunication.

[99] I. Abt *et al.*, *The HERA – B Apparatus*, in preparation.

[100] V. Balagura, *FLT Efficiency Maps*, HERA – B Note 03-024 (2003) .

[101] V. Balagura, *MU1 Efficiency at FLT*, HERA – B Note 02-035 (2002) .

[102] A. Sbrizzi, Ph.D. thesis, Univ. Amsterdam, in preparation.

[103] M. Mevius, *Beauty at HERA – B* , Ph.D. thesis, Univ. Utrecht, 2003.

[104] T. Alexopoulos *et al.*E771 collab., Phys. Rev. **D55** (1997) 3927.

[105] E771 Collaboration, T. Alexopoulos *et al.*, Phys. Lett. **B374** (1996) 271.

[106] D.E. Groom *et al.*, Eur. Phys. J. **15** (2000) 1.

[107] A. Spiridonov, HERA – B Note 04-016 (2004) .

[108] Particle Data Group (K. Hagiwara *et al.*), Phys. Rev. **D66** (2002) 010001.

[109] M. Mevius, *Selection cuts optimization tool*, Talk at NIKHEF Bfys Meeting , 14th May 2004.

[110] I. Arino, *Measurement of hadron fractions in Proton-Nucleus interactions at 920 GeV/c using the HERA – B detector*, Ph.D. thesis, Univ. Barcelona, 2001.

[111] R. Mankel, *Prism - The HERA-B Event Display and its Tcl/Tk User Interface (Version 4.9)*, 1997.

[112] G. J. Feldman and R. D. Cousins, Phys. Rev. **D57** (1998) 3873.

Conventions

BX	Bunch Crossing
DAQ	Data Acquisition System
DESY	Deutsches Elektronen-Synchrotron
ECAL	Electromagnetic Calorimeter
EVC	Event Controller
FCS	Fast Control System
FED	Front End Drivers
FLT	First Level Trigger
ITR	Inner Tracker
LL	Leading Logarithm
LO	Leading Order
MC	Monte Carlo
MU1, MU2, MU3, MU4	MUON stations
MUON	Muon system
NLL	Next to Leading Logarithm
NLO	Next to Leading Order
OTR	Outer Tracker
PC1, PC2, PC3, PC4	Tracking stations between the magnet and the ECAL
PDG	Particle Data Group
RICH	Ring Imaging Cherenkov Detector
SLB	Second Level Buffer
SLT	Second Level Trigger
TC1, TC2	Tracking stations between the ECAL and the MUON
TDU	Track Decision Unit
TFU	Track Finding Unit
TLB	Trigger Link Board
TPU	Track Parameter Unit
VDS	Vertex Detector System
WM	Wire Memory

Summary

In this thesis we have presented a determination of the $b\bar{b}$ cross section based on data of pN collisions at $\sqrt{s} = 41.6$ GeV which were taken with the HERA – B detector during 2002 and 2003.

At present there are complete theoretical calculations up to next-to-leading-order (NLO) in the expansion of α_s. However, these calculations fail to give an accurate value on the $b\bar{b}$ production at energies near threshold, since higher order terms represent large contributions to the cross section. New developments and theoretical tools were developed in the past years to partially include higher order terms in the perturbative expansion but they still present large uncertainties.

In the past $b\bar{b}$ production on fixed target experiments has been measured three times. These results are not all compatible, and in addition, they suffer from limited statistics.

The method presented in this thesis to measure the $b\bar{b}$ cross section is based on the characteristics of the long life time of the B mesons and their inclusive decay into a J/ψ. It is thus sufficient to detect the decay of those J/ψ into lepton pairs which are not produced in the primary interaction, but which have their decay vertex downstream. The small $b\bar{b}$ production cross section in combination with the small branching ratio of $b \to J/\psi$ implies that only a fraction of $\approx 10^{-11}$ of all events are useful which underlines the need for a highly efficient trigger. The trigger system of HERA – B incorporates a hardware track reconstruction in the first trigger level, and software vertexing in the second level. The dedicated J/ψ First Level Trigger (FLT) is build on a network of specific processor boards and performs a lepton track selection within 12 μs. It is of crucial importance to understand its single track efficiency, which is explained in detail in this thesis, and which has been determined to be ($61.1 \pm 0.2_{stat} \pm 1.0_{sys}$) % for electrons and ($28.0 \pm 0.1_{stat} \pm 0.6_{sys}$) % for muons. The rejection power is estimated to be about 200. The characteristics of the FLT allowed the collection of 300,000 reconstructed J/ψ events in both electron and muon channels, leading to an identified sample of 83 $b \to J/\psi$ inclusive events.

The $b\bar{b}$ production cross section is determined relative to the J/ψ production cross section which has been measured by other experiments. Our analysis, based on muon tracks, yields a cross section ratio of $b\bar{b}$ over J/ψ production $R_{sigma} = \sigma(b\bar{b})/\sigma_{J/\psi} = 0.027 \pm 0.005_{stat} \pm 0.004_{sys}$. Based on $\sigma_{J/\psi} = 352 \pm 2_{stat} \pm 26_{sys}$ nb/nucleon as measured by

Fermilab experiments we obtain for $\sigma(b\bar{b}) = 9.4 \pm 1.7_{stat} \pm 1.3_{sys}$ nb/nucleon. The full HERA – B result, *i.e.* the muon result combined with the electron channel and together with the data of the year 2000 is at present the most precise measurement of the $b\bar{b}$ production cross section with a value of $\sigma(b\bar{b}) = 9.9 \pm 1.5_{stat} \pm 1.4_{sys}$ nb/nucleon. This result is compatible with the data of the E789 experiment, but is more than 2 σ below the result of the E771 experiment. Theoretical calculations beyond NLO order, which are performed with different resummation techniques, are several σ above our measurement, but are still compatible due to the large theoretical uncertainties.

An attempt to identify exclusive B-decays resulted, due to the limited statistics, in only a few events fully reconstructed in the $\mathrm{B}^+ \to J/\psi\ \mathrm{K}^+$ and $\mathrm{B}^0 \to J/\psi\ \mathrm{K}^+\ \pi^-$ channels. This is compatible with the expectations.

Samenvatting

Materie zoals deze op aarde voorkomt is opgebouwd uit atomen: kernen met daaromheen elektronen. De kernen bestaan uit protonen en neutronen. Verstrooiings-experimenten hebben aangetoond dat protonen en neutronen opgebouwd zijn uit kleinere bouwstenen; de quarks. Voor het proton en het neutron hebben we twee quarkvarianten nodig, de up (u) en down (d) quark. In radioactief verval blijkt er nog een deeltje nodig te zijn, namelijk het neutrino (ν_e). De twee quarks, het elektron en het neutrino vormen samen een "familie" van elementaire deeltjes. De deeltjes interageren met elkaar via de sterke wisselwerking tussen quarks onderling, de elektromagnetische wisselwerking tussen geladen deeltjes en de zwakke wisselwerking tussen alle deeltjes.

In hoog energetische interacties, bijvoorbeeld proton-proton botsingen, hebben we de mogelijkheid om uit de beschikbare energie nieuwe deeltjes te vormen. De productie van deze deeltjes moet aan een aantal behoudswetten voldoen (b.v. ladingsbehoud). Het is daarom in het algemeen alleen mogelijk om deeltjes samen met hun antideeltjes te produceren.

Experimenteel is in de laatste decennia gebleken dat er een verrassende herhaling van deeltjes optreedt. De familie wordt herhaald maar dan met deeltjes die meer massa hebben. Zo bestaat de tweede familie uit een muon (μ, een zwaar soort electron), een tweede soort neutrino (ν_μ), een charm (c) en strange (s) quark. De charm quark heef in deze familie de hoogste massa. De derde familie, tenslotte, heeft als leden de tau (τ), het bijbehorende neutrino (ν_τ), de topquark (t) de "zwaarste", met een massa van 175 GeV of wel bijna de massa van een wolfraamkern en het onderwerp van dit proefschrift: de bottomquark (b). Deze heeft een massa van vijf protonen ofwel 5 GeV.

De productie van b-quarks verloopt via de sterke wisselwerking. Deze wordt beschreven door QuantumChromoDynamica of QCD. In deze theorie wordt de productie van quarks beschreven door middel van een zogenaamde storingsreeks. De belangrijkste termen in de berekening worden als eerste benadering gebruikt. De berekeningen kunnen verfijnd worden door meer termen in de reeks mee te nemen. De termen die meegenomen moeten worden hangen mede af van hoeveel energie beschikbaar is voor de productie. Dicht bij de productiedrempel zijn sommige termen belangrijk en het is in dit gebied dat wij onze metingen hebben uitgevoerd.

Om een b-quark samen met zijn antideeltje de anti-b te produceren is minimaal 10 GeV

in het zwaartepuntsysteem van de interactie nodig. In de praktijk is een veel hogere energie nodig omdat in de interacties niet alleen b-quarks geproduceerd worden maar ook vele andere deeltjes, tot wel honderd in een interactie. Ook worden niet in elke interactie b-quarks geproduceerd. Bij HERA – B , het experiment waarover dit proefschrift gaat, worden protonen van 920 GeV in botsing gebracht met draden van Koolstof, Titanium en Wolfraam. De energie beschikbaar voor deeltjes productie is dan 41.6 GeV. Onder deze omstandigheden wordt er een b-anti-b paar geproduceerd in één op de miljoen interacties. Willen we deze op efficiënte wijze registreren, dan is het van belang gebeurtenissen met b-quarks snel te herkennen.

Quarks komen niet vrij in de natuur voor maar alleen in combinatie met andere quarks of een anti-quark. De deeltjes die bestaan uit zwaardere quarks zijn niet stabiel maar vervallen naar deeltjes die lichtere quarks bevatten. Zij hebben echter een eindige levensduur: voor deeltjes die een b-quark bevatten is deze levensduur ongeveer 1.5 ps. Dit betekent dat zij in het HERA – B experiment gemiddeld zo'n 9 mm afleggen voordat ze uiteenvallen. Wij kunnen ze dus herkennen in de detector als een verzameling van sporen (de vervalsproducten) die niet afkomstig zijn van een van de draden maar van een punt een aantal millimeters verwijderd van de draad. Dit patroon is unieke voor deeltjes met zware quarks. Om de herkenning van deze deeltjes nog meer te versimpelen hebben wij ons geconcentreerd op een bepaald vervalsproduct: het J/ψ deeltje. Dit heeft een massa van 3.1 GeV en vervalt ondermeer naar de eenvoudige eindtoestanden e^+e^- en $\mu^+\mu^-$. Dit laatste kanaal is in dit proefschrift beschreven.

Het J/ψ deeltje kan ook direct geproduceerd worden (dus niet als vervalsproduct van een b-quark deeltje) en de kans dat dit gebeurt, de botsingsdoorsnede, is goed bekend. Door nu zowel de directe (van de draad) als de indirecte (via verval een eindje van de draad) te vergelijken kunnen we de botsingsdoorsnede voor b-quarks bepalen.

Dit proefschrift beschrijft de zoektocht naar de gebeurtenissen met J/ψ deeltjes. Hierbij wordt gebruik gemaakt van geavanceerde elektronica die, binnen 12 μs, informatie uit de detectoren in het experiment kan reconstrueren tot sporen. Ook kan in die tijd worden beslist of dit spoor aan een muon of elektron toebehoort. Hierna moeten de geselecteerde gebeurtenissen volledig gereconstrueerd, en het J/ψ deeltje gezocht worden. Dit heeft geresulteerd in een verzameling van 300000 direct geproduceerde en 85 indirect geproduceerde J/ψ deeltjes. Hieruit kan de werkzame doorsnede van b-productie gehaald worden maar niet voordat een gedegen studie gedaan is naar hoe efficient ieder onderdeel van het experiment heeft gewerkt.

Acknowledgements

During the four and a half years of my PhD, there were many people that supported and helped me with the work included in this thesis and also in life as whole inside and outside work. I will try to thank some of them aiming to follow a chronological order.

First of all I want to thank Thomas Bauer for giving me the opportunity to come to Holland and work at HERA – B , and also for all his support and guidance during all the years of my PhD. At the beginning of my work I was enthusiastically guided and assisted by Maarten Bruinsma in all the technicalities needed to perform my duties. I also profited a lot from his knowledge about the first level trigger and HERA – B in general. During that first year I also had the opportunity to interact with Wouter Hulsbergen and Maaijke Mevius. Maaijke also helped me in the last years with the analysis, sharing all her knowledge on the cross section studies and also supporting me whenever the analysis was slowed down, she always picked up the problems and gave me the hints to solve them. She was always very encouraging, ready to help and to give any kind of support. During the first period I had great fun going out with a group of students living in the *Kiezel* building. After most of them left I luckily kept meeting in Amsterdam Antonio, Carlos, Fran and Paola. When I moved to Hamburg I had the pleasure to share office and work with Mohamed Ouchrif and Antonello Sbrizzi. I want to thank Antonello for many things; we shared a lot of discussions and supported each other in the day by day work, but beyond that we spent a good time outside the office going out and travelling. I think I was lucky to find in him a great friend and "compagno" to share a lot of experiences with. During my permanence in Hamburg I was involved in the FLT group where I profited from discussion and interaction with Robert Pernack, Imma Riu, Bernhard Schwingenheuer, Alexandre Somov, Vladik Balagura, Vladimir Popov and Pavel Meshkov. Bernhard was the coordinator of the group and working with him was a very stimulating experience, learning from his knowledge on hardware, physics and his passionate dedication to work. I am grateful to Gabriela for her great company and the good time that we shared during the period in Hamburg.

When coming back again to Holland, I started the studies in the field of B physics, participating in the B physics group of HERA – B , where I usefully collaborated with Benedetto Giacobbe, Silvia Masciocchi, Maaijke, Martin zur Nedden, Mauro Villa and Antonio Zoccoli. Mauro was coordinating the group and I profited from him on his great knowledge in the field of B physics and the precise knowledge of all the small details that

are needed to bring the analysis to final high quality scientific work. During all these years I shared office, meetings, schools, lunches, dinners, beers with many colleges and friends from Utrecht University, DESY and NIKHEF. I would like to thank them all and I would specially like to mention Niels Tuning, Jeroen van Tilburg, Bart Hommels, Marko Zupan, Emanuele Simili, Eelco Schillings, Gabriel Ybeles Smit, Erik Maddox, Andreas Reischl, Michiel Demey, Antonio Pellegrino, Teresa and Conchita Nuñes, Alexey Sokolov and Marcel Merk.

For all the company and fun outside office hours I would specially like to mention Jacopo Nardulli, Maaike Limper, Claudine Colnard, Angelo (and occasionally Cosimo) for the many dinners and going out events that we shared, they all have been a great company during the last year. In Jacopo I also found a good friend with whom to share time at work supporting each other in the day by day struggle. I would like to thank to Carien for her support and the nice time together in Amsterdam.

For the last writing phase, I would like to thank Paul Kooijman for his useful suggestions and comments. I have to specially thank Thomas again for all his advice and corrections over the many versions of thesis that I gave him. I also want to thank Antonello, Maaijke, and Bernhard for the reading and suggestions on different sections of the manuscript.

Finally I would like to thank all my family and specially my parents, sister and brother, who despite the physical distance were all the time very close.